

Pressure-Assisted Fabrication of Organic Light Emitting Devices



Vitalis Chioh Anye

(ID #: 70045)

A Dissertation Presented to the Faculty of African University of Science
and Technology, Abuja, Nigeria

In Candidacy for the Degree of Doctor of Philosophy

Recommended for Acceptance by

The Department of Materials Science and Engineering

Advisor

Prof. Wole Soboyejo

Co-Advisor

Prof. M.G. Zebaze Kana

June, 2015.

© Copyright by Vitalis Chioh Anye, 2015.

All Rights Reserved.

Dedication

To the Almighty God for his constant care and protection

To my wife, Odette and son, Daniel for their love and support

To my mum (deceased) for all the toils to bring me up to where I am today.

Abstract

This dissertation presents an overview of the research work with the above caption. This research is divided into five major sections or parts. Part one deals with interfacial adhesion studies of the layers relevant to organic light-emitting diodes (OLEDs). The adhesion interactions, that is, force and energy between different interfaces of the adjacent layers relevant to the OLED structure used in this work are analyzed together with their implication(s) on the device performance. In the second part of the research, we use nanoindentation techniques to determine the mechanical properties of the OLED layers. These properties are utilized in computational models essential to validate the experimental results. Pressure-assisted fabrication of OLEDs is described in the third section of the research. It was noticed from the experimental and finite element analyses that the application of pressure on finished OLEDs has the potential to improve their performance. Electrical characterization of the devices fabricated with molybdenum trioxide (MoO_3) and poly[3,4-ethylenedioxythiophene]: poly(styrene sulfonate) (PEDOT:PSS) as hole injection layer materials (HILMs) show a 50% reduction in turn-on voltage when the devices are compressed. MoO_3 -based devices without pressure application revealed lower turn-on voltages without pressure than PEDOT: PSS-based. This implies that MoO_3 represents a better HILM than PEDOT: PSS. The fourth part of this work is concerned with an attempt to prolong the life of these devices. This is achieved through encapsulation with the use of polydimethyl siloxane (PDMS). This encapsulation process has the potential to tune the optical properties of the material layers. Optical simulations using COMSOL Multiphysics ver. 4.3 finite element analysis software package is used to better capture the effect of this change in optical properties on the diffusion of the light produced by the device. In the last part of this research, we will employ more cost-effective and temperature friendly techniques through soft-contact lamination to deposit some of the layers relevant to OLEDs. A fracture mechanics approach is used to analyze the differential adhesion energy and energy release rate during pull-off of the stamp material used as anvil.

Acknowledgements

Firstly, I would like to give thanks to Almighty God for his grace through his son, Jesus Christ. None of this work would have been possible without his mercy, love and guidance.

I would also like to give thanks to my advisor, Wole Soboyejo, for letting me be part of his team, family and vision. My time under his tutelage has been nothing short of a once in a lifetime experience; the details of which, could fill another volume of text with lessons on life and research. Sincere gratitude goes to my co-advisor, Prof M.G. Zebaze Kana for putting me through the laboratory sessions and his efforts in helping me become a better scientist. I would also like to thank Prof Omololu Akin-Ojo and Dr. Jing Du for their efforts in reviewing this thesis and making invaluable inputs.

The work presented in this thesis would not have been possible without the efforts of a number of people at AUST. I would like to thank them for their contributions:

Damilola Momodu for open discussions where your candidness and honesty led to worthwhile conclusions on life and research; Kehinde Oyewole for his practical wisdom in confusing times; Joseph Asare for his unique sense of humor and style; Egidius Rwenyagila for his coolness and calmness; Benjamin Agyei-Tuffour for his encouragements and potent advice; and of course Fashina Adebayo for his sensible nature. I would also like to thank Tiffany Tong and Deying Yu, former graduate students at Princeton University for their tremendous support during my time at Princeton. Much thanks also goes to Mr. Fru Juvet for being a brother and a friend at all times.

I would like to thank my beloved wife, Odette, for being extremely supportive and understanding all through this period. Thank you for being my confidant. I love you so much. And to my dear son, Daniel, for his broad smile that keeps me going even during tough times. My sincere gratitude also goes to my dad, Mr Gideon Anye, for his love, encouragement, support and vision; my siblings, Emmanuel, Salome (Big), Laura (Yoyo), Julius, Maureen and Vivian (Bibis) for their words of encouragement and support in diverse ways. I love you all so very much!

As a matter of fact, a proper and comprehensive acknowledgement is not possible. I can only try to show my true feelings of appreciation in my actions and deeds once my time at AUST is over. Only God, in his infinite grace and mercy, can truly reward all the people that have made this possible.

God bless you all!

Vitalis Chioh Anye

AUST, Abuja

June, 2015.

Table of Contents

Dedication.....	i
Abstract.....	ii
Acknowledgements.....	iii
Table of Contents.....	iv
List of Tables.....	viii
List of Figures.....	ix
List of Abbreviations and Symbols.....	xv
List of Peer-Reviewed Publications.....	xviii
List of Workshops and Conference Presentations.....	xix
Chapter 1.....	1
Background and Introduction.....	1
1.1 Background.....	1
1.2 Research Objectives.....	4
1.3 Scope and Organization of Thesis.....	4
References.....	6
Chapter 2.....	9
Literature Review.....	9
2.1 Adhesion and Contact Deformation Theories.....	9
2.2 Fundamentals of Fracture Mechanics.....	15
2.2.1 Fundamentals of Linear Elastic Fracture Mechanics (LEFM).....	15
2.2.2 Fundamentals of Elastic-Plastic Fracture Mechanics (EPFM).....	18
2.2.3 Interfacial Fracture Mechanics.....	19
2.3 Lamination and stamping of Organic Light Emitting Diode layers.....	24
2.3.1 Alternative Schemes for the Fabrication of Organic Electronic Devices.....	24
2.3.2 Contact and Adhesion in Organic Electronic Structures.....	33
2.4 Encapsulation and Red-Shift in Organic Light Emitting Devices.....	36
2.5 Transition metal oxides for organic electronics.....	39
References.....	42

Chapter 3.....	49
Pressure Effects on the Performance of Organic Light Emitting Devices	49
3.1 Introduction.....	49
3.2 Experiments	51
3.3 Characterization of layers and device	54
3.3.1 Nanoindentation.....	54
3.3.2 Atomic Force Microscopy Measurements	55
3.3.3 Optical Measurements.....	56
3.4 Analytical and Numerical Modeling.....	56
3.4.1 Adhesion Models and Adhesion Energy.....	56
3.4.2 Analytical Models for Pressure-Free Contact	58
3.4.3 Finite Element Analysis.....	59
3.5 Results and Discussion.....	62
3.5.1 Electrical Characterization of OLEDs	62
3.5.2 Optical Transmittance Measurements.....	64
3.5.3 Nanoindentation Results	65
3.5.4 Adhesion Measurements and Adhesion Energy	68
3.5.5 Evolution of Contact Profiles under Pressure	69
3.5.6 Implications.....	73
3.6 Summary and Concluding Remarks	74
References.....	75
Chapter 4.....	79
Adhesion in Organic Light Emitting Devices.....	79
4.1 Introduction.....	79
4.2 Theory of Adhesion	80
4.3 Experiments	85
4.3.1 OLED Fabrication.....	85
4.3.2 HOILED Fabrication.....	87
4.3.3 AFM Experiments.....	87
4.4 Finite Element Modeling of Interfacial Fracture/Delamination.....	89
4.5 Results and Discussion	91
4.5.1 Surface Morphology	91

4.5.2. Force-Displacement Characteristics.....	92
4.5.3. Adhesion Energies of Organic Electronic Devices	94
4.5.4 Effects of Inorganic Nanoparticle Additives on Device Behavior.....	97
4.5.5 Inter- and Intra-facial Adhesion Energies for Hybrid Organic/Inorganic Light Emitting Devices	98
4.5.6 Finite Element Simulations.....	99
4.5.7 Implications.....	100
4.6 Summary and Concluding Remarks	102
References.....	102
Chapter 5.....	105
Stamping and Transfer Printing of Organic Light Emitting Diode Layers.....	105
5.1 Introduction.....	105
5.2 Experimental Methods	107
5.2.1 Spin-Coating of Polymer Layers.....	107
5.2.2 Preparation of PDMS anvil	108
5.2.3 Lamination of MEH-PPV layers.....	108
5.3 Atomic Force Microscopy Measurements	110
5.4 Finite Element Simulations.....	110
5.5 Results and Discussion	114
5.5.1 Spin-Coated versus Laminated Polymer Layers	114
5.5.2 Finite Element Simulations.....	118
5.5.3 Implications.....	124
5.6 Summary and Concluding Remarks	125
References.....	126
Chapter 6.....	129
Encapsulation of Organic Light Emitting Diodes and Red-Shift of its Electroluminescence Spectra	129
6.1 Introduction.....	129
6.2 Experimental Procedures	132
6.2.1 Organic Light Emitting Diode Fabrication	132
6.2.2 PDMS Encapsulation	133
6.3 Thin Film Layers/Device Characterization.....	134
6.3.1 Electrical Characterization.....	134

6.3.2 Optical Characterization	135
6.3.3 Sensitivity Tests	135
6.3.4 Storage Tests	135
6.3.5 Mechanical Test	136
6.3.6 Adhesion Measurements	139
6.4 Finite Element Modeling	143
6.5 Results and Discussion	147
6.5.1 Electrical and Optical Characteristics	147
6.5.2 Sensitivity Tests	152
6.5.3 Storage Tests	154
6.5.4 Mechanical Robustness	155
6.5.5 AFM Measurements	156
6.5.6 Optical Model	156
6.5.7 Implications	159
6.6 Summary and Concluding Remarks	164
References	164
Chapter 7	169
Concluding Remarks and Suggestions for Future Work	169
7.1 Concluding Remarks	169
7.2 Suggestions for Future Work	171

List of Tables

Table 3.1: Material properties used in the finite element simulations.

Table 4.1: Average roughness (Ra) and thickness of different OLED layer structures.

Table 4.2: Summary of adhesion forces and energies (computed using DMT adhesion model).

Table 5.1: Mechanical properties of tri-layer materials used in simulations.

Table 5.2: Surface roughness of laminated layers.

Table 6.1: Simulation Parameters for the Field Distribution at a Wavelength of 600 nm.

Table 6.2: Adhesion energies between different device layers in fabricated polymer light emitting diodes.

List of Figures

Figure 2.1: Geometry of a contact between a sphere and a flat surface. R = radius of the sphere, a = radius of contact area, F_1 = externally applied load.

Figure 2.2: Interaction forces (thicker grey lines) for the different contact models (b-e), plotted in comparison to a realistic interaction [(a) and the lines in (b-e)].

Figure 2.3 : Three modes of crack surface displacements; (a) Mode I (opening or tensile mode); (b) Mode II (sliding mode); and (c) Mode III (tearing mode).

Figure 2.4: Schematic of the components of the path independent J integral.

Figure 2.5 : Interfacial fracture mechanics specimen ; (a) double cleavage drilled compression specimen ($\psi=40^\circ-45^\circ$); (b) mixed-mode flexure specimen; (c) Brazil specimen ($0^\circ \leq \psi \leq 90^\circ$); (d) Dissimilar mixed-mode bending specimen ($0^\circ \leq \psi \leq 90^\circ$).

Figure 2.6: Different types of soft lithography sub techniques; (a) Replica Molding; (b) Microcontact Printing; (c) Micromolding in Capillaries (MIMIC) and (d) Microtransfer Printing.

Figure 2.7: Schematics of (a) subtractive cold welding,(b) additive cold welding and (c) roll-to-roll processing techniques.

Figure 2.8: Schematics of stamping of (a) a metal cathode onto an organic layer and (b) an organic layer on another organic layer in the fabrication of OLEDs.

Figure 2.9: Lamination methods: (a) Soft Contact Lamination of OLEDs; (b) Electric glue-assisted lamination of OLEDs.

Figure 2.10: Conventional methods of encapsulation organic electronic devices (a) rigid lid (b) Coated lid and (c) thin film barrier layer.

Figure 2.11: Effects of micron size particles on the encapsulation of electronic devices (a) contaminating particle at initial stage (b) evolution of contaminants after 120 min oxygen exposure.

Figure 2.12: CB minimum and VB maximum with respect to the vacuum level (EVL) for MoO_3 , V_2O_5 and WO_3 , deduced from UPS and IPES measurements. The ionization energies, work functions and electron affinities are indicated.

Figure 3.1: Schematic of the pressure treatment for the pressure-assisted OLED fabrication process. The device was made with the MoO_3 or PEDOT:PSS as the HIL material. The self-assembled monolayer (SAM) coated anvil was pressed onto the device to add a pressure and then lifted from the device to remove the pressure.

Figure 3.2: FEA Model for the pressure treatment in the pressure-assisted fabrication of OLEDs. The HIL material could be either MoO_3 or PEDOT:PSS.

Figure 3.3: Current-voltage characteristic for (a) MoO_3 -based devices and (b) PEDOT:PSS-based devices before and after pressure treatment.

Figure 3.4: Transmittance spectrum of ITO, MEH:PPV and MoO_3 all deposited on glass.

Figure 3.5: Typical surface profiles of MoO_3 thin film (a) before and (b) after nanoindentation measurement.

Figure 3.6: Reduced Young's modulus and hardness of MoO_3 thin film measured by nanoindentation.

Figure 3.7: FEA predicted contact profile of MoO₃-based device under 14 MPa pressure.

Figure 3.8: The evolution of blister morphology during the pressure treatment with (a) blister radius and area and (b) normalized blister radius and area and the sink-in depth.

Figure 4.1: Schematic Force-Displacement Curve Depicting the Various Stages (A-E) of Cantilever-Surface Engagement.

Figure 4.2: Schematic of (a) model OLED and (b) model HOILED structure.

Figure 4.3: Typical finite element model with initial interfacial crack shown.

Figure 4.4: Sample 3 μm Tapping AFM Height Images for Different Layers in OLED Structures. (a) plain glass, (b) ITO-coated glass, (c) Baytron P VP AL-4083 PEDOT:PSS, (d) MEH:PPV, (e) Al.

Figure 4.5: Typical AFM Force-Displacement Curve Obtained Between MEH: PPV and PEDOT: PSS. In this image, the separation height is 1.611 pixels. With a measured tip spring constant of 0.323 N/m, this corresponds to a pull-off force of 135.2 nN (from Hooke's Law).

Figure 4.6: Summary of measured adhesion forces and energies.

Figure 4.7: Scenarios for AFM Contacts between a Coated AFM Tip (yellow) and Substrate (blue) with: (a) High RMS Surface Roughness and (b) Low RMS Surface Roughness.

Figure 4.8: Dependence of energy release rate on crack size for (a) Al/MEH-PPV, (b) ITO/PEDOT:PSS and (c) MEH-PPV:TiO₂/PEDOT:PSS bimaterial systems subject to different loads. The critical point for interfacial delamination is shown.

Figure 5.1: Instron 5875 microtester setup.

Figure 5.2: Complete Transfer of MEH:PPV on glass.

Figure 5.3: Schematic of transfer printing process with two (2) steps.

Figure 5.4: Force displacement curves from wave maker software during loading, holding and lifting up process.

Figure 5.5: Surface Morphology of laminated MEH-PPV layer on glass.

Figure 5.6: Surface Morphology of laminated MEH-PPV + TiO₂ layer on glass.

Fig 5.7: SEM images of (a) laminated MEH-PPV on glass, (b) laminated MEH-PPV+TiO₂ on glass, (c) spin-coated MEH-PPV on glass and (d) spin-coated MEH-PPV+TiO₂ on glass

Figure 5.8: Dependence of energy release rate on initial interfacial crack size at the top interface (TI) and bottom interface (BI) of a typical tri-layer structure relevant in organic electronics. This is done for device substrate with different stiffness values (EDS).

Figure 5.9: Dependence of energy release rate of top interfacial crack on initial interfacial crack size of bottom interface (BI) in a typical tri-layer structure relevant in organic electronics. This is studied for device substrate with different stiffness values (EDS) and top initial interfacial crack sizes; (a) For a compliant device substrate of stiffness, 3 MPa; (b) For a device substrate with intermediate stiffness of, 100 MPa, and (c) For a stiff device substrate with stiffness, 69 GPa.

Figure 5.10: Dependence of energy release rate of bottom interfacial crack on initial interfacial crack size of bottom interface (BI) in a typical trilayer structure relevant in organic electronics. This is studied for device substrate with different stiffness values (EDS) and top initial interfacial crack sizes; (a) For a compliant device substrate of stiffness, 3 MPa; (b) For a device substrate

with intermediate stiffness of, 100 MPa, and (c) For a stiff device substrate with stiffness, 69 GPa.

Figure 5.11: Dependence of the differential driving force for interfacial crack growth on initial interfacial crack size of bottom interface (BI) in a typical trilayer structure relevant in organic electronics. This is studied for device substrate with different stiffness values (EDS) . The top initial interfacial crack size here is $L_t = 20h$.

Figure 6.1: Schematic of OLED structure used in this study.

Figure 6.2: Flow diagram of the encapsulation process.

Figure 6.3: (a) Diagram showing the Brazil Nut specimen depicting the bi-material surface under consideration and the two possible modes of fracture being investigated; (b) Loading of the Brazil nut specimen.

Figure 6.4: (a) Scanning Electron Microscopy (SEM) image of a coated Atomic Force Microscope tip. (b) Typical displacement curve. Note that the deflection of the tip is graphed on the vertical axis while the out of plane displacement of the cantilever tip is along the horizontal axis. (c) Corresponding physical description of points (A-E) on the displacement curve.

Figure 6.5: Schematic of optical model setup in COMSOL multiphysics.

Figure 6.6: Current-Voltage relationships of encapsulated devices.

Figure 6.7: Electroluminescent spectrum of encapsulated devices.

Figure 6.8: Current-Voltage relationships of encapsulated devices: (a) I-V curves of bare devices recorded daily; showing the effects of degradation. (b) I-V curves of encapsulated devices after 6 days. (c) I-V curves of encapsulated devices after 30 days.

Figure 6.9: Current-Voltage relationships of encapsulated devices before and after elevated temperature and humidity tests.

Figure 6.10: Current-Voltage relationships of encapsulated devices: (a) Before and after 5 minutes of full immersion in water. (b) Before and after 16hrs of full immersion in water.

Figure 6.11: Mechanical robustness of the encapsulated device. (a) Result of the Brazil nut tests. (b) Adhesion energies.

Figure 6.12: Electroluminescence spectra of OLED obtained through optical modeling with COMSOL Multiphysics; (a) EL spectrum of simulated bare device; (b) EL spectrum of simulated bare device compared with its encapsulated counterpart; (c) EL spectrum of simulated bare device compared with the experimental bare device.

List of Abbreviations and Symbols

OLED	Organic Light Emitting Diode
PEDOT: PSS	Poly-(3, 4-ethylenedioxythiophene): poly-(p-styrenesulfonate)
ITO	Indium Tin Oxide
HOMO	Highest Occupied Molecular Orbital
TMO	Transition Metal Oxide
HILM	Hole Injection Layer Material
HDPE	High Density Poly Ethylene
PDMS	Polydimethyl Siloxane
JKR	Johnson-Kendall-Roberts
DMT	Derjaguin-Muller-Toporov
MD	Maugis-Dugdale
AFM	Atomic Force Microscopy
LEFM	Linear Elastic Fracture Mechanics
EPFM	Elastic Plastic Fracture Mechanics
MEMs	Micro Electro Mechanical systems

ODT	Octadecanethiol
OTFT	Organic Thin-Film Transistor
SCL	Soft Contact Lamination
AMOLED	Active Matrix OLED
WVTR	Water Vapor Transmission Rate
OTR	Oxygen Transmission Rate
OPV	Organic PhotoVoltaic
SEM	Scanning Electron Microscope
EL	ElectroLuminescence
HTM	Hole Transport Material
UPS	Ultraviolet Photoemission Spectroscopy
IPES	Inverse Photoemission Spectroscopy
WF	Work Function
IE	Ionization Energy
EA	Electron Affinity
IPA	Isopropyl Alcohol

MEH:PPV	Poly[2-methoxy-5-(2'-ethyl-hexyloxy)-1,4-phenylene vinylene]
FOTCS	(tridecafluoro-1,1,2,2,-tetrahydrooctyl)-trichlorosilane
SAM	Self-Assembled Monolayer
EML	Emissive Layer
HOLED	Hybrid Organic/Inorganic LED
TOLED	Top Emission Organic Light Emitting Diodes
CCBD	Centrally-Cracked Brazilian Disk
FEA	Finite Element Analysis

List of Peer-Reviewed Publications

1. J. Du, **V. C. Anye**, E. O. Vodah, T. Tong, M. G. Zebaze Kana and W. O. Soboyejo, Pressure-assisted fabrication of organic light emitting diodes with MoO₃ hole-injection layer materials, Journal of Applied Physics, 115, 233703 (2014).
2. D.Y. Momodu, T. Tong, M.G. Zebaze Kana, **A. V. Chioh** and W.O. Soboyejo, Adhesion and degradation of organic and hybrid organic-inorganic light-emitting devices, Journal of Applied Physics, 115, 084504 (2014).
3. D.Yu, O.K. Oyewole, D. Kwabi, T. Tong, **V. C. Anye**, J. Asare, E. Rwenyagila, A. Fashina, O. Akogwu, J. Du and W.O. Soboyejo, Adhesion in flexible organic and hybrid organic/inorganic light emitting devices and solar cells, Journal of Applied Physics, 116, 074506 (2014).
4. T. M. Tong, J. Asare, E. R. Rwenyagila, **V. Anye**, O. K. Oyewole, A. A. Fashina and W. O. Soboyejo, “A Study of Factors that Influence the Adoption of Solar Powered Lanterns in a Rural Village in Kenya” PGDT 14(4), 448-491, 2015.
5. O. Oyewole, D. Yu, J. Du, J. Asare, D. O. Oyewole, **V. Anye**, A. Fashina, M. Z. Kana, and W. Soboyejo, “Micro-Wrinkling and Delamination-Induced Buckling of Stretchable Electronic Structures” Accepted for Publication in J. Appl. Phys. 117(23), 2015
6. **V. C. Anye** , W. O. Akande, M.G. Zebaze Kana and W.O. Soboyejo, Encapsulation of Organic Light Emitting Diodes by PDMS Stamping (In preparation for Journal of Applied Physics)
7. **V. C. Anye** ,O.K. Oyewole, J. Asare, E. Rwenyagila, A. Fashina, J. Du, M.G. Zebaze Kana and W.O. Soboyejo, Stamping and Transfer Printing of Organic Light Emitting Diode Layers (In preparation for Journal of Applied Physics)

List of Workshops and Conference Presentations

1. 2013 African Materials Research Society Conference, Addis-Ababa Ethiopia 2013.
2. 2013 Nigerian Materials Congress (NIMACON) 2013, Abuja. Organized by the Materials Society of Nigeria (MSN).
3. 2013 AUST/NASENI Workshop on Nanoscience and Advanced Manufacturing, AUST, Abuja.
4. 2012 Nigerian Materials Congress (NIMACON) 2012, Ile-Ife. Organized by the Materials Society of Nigeria (MSN), Ile-Ife, Osun State, Nigeria.
5. 2011 Workshop on Science and Technology for African Development, AUST – Abuja.
6. 2011 Pan African School on Materials (PASMAT) workshop on Fatigue and Fracture/Phase Diagram (SHETSCO-PRINCETON-AUST Workshop) AUST – Abuja.
7. 2011 Nigerian Materials Congress (NIMACON) 2011, Akure. Organized by the Materials Society of Nigeria (MSN).

Chapter 1

Background and Introduction

1.1 Background

In recent years, much progress has been made in the fabrication of Organic Light Emitting Diodes (OLEDs) [1-6]. Low cost methods such as spin coating [7], screen and inkjet printing [8] have been used to fabricate organic electronic devices that are relevant for OLED applications in display and illumination technologies [6]. Furthermore, OLEDs have received increasing attention over conventional display and solid state lighting counterparts due to their higher resolution and lower power consumption [1, 2, 7]. They are also thinner, light weight and can be built on flexible or stretchable substrates [9]. In a typical device, at least one organic material is sandwiched between two electrodes. Charge carriers are injected from the electrode upon the application of a bias across the device. Holes injected from the anode, recombine with electrons from the cathode and produce excitons that can decay radiatively with the emission of photons. Crucial to the device performance are charge injection, charge transport, exciton formation and relaxation [7, 8].

Poly-(3, 4-ethylenedioxythiophene): poly-(p-styrenesulfonate) (PEDOT: PSS) is often used as the conventional hole transport layer due to its high electrical conductivity [10]. However, PEDOT: PSS is acidic, due to the acidic nature of the PSS dopant. It also etches away In and Sn from the commonly used indium tin oxide (ITO) anode over time. Furthermore, PEDOT: PSS exhibits anisotropic conductivity and its highest occupied molecular orbital (HOMO) energy is

not sufficient to bridge the energy offset with ITO. It is also hygroscopic which results in the undesirable uptake of water into the OLED structure [11]. Transition metal oxides (TMOs) such as NiO, WO₃, V₂O₅ and MoO₃ with electrochromic properties, have been shown to exhibit interesting properties for potential applications as hole injection layer materials (HILMs) in organic photovoltaics and LEDs [12-15].

Nanovoids and impurity particles such as dust (Iron, Aluminum, Silicon, Silicone etc. particles) at the interface between OLED layers promote charge trapping, as well as exciton quenching. They, therefore hinder charge injection and transport. Kim et al. [16] have studied the effects of compression on the performance of OLEDs with small molecule active layer materials. Through ellipsometry measurements of the refractive indices of the films, they noticed that compression treatment of the devices tunes their optical properties. The reason(s) for this is/ARE not fully understood.

Furthermore, a major limitation of organic electronic devices is their short lifetimes. Environmental interactions with the active layers and low work function metals that are used in the device fabrication limit their application/lifetimes in moisture and oxygen-rich environments. Epoxy-glass seals [17] have, therefore, been used for device encapsulation. However, these are not cost-effective. They also, leach into the device active layer during processing and/or in service, which results in severe device degradation. Epoxy-glass seals also add to the weight of the structure, thereby curtailing the lightweight appeal of these structures.

Al-Li and High Density Poly Ethylene (HDPE) multilayer barriers have also been used to successfully encapsulate OLEDs on glass [18]. In most cases, these encapsulation materials have been shown to limit the majority of extrinsic degradation mechanisms (dark spots, bubbles) that

plague OLEDs due to their interactions with oxygen and moisture in the environments encountered during service [18]. Mandlik et al. [19] have also shown that plasma deposited Si_xC_y hybrid layers can be used to extend the lifetimes of encapsulated OLEDs to about 7500h. Although successful, this method requires a complex vacuum deposition procedure and is therefore, not suitable for low-cost applications.

Thermal vacuum evaporation of the metal cathodes and other layers involves temperatures that may be detrimental to the underlying organic layers. Soft-contact lamination is an alternative, cost effective technique for OLED layer deposition. It can be used in large area fabrication, such as roll-to-roll printing [19-20]. Tucker et al. [21] have also used finite element simulation to study the transfer printing of layers that are associated with organic photovoltaics and OLEDs. Their work provides adhesion and fracture mechanics insights for the control of the pull-off process in the transfer printing procedure.

OLED fabrication techniques can also affect the optical properties of the thin film device layers thereby tuning the wavelength of the light they produced [22-23]. However, the mechanisms by which the wavelengths are tuned are not well understood. There is, therefore, a need for further experimental and computational studies of the effects of OLED fabrication techniques on the optical performance of OLED structures. There is also a need for detailed studies of the effects of pressure and interfacial adhesion energy on the surface contacts (between layers) and the current-voltage characteristics of OLED structures with improved hole injection layers, such as MoO_3 . Finally, there is a need to study the effects of encapsulation on the service lives of OLED structures.

1.2 Research Objectives

In an effort to overcome some of the challenges associated with the use of PEDOT: PSS as a hole injection layer material (HILM), we explore the use of a transition metal oxide (TMO) such as molybdenum trioxide (MoO_3), as a hole injection layer in this work. We also examine the effects of pressure on the surface contacts and the current-voltage characteristics of OLEDs with HILMs produced from MoO_3 HILM.

Also, in an effort to improve the lifetimes of OLEDs, a novel cost-effective device encapsulation technique is explored. The cost-effective technique uses polydimethyl siloxane (PDMS) for the encapsulation of OLEDs.

In an effort to develop low cost manufacturing techniques, soft-contact lamination is explored for the transfer of layer films onto OLED structures. This is a technique that limits thermally-induced stresses and protects the underlying layers from degradation during device fabrication.

Finally, optical simulations of light propagation (through the OLED structure) are used to explain shifts in wavelength of the light that are produced by device processing techniques. The implications of the optical simulations are discussed for the tuning of devices and the control of the optical properties of the device layers.

1.3 Scope and Organization of Thesis

Following the background and introduction in chapter 1, chapter 2 presents a review of the current literature on adhesion/contact theories, the fundamentals of fracture mechanics, and lamination techniques for the deposition of layers that are relevant to organic electronic structures and encapsulation protocols for prolonging the lifetime of OLEDs.

The effects of pressure are examined in Chapter 3 using a combination of experiments and finite element simulations. The computational studies of surface contacts are used to explain the trends in the measured current-voltage characteristics of model OLED structures with PEDOT: PSS as a HIL (control) or MoO₃ as an improved HIL (test).

Chapters 4, explore the effects of interfacial adhesion on the reliability of OLEDs. Force microscopy is used to measure the adhesion between adjacent layers in model multilayered OLED structures. These include the following interactions: organic/organic interfaces, organic/inorganic interfaces and metal/organic interfaces.

A soft-contact lamination process for the effective transfer of relevant OLED layers is presented in chapter 5. Finite element simulations are also used to study the effects of surface contacts and interfacial fracture during the contact and pull-off stages of soft-contact lamination. The results are used to provide insights into the conditions required for successful, unsuccessful or partial transfer of the thin film layer during soft lamination processes.

In chapter 6, we explore the encapsulation of fabricated OLEDs. The encapsulation procedure, which uses PDMS as the encapsulation material, results in an optical tuning of the system i.e. -a red shift in the optical spectra of the resulting OLEDs. Optical simulations are carried out using the COMSOL Multiphysics software package. The finite element simulations are used to explain the observed red shift, before discussing the implications of the results for the tuning of OLEDs and the design of encapsulation.

Lastly, chapter 7 presents the conclusions arising from the current study, along with some suggestions for future research.

References

- [1] C.W. Tang, S.A. Van Slyke, “Organic Electroluminescent diodes”, Appl. Phys. Lett. 51, 913 (1987).
- [2] R.H. Friend, R.W. Gymer, A.B. Holmes, J.H. Burroughes, R.N. Marks, C. Taliani, D.D.C. Bradley, D.A. Dos Santos, J.L. Bredas, and M. Löglund, W.R.Salaneck,” Electroluminescence in conjugated polymers”, Nature, 397,121(1999).
- [3] T. Tong, B. Babatope, S. Admassie, J. Meng, O. Akogwu, W. Akande, and W. O. Soboyejo, “Adhesion in organic electronic structures”, , J. Appl. Phys., 106, 083708 (2009).
- [4] J.H. Burroughes, D.D. C. Bradley, A.R. Brown, R.N. Marks, K. Mackay, R. H. Friend, P.L. Burn and A. B. Holmes, “ Light-emitting diodes based on conjugated polymers”, Nature 347 539(1990).
- [5] J. Zmija, M.J. Malachowski, “Organic Light Emitting Diodes Operation in displays”, Arch. Mater. Sci. Eng. 40, 5(2009).
- [6] Wali O. Akande, Onobu Akogwu, Tiffany Tong, and Wole Soboyejo, “Thermally induced surface instabilities in polymer light emitting diodes”, J. Appl. Phys. 108, 023510(2010).
- [7] Z. Ge, T. Hayakawa, S. Ando, M. Ueda, T. Akike, H. Miyamoto, T. Kajita and M. Kakimoto, “Spin-Coated Highly Efficient Phosphoresce Organic Light-Emitting Diodes Based on Bipolar Triphenylamine-Benzimidazole Derivatives”, Adv. Func. Mat. 18,584 (2008).
- [8] T.R. Hebner, C.C. Wu, D. Marcy, M.H. Lu and J.C. Sturm , “Ink-jet printing of doped polymers for organic light emitting devices”, Appl. Phys. Lett. 72, 519 (1998).

- [9] M. Ramuz, B. Tee, J. Tok and Z. Bao, "Transparent, Optical, Pressure-Sensitive Artificial Skin for Large-Area Stretchable Electronics", *Adv. Mat.* 24,3223 (2012)
- [10] P.A. Levermore, L. Chen, X. Wang, R. Das and D.D. C. Bradley, "Fabrication of Highly Conductive Poly (3,4,-ethylenedioxythiophene) Films by Vapor Phase Polymerization and their Application in Efficient Organic Light-Emitting Diodes", *Adv. Mat.* 19, 2379 (2007).
- [11] F. Huang, Y. Cheng, Y. Zhang, M. Liu and A. Jen, "Crosslinkable hole-transporting materials for solution processed polymer light-emitting diodes", *J. Mater. Chem.* 18, 4495 (2008).
- [12] J. Meyer, K. Zilberberg, T. Riedl and A. Kahn, "Electronic Structure of Vanadium pentoxide: An efficient hole injector for organic electronic materials", *J. Appl. Phy.* 110, 033710(2011).
- [13] K. X. Steirer, J. P. Chesin, N. E. Widjonarko, J. J. Berry, A. Miedaner, D. S. Ginley, and D. C. Olson, "Solution deposited NiO thin-films as hole transport layers in organic photovoltaics", *Org. Electron.*, 11, 1414(2010).
- [14] J. Meyer, R. Khalandovsky, P. Görrn, and A. Kahn, "MoO₃ Films Spin-Coated from a Nanoparticle Suspension for Efficient Hole-Injection in Organic Electronics", *Adv. Mater.*, 23, 70(2011).
- [15] K. Zilberberg, S. Trost, H. Schmidt and T. Riedl, "Solution Processed Vanadium Pentoxide as Charge Extraction Layer for Organic Solar Cells", *Adv. En. Mater.* 1, 377(2011).

- [16] J.H. Kim, S. Seo and H.H. Lee, “Nanovoid nature and Compression Effects in organic light emitting diode”, *Appl. Phys. Lett.* 90, 143521 (2007).
- [17] J. McElvain, H. Antoniadis, M. Hueschen, J. Miller, D. Roitman, J. Sheats, and R. Moon, “Formation and growth of black spots in organic light-emitting diodes”, *J. Appl. Phys.* 80, 6003 (1996).
- [18] S.H. Kwon, S.Y. Paik, O.J. Kwon, and J.S. Yoo, “Triple-layer passivation for longevity of polymer light-emitting diode”, *Appl. Phys. Lett.* 79, 4450 (2001).
- [19] P. Mandlik, J. Gartside, L. Han, I-C. Cheng, S. Wagner, A.J. Silvernail, R. Ma, M. Hack and J.J. Brown, “A single-layer permeation barrier for organic light-emitting displays”, *Appl. Phys. Lett.* 92, 103309 (2008).
- [20] J.W.P. Hsu, “Soft lithography contacts to organics”. *Mater. Today* 8, 42 (2005).
- [21] M. B. Tucker, D. R. Hines, and Teng Li, “A quality map of transfer printing”, *J. Appl. Phys.*, 106, 103504 (2009)
- [22] V. Bulovic, R. Deshpande, M. E. Thompson, and S.R. Forest, “Tuning the color emission of thin film molecular organic light emitting devices by the solid state solvation effect”, *Chem. Phys. Lett.*, 308, 317 (1999).
- [23] T. Tsuzuki, N. Shirasawa, T. Suzuki, and S. Tokito, “Color Tunable Organic Light-Emitting Diodes Using Pentafluorophenyl-Substituted Iridium Complexes”, *Adv. Mater.*, 15, 1455 (2003).

Chapter 2

Literature Review

2.1 Adhesion and Contact Deformation Theories

The pioneer classical theory of contact was developed by Hertz [1] in 1881. He assumed that there is no adhesion between two elastic spheres in contact. Figure 2.1 shows the geometry of a sphere in contact with a flat surface. The Johnson-Kendall-Roberts (JKR) model [2] describes the contact between compliant materials with short range, strong adhesion forces, and large tip radii. In contrast, the Derjaguin-Muller-Toporov (DMT) model [3] applies to adhesion between stiff materials with long range, weak adhesion forces, and small tip radii. In this regime, the adhesion forces can be estimated by the following two limiting cases: (i) The JKR theory, and (ii) the DMT model.

The JKR theory [2] is suitable for highly adhesive systems with low stiffness and large tip radii. One difficulty with the JKR theory is that it predicts an infinite stress at the edge of the contact area. This unphysical situation arises because the JKR considers only forces inside the contact area and implicitly assumes that the attractive forces act over an infinitesimally small range. These singularities disappear when a finite range force law such as the Lennard-Jones potential, is assumed. On the other hand, the Derjaguin-Muller-Toporov (DMT) model [3], which describes well the case of long range surface forces with a Hertzian geometry (i.e. stiff materials, weak adhesion forces), considers adhesive interactions outside the contact area. Intermediate

between the JKR and DMT models, is the Maugis-Dugdale (MD) model [4] which proposes an analytical solution.

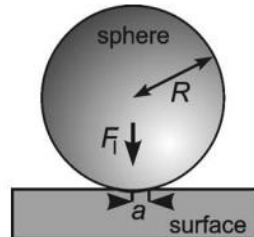


Figure 2.1: Geometry of a contact between a sphere and a flat surface. R = radius of the sphere, a = radius of contact area, F_1 = externally applied load.

Figure 2.2 (b)-(d) [5] compares the interaction forces (per unit area) for the Hertz, JKR and DMT models with the realistic interaction. In the Hertz model, there is no attractive force, only hard wall repulsion at the contact. The JKR model represents short range adhesion, which can be described by a delta function with strength γ and short-range contact zone. The DMT model represents a long-range surface force, which has a Hertzian contact profile, with an additional external load as attractive forces. For realistic interactions, the integral of the force-distance attractive well, for example Lennard-Jones potential, corresponds to the work of adhesion, i.e. adhesion energy, γ .

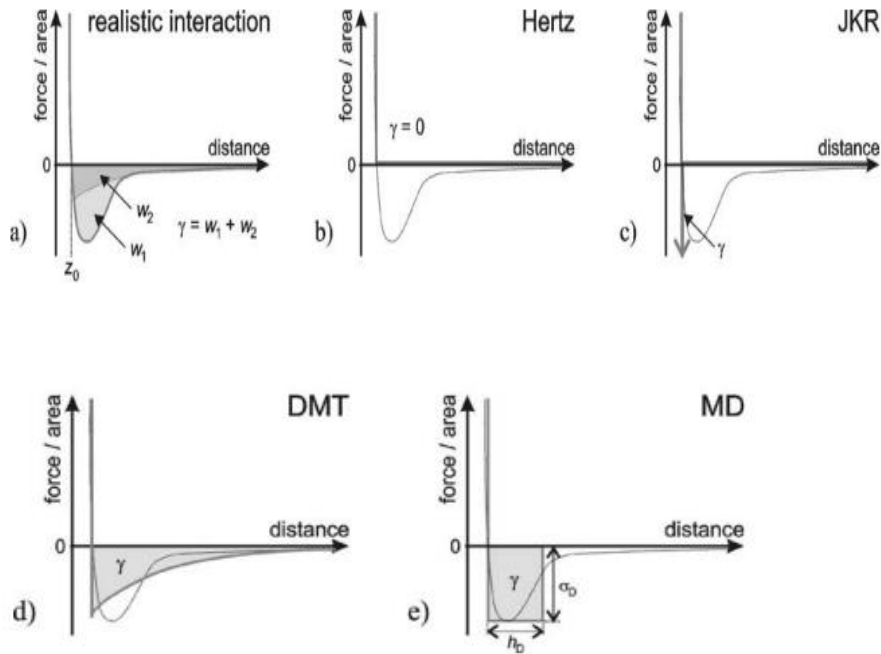


Figure 2.2: Interaction forces (thicker grey lines) for the different contact models (b-e), plotted in comparison to a realistic interaction [(a) and the lines in (b-e)]. All the forces are given per unit area with the shaded area representing the work of adhesion, γ . Attractive forces are not included in the Hertz model (a), whereas they are considered by a delta function in the JKR model (c), a long-range force in the DMT model (d), a step function (Dugdale force) in the MD model (e).

Figure 2.2(e) [5] shows the force-distance relation in the Maugis-Dugdale (MD) model, which is an analytical solution in the intermediate regime between the JKR and DMT models. Maugis [5] used a Dugdale square well potential to approximate the interaction potential in reality. In this interaction, a uniform adhesive stress (force per unit area) σ_0 acts between the surfaces over a

range of δ_t . Therefore, the work of adhesion, i.e. adhesion energy, can be calculated as $\gamma = \sigma_0 \delta_t$.

To select the appropriate model, Maugis [4] defined a transition parameter, λ , which is given by:

$$\lambda = 2\sigma_0 \left(\frac{R}{\pi\kappa^2\gamma} \right)^{1/3} \quad (2-1)$$

where γ is the adhesion energy per unit area; R is the combined radius given by

$$R = R_1 R_2 / (R_1 + R_2) \quad (2-2)$$

where R_1 and R_2 are the radii of the two spheres; κ is the combined elastic modulus for two spheres in contact. κ is given by

$$\kappa = \frac{4}{3} \left[\frac{(1-\nu_1^2)}{E_1} + \frac{(1-\nu_2^2)}{E_2} \right]^{-1} \quad (2-3)$$

where E_1 and E_2 are the elastic moduli of the two spheres, and ν_1 and ν_2 are the Poisson's ratios of the two spheres. In choosing σ_0 to match the minimum adhesive stress of a Lennard-Jones potential with equilibrium separation distance, z_0 , (Figure 2.2(a)), it follows that $\delta_t = 0.97z_0$

The JKR model is suitable when $\lambda > 5$. The DMT model applies when $\lambda < 0.1$. The MD model applies for the intermediate values of λ .

In the non-zero adhesion cases, the negative critical load at which the surfaces of two spheres separate, when being pulled apart, is defined as the pull-off force or adhesion force. For the two extreme cases, it is given in DMT and JKR theories, respectively, by:

$$F_{DMT} = 2\pi\gamma R \quad (2-4)$$

$$F_{JKR} = \frac{3}{2}\pi\gamma R \quad (2-5)$$

In the MD model, two equations are desired to relate the contact radius, a , and the contact force, F :

$$\frac{\lambda\hat{a}^2}{2} \left[\sqrt{m^2-1} + (m^2-2)\cos^{-1}\left(\frac{1}{m}\right) \right] + \frac{4\lambda\hat{a}^2}{2} \left[\sqrt{m^2-1}\cos^{-1}\left(\frac{1}{m}\right) + -m+1 \right] = 1 \quad (2-6)$$

$$\hat{F} = \hat{a}^3 - \lambda\hat{a}^2 \left[\sqrt{m^2-1} + m^2\cos^{-1}\left(\frac{1}{m}\right) \right] \quad (2-7)$$

where \hat{a} and \hat{F} are two dimensionless parameters defined by:

$$\hat{a} = \frac{a}{(\pi\gamma R^2/\kappa)^{1/3}} \quad (2-8)$$

$$\hat{F} = \frac{F}{\pi\gamma R} \quad (2-9)$$

and the parameter m represents the ratio between the contact radius, a , and an outer radius, c , when the gap between the sphere surfaces reaches δ_t , i.e., where the adhesion no longer occurs. However, the above equations are difficult to use, since there is not a single expression relating only a and F . Equations (2-6) and (2-7) need to be solved simultaneously by letting m vary suitably between limits, which depend upon λ . Furthermore, in the usual case with experimental measurements, such as AFM force measurement, the value of λ is an unknown. The relation for the pull-off force must therefore, be determined through an iterative procedure [6].

Carpick et al. [5] proposed that the relation between contact radius a and the contact radius at zero load, a_0 , can be described by a generalized equation

$$\frac{a}{a_0} = \left(\frac{\alpha + \sqrt{1 - F/F_{ad}}}{1 + \alpha} \right)^{2/3} \quad (2-10)$$

where F_{ad} is the general adhesion force. The JKR model is applicable when $\alpha=1$ while $\alpha=0$ represents the DMT model. They showed that for intermediate cases, for which $0 < \alpha < 1$, the generalized transition equation agrees very closely to solutions furnished by Maugis using the Dugdale model. By curve fitting, they also provided a conversion equation from α to λ :

$$\lambda = -0.924 \ln(1 - 1.02\alpha) \quad (2-11)$$

Equation (2-11) was later modified by Pietrement and Troyon [7] through fitting to be

$$\lambda = -0.913 \ln(1 - 1.018\alpha) \quad (2-12)$$

Applying Equation (2-9) to adhesive forces gives

$$\hat{F}_{ad} = \frac{F_{ad}}{\pi\gamma R} \quad (2-13)$$

They also determined empirical equations supplying direct conversion equations between parameter α and F_{ad}

$$\hat{F}_{ad} = 0.267\alpha^2 - 0.767\alpha + 2.00 \quad (2-14)$$

The AFM measurement gives F_{ad} . With R and κ known, the adhesion energy can be calculated by solving the Equations (2-1), (2-12), (2-13) and (2-14).

In this section, we have reviewed prior theories [1–4] for the characterization of the contact adhesive interactions. These theories provide methods to characterize the adhesion between two elastic spheres in contact. They can also be used to estimate the adhesion energies from atomic force microscopy (AFM) experiments.

2.2 Fundamentals of Fracture Mechanics

Interfacial crack nucleation and growth occurs when the adhesion between two contacting bodies is broken. To succinctly describe this phenomenon in terms of interfacial bonding and strength, we present some basic concepts in fracture mechanics in this section.

2.2.1 Fundamentals of Linear Elastic Fracture Mechanics (LEFM)

Crack growth occurs through three different modes [8]. These modes of fracture are shown schematically in Figure 2.3. Mode I is the crack opening or tensile mode. It is the most damaging of all the three fracture modes. Mode II is called the in-plane shear or sliding mode, while mode III is the out-of-plane shear or tearing mode. These three modes can either occur independently or concurrently. The expressions for the crack-tip stress fields for linear elastic conditions are given by [8]:

$$[\sigma_{ij}]_M = \frac{K_M}{\sqrt{2\pi r}} [\tilde{\sigma}_{ij}(\theta)]_M \quad (2-15)$$

where the subscript M refers to a given crack growth mode (Mode I, II, or III), σ_{ij} is the stress, r and θ are the coordinates in the polar coordinate system whose origin is at the crack tip.

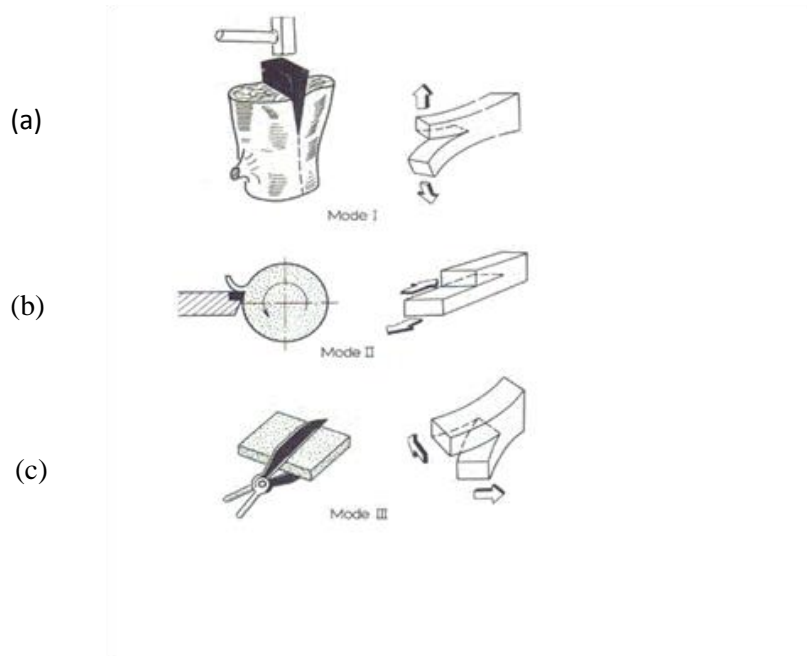


Figure 2.3 : Three modes of crack surface displacements; (a) Mode I (opening or tensile mode); (b) Mode II (sliding mode); and (c) Mode III (tearing mode)

(From Parton V.Z. *Fracture Mechanics from Theory to Practice*, Pg. 66, Fig. 47, Gordon and Breach Science Publishers)

From equation (2-15), it is clear that, for a given fracture mode, the functional dependence of the crack-tip fields is similar, with the exception of the scaling factor, K . Therefore, K can be used to represent the amplitude of the crack-tip fields. It essentially corresponds to the driving force for crack growth under LEFM conditions. In general, the stress intensity factor, K , is often expressed as [8]:

$$K = f(a/w) \sigma \sqrt{\pi a} \quad (2-16)$$

where σ is the applied remote stress, $f(a/w)$ is a function of the crack length, a and the specimen width, w .

It is clear from equation (2-15), that there is a singularity of stress at the crack tip. Since infinite stresses cannot be supported in the crack-tip regime, yielding occurs in an annular region around the crack-tip. This results in the formation of a plastic zone, around the crack tip. Nevertheless, linear elastic fracture mechanics (LEFM) is still valid when the plastic zone size, r_p , is small compared to the crack length, a ($r_p < a/50$). When this is so, a linear relationship is generally observed between the applied force and the crack opening displacement, until the onset of stable crack growth and catastrophic failure.

Since there is a high stress concentration in the region surrounding the crack tip, strain energy is stored within this regime. Also, as the crack extends into the region of high stress concentration, the strain energy is released. The energy release rates for modes I, II and III crack growth modes can be added algebraically since energy is a scalar. For a three dimensional solid subjected to all three modes of crack growth simultaneously, the energy release rate is given by:

$$G = G_I + G_{II} + G_{III} \quad (2-17)$$

$$\text{where } G_I = K_I^2 / E', G_{II} = K_{II}^2 / E', G_{III} = K_{III}^2 / 2\mu = (1+\nu) K_{II}^2 / E'$$

where, E is the Young's modulus, μ is the shear modulus and ν is the Poisson's ratio,

$E' = E$ for plane stress conditions and $E' = E/(1-\nu^2)$ for plane strain conditions.

Thus we obtain [9]:

$$G = \frac{1}{E} (K_I^2 + K_{II}^2) \quad (\text{for plane stress}) \quad (2-18)$$

and

$$G = \frac{(1-\nu^2)}{E} (K_I^2 + K_{II}^2) + \frac{1+\nu}{E} K_{III}^2 \quad (\text{for plane strain}) \quad (2-19)$$

2.2.2 Fundamentals of Elastic-Plastic Fracture Mechanics (EPFM)

The small-scale plasticity assumption is invalid when the plastic zone sizes are large compared to the crack size. In such cases, LEFM is not valid and alternative methods, such as the J integral approach, are needed to describe the crack driving forces associated with elastic-plastic fracture.

The J integral approach was proposed by Rice and Rosengren [10] for a non-linear elastic solid.

It is given by:

$$J = \int_{\Gamma} \left(W dy - T \frac{du}{dx} ds \right) \quad (2-20)$$

where Γ is an arbitrary counterclockwise closed contour in a stressed solid, T is the traction force perpendicular to Γ in an outward facing direction, u is the displacement in the x direction, ds is an element of Γ (Figure 2.4) and W is the strain energy density.

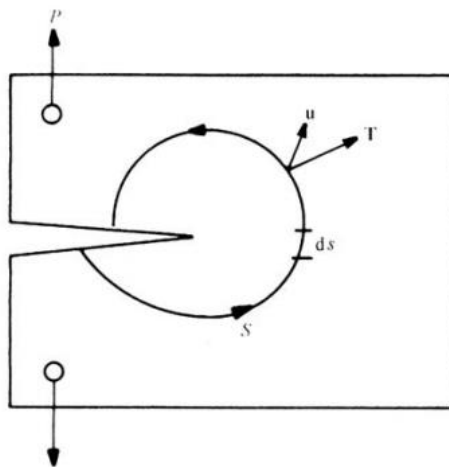


Figure 2.4: Schematic of the components of the path independent J integral [8].

Later, Begley and Landes [11-12] showed that J provides a measure of the driving force for crack growth under elastic-plastic fracture mechanics conditions.

For a nonlinear elastic solid, the J integral is defined as the change in potential energy for a virtual crack extension by Rice [13]. It is a path-independent integral that relies on the determination of an energy term, which expresses the change in potential energy, when a crack is virtually extended by a distance. It is analogous to the strain energy release rate, G , which is used under the linear elastic condition. For a linear elastic material, $J=G$. The J integral is only applicable when the following two conditions for J dominance proposed by Hutchinson [14] are satisfied:

1. The J_2 deformation theory of plasticity must provide an adequate model for the small-strain behavior of real elastic-plastic materials under the monotonic loading.
2. The regions in which finite strain effects are important and the region in which microscopic processes occur must be contained within the region of the small-strain solution dominated by the singularity fields.

2.2.3 Interfacial Fracture Mechanics

Crack nucleation and growth at the interfaces of dissimilar materials is more complex than in the bulk of a homogeneous material. This complexity arises as a result of the oscillatory singularity of the interfacial crack-tip fields in the presence of mode mixity. In order to analyze fracture in this situation, we require crack driving forces and fracture criteria that are mode mixity-dependent.

For two isotropic elastic solids joined along the x-axis, say, with material 1 above the interface and material 2 below, we define Dundurs' elastic mismatch parameters [15] as:

$$\alpha = \frac{\mu_1(\kappa_2 + 1) - \mu_2(\kappa_1 + 1)}{\mu_1(\kappa_2 + 1) + \mu_2(\kappa_1 + 1)}$$

and

$$\beta = \frac{\mu_1(\kappa_2 - 1) - \mu_2(\kappa_1 - 1)}{\mu_1(\kappa_2 + 1) + \mu_2(\kappa_1 + 1)} \quad (2-21)$$

where $\kappa_i = 3 - 4\nu_i$ for plane strain and $\kappa_i = \frac{3 - 4\nu_i}{1 + \nu_i}$ for plane stress

μ_i , and $\nu_i (i=1,2)$ are the shear modulus and Poisson's ratio of the respective materials.

The mismatch in the plane tensile modulus is measured by the parameter α while the parameter β measures the mismatch in the in-plane bulk modulus.

Solutions to bimaterial interface crack problems were presented by England [16], Erdogan [17], Rice and Sih [18]. Traction on the interface directly ahead of the tip are given by

$$\sigma_{22} + i\sigma_{12} = \frac{Kr^{i\epsilon}}{\sqrt{2\pi r}} \quad (2-22)$$

where $K = K_1 + iK_2$ is the complex interface stress intensity factor. It has real and imaginary parts K_1 and K_2 , respectively, that play the same role as in the case of a crack in a homogeneous isotropic solid.

Also,

$$\varepsilon = \frac{1}{2\pi} \ln \left(\frac{\mu_1 + \mu_2 (3 - 4\nu_1)}{\mu_2 + \mu_1 (3 - 4\nu_2)} \right) \quad (2-23)$$

Equation (2-23) represents the so-called oscillatory singularity that captures some complications that are not present in the elastic fracture mechanics of homogeneous solids. Combining the two stress intensity factors, gives rise to two alternative parameters, the energy release rate, G , and the mode mixity angle, ψ . They represent a more useful and practical measure of interface crack growth. The energy release rate, G , is given by Malyshev and Salganik [19]:

$$G = \frac{1 - \beta^2}{\hat{E}} (K_1^2 + K_2^2) \quad (2-24)$$

$$\text{Where } \frac{1}{\hat{E}} = \frac{1}{2} \left(\frac{1}{\bar{E}_1} + \frac{1}{\bar{E}_2} \right) \quad (2-25)$$

$$\bar{E}_i = \frac{E_i}{1 - \nu_i^2} \quad (\text{for plane strain})$$

$$\text{and } \bar{E} = E_i \quad (\text{for plane stress})$$

The mode mixity angle, ψ , is defined by:

$$\psi = \tan^{-1} \left(\frac{K_{II}}{K_I} \right) \quad (2-26)$$

The criterion for crack growth is defined by Hutchinson and Suo [20] as G reaches a critical value, the interfacial toughness, Γ_i . Hence, to analyze the reliability of an interface within a joint, (1) the energy release rate has to be calculated through the finite element method and the above equations, and (2) the mixity-dependent interfacial toughness has to be measured for that specific interface using laboratory specimens that duplicate the stress states at the interface.

Conducting experimental studies on interfacial fractures is more challenging than the corresponding studies performed on single materials. When interfaces are bonded by procedures, such as sintering or adhesive bond, to make layered specimens, a number of laboratory specimen geometries (Figure 2.5) are proposed. The mode mixity angles for most of these specimens are limited to relatively narrow ranges (Figure 2.5). It is, therefore, common to use a range of fracture mechanics specimens to obtain the full range of interfacial fracture toughness values for mode mixities between pure mode I and pure mode II. The dissimilar mixed mode bend specimen (Figure 2.5(d)), suggested by Soboyejo et al. [21], and the Brazil specimen (Figure 2.5(c)) suggested by Hutchinson and Suo [20], can provide measurements of interfacial fracture toughness values for the full range of mode mixities.

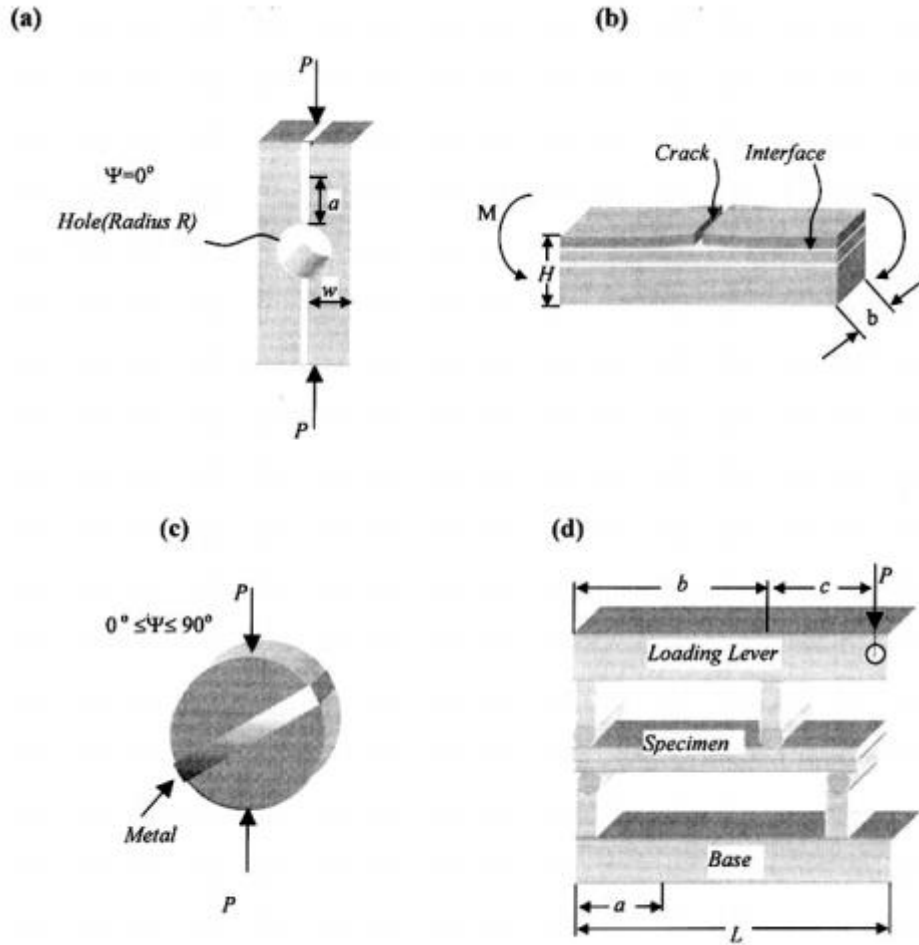


Figure 2.5 : Interfacial fracture mechanics specimen [8]; (a) double cleavage drilled compression specimen ($\psi=40^{\circ}$ - 45°); (b) mixed-mode flexure specimen; (c) Brazil specimen ($0^{\circ}\leq\psi\leq90^{\circ}$); (d) Dissimilar mixed-mode bending specimen ($0^{\circ}\leq\psi\leq90^{\circ}$).

There have been some experiments of interfacial fracture between dissimilar materials. The systems exhibited resistance-curve behavior and resulted in fracture energies that are significantly greater than the thermodynamic work of adhesion. Also, the study by Cao and Evans [22] and the study by Soboyejo et al. [21], both showed that the interfacial fracture toughness varies appreciably with mode mixity. The above phenomena are due to crack-tip shielding by ductile ligaments; plastic dissipation in the substrate; and friction at asperities at the crack surfaces. Furthermore, Evans and Dalgleish [23] showed that the crack could either grow

along the interface or inside the substrate materials. The crack-path selection criteria for cracks between dissimilar solids depend, not only on the ratio of interfacial toughness, Γ_i , to the substrate toughness, Γ_s , of the adjacent material, but also on the mode mixity angle, ψ .

2.3 Lamination and stamping of Organic Light Emitting Diode layers

Electroluminescence was first observed in small organic molecules by Pope et al. [24]. A device was later on constructed using organic molecules by Tang and Van Slyke [25]. Since the early work [24,25], several studies have been carried out on organic light emitting diodes (OLEDs) and other organic electronic devices that are low-cost alternatives to conventional silicon-based devices. Although the field of organic electronics is relatively new, compared to silicon electronics, the performance improvements in these structures have already triggered great commercial interest [26].

2.3.1 Alternative Schemes for the Fabrication of Organic Electronic Devices

(a) Soft lithography

There are several unconventional methods for the fabrication processes of OLEDs and other organic electronic devices. Xia et al. [27–29] reviewed a series of soft lithography methods for the micro- and nanofabrication of organic polymeric materials. Soft lithography is a rapidly emerging technique commonly used in producing nanotechnology related devices. It can be used for the production of lab-on-chip systems, bio surfaces, biochips, microfluidics, micro reactors, sensors, microelectromechanical systems (MEMS), micro optics etc [28, 29]. It is also an alternative to photolithography and electron beam lithography because it is cost effective and allows the creation of three dimensional patterns at room temperature and pressure.

Soft lithography utilizes cast molded stamps made from elastomeric or flexible materials, such as polydimethyl siloxane (PDMS). Since the stamp is flexible, the substrate material need not be perfectly flat. It can be spherically curved, flat curved or even contain surface features. Some common soft lithography patterning techniques include, among others, replica molding, microcontact printing, micromolding and microtransfer printing [27].

Figure 2.6 presents schematics of the above techniques. In replica molding, after a PDMS stamp is made from the original master (usually silicon wafer), it is used as a secondary master and another stamp produced from it. The original master can, therefore, be preserved as multiple copies are made. Microcontact printing technique involves ‘inking’ the stamp with preselected chemicals, usually alkanethiols like octadecanethiol (ODT). It is then pressed onto the substrate and removed, leaving behind a one molecule thick layer with features as small as 300 nm.

In micromolding , the stamp is brought in contact with a solid substrate and capillary action is used to add a polymer material to the channels (Figure 2.6 (c)). The polymer is cured and the stamp removed leaving a pattern with features as small as 1 μm . Microtransfer molding on the other hand, requires a pre-polymer or ceramic precursor to be added to the stamp that is placed on a substrate (Figure 2.6(c)). After curing, the stamp is removed leaving behind a pattern with features down to 250 nm.

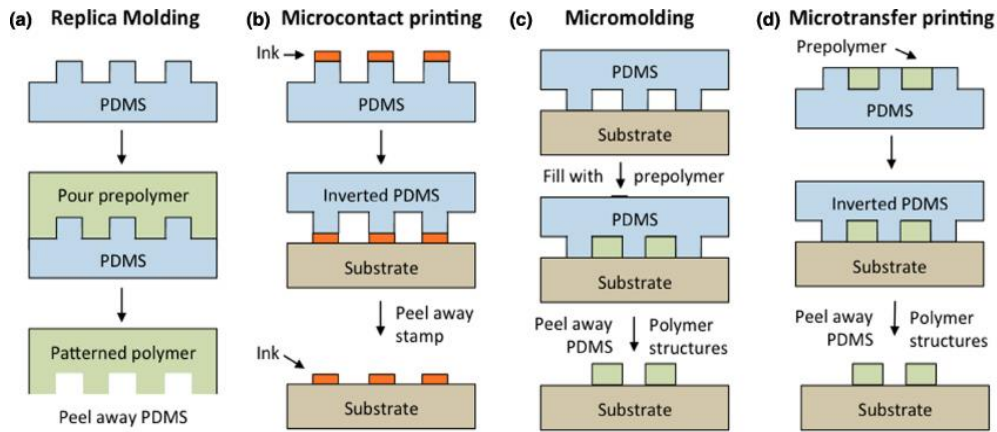


Figure 2.6 : Different types of soft lithography sub techniques; (a) Replica Molding; (b) Microcontact Printing; (c) Micromolding in Capillaries (MIMIC) and (d) Microtransfer Printing.

(b) Cold Welding

Cold welding is a technique that joins two metallic surfaces together by forming metallic bonds under room temperature. This technique was used by Kim et al. [30–32], as shown in Figure 2.7(a) and (b), to pattern the metallic electrode after the organic active layer is deposited for the organic light-emitting devices.

In subtractive cold welding [30], as shown in Figure 2.7 (a), submicrometer patterning of the metal electrodes was achieved by pressing a pre-patterned, metal-coated stamp onto the unpatterned organic light-emitting layers to form strong cold welds, and then lifting the stamp to selectively remove the cathode metal. Here, the metal layer subtraction relied on both the cold welds and separation between the metal coating and organic substrate.

In contrast, in additive cold welding [31], upon lifting of the stamp from the substrate, the metal film on the stamp is transferred to the substrate, due to the relatively stronger cold welds and

relatively weaker adhesion of the adhesion reduction layer. This additive [32] process differs from the subtractive process [30] in that it relied only on the delamination in a stamp rather than on a substrate. Therefore, the required pressure ($\sim 150\text{MPa}$) was significantly reduced compared to that for the subtractive method ($\sim 300\text{MPa}$).

Kim et al. [30] have demonstrated the potential to extend the cold welding technique to ultimately result in the printing of large-area organic electronic circuits using roll-to-roll methods, in which the devices are fabricated in a continuous, high-speed, low-cost process (Figure 2.7 (c)). Furthermore, Xu et al. [33] have used the cold-welding processes to enable the direct transfer of metals onto pre-formed hemispheres with micrometer scale feature resolution. This was used to realize 10 kilopixel organic photodetector focal plane arrays (FPAs) that mimic the size, function, and architecture of the human eye.

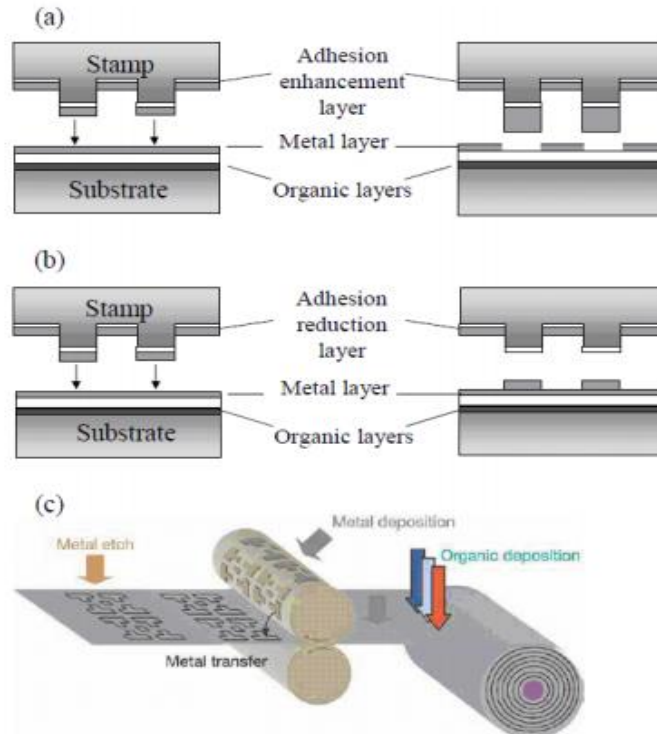


Figure 2.7 : Schematics of (a) subtractive cold welding, (b) additive cold welding and (c) roll-to-roll processing techniques [32].

(c) Stamping

Stamping is a technique that is similar to additive cold welding. In this technique, a stamp is also used to transfer one material onto the other. A self-assembled monolayer (SAM) is usually included between the stamp and the coating to reduce the adhesion between them and facilitate the easy transfer of the coated material to the substrate. The difference between this technique and the cold welding technique is that (1) at least one of the transferred materials and the substrate material is organic polymer and (2) those two materials are joined together by the adhesion between them.

Rhee and Lee [34] used the stamping method in the fabrication of OLEDs. By applying pressure to a metal coated stamp, they were able to transfer the metallic cathode onto the organic active layer of OLEDs, as shown in Figure 2.8(a). Kim et al. [35] have also used stamping to transfer the active organic layer in OLEDs to an organic strike layer. This was achieved by utilizing the adhesion interactions between different organic layers within the OLEDs, as shown in Figure 2.8(b). In a similar manner, Joo et al. [36] used stamping to transfer active organic layers to ITO-coated glass substrates that were used to fabricate polymer light emitting diodes.

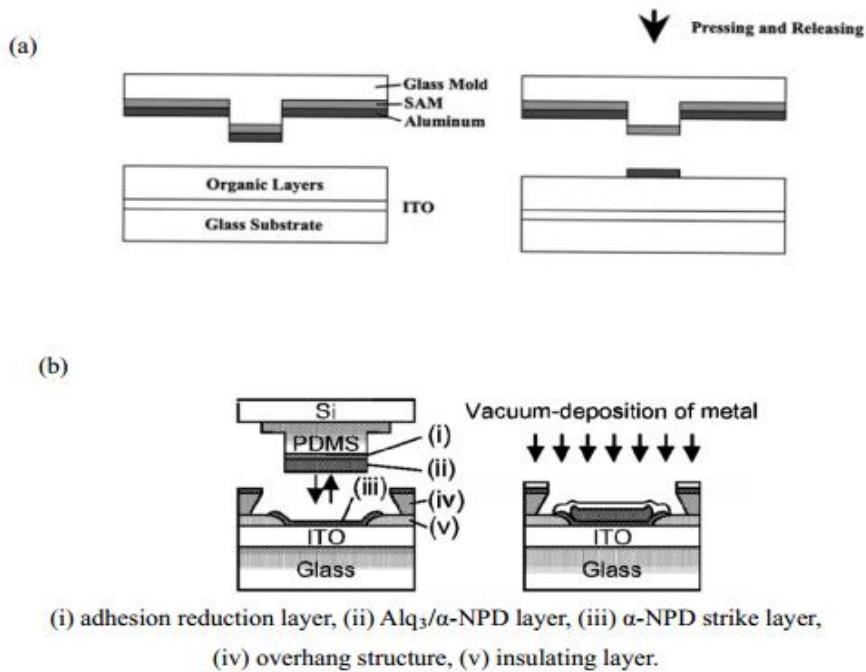


Figure 2.8 : Schematics of stamping of (a) a metal cathode onto an organic layer[34] and (b) an organic layer on another organic layer[35] in the fabrication of OLEDs.

(d) Soft Contact Lamination (SCL)

Lamination is another organic electronic fabrication technique. Instead of transferring materials from one place to another, it gets several layers of materials together into optimal contact to form

the devices. Lee et al. [37] illustrated a soft contact lamination method, as shown in Figure 2.9(a). The patterned OLEDs were built by bringing a patterned metallic electrode layer on a flat elastomer substrate and the active organic layers on an ITO glass substrate into contact. The homogeneous and intimate contact relies only on van der Waals interactions. Hence, it is achieved without applying heat or pressure.

Ouyang et al. [38] fabricated a polymer light-emitting diode through a lamination process in which the adhesion was enabled by a conducting polymer as transparent electric glue (Figure 2.9(b)). The integration of organic thin-film transistor (OTFT) and OLED has been considered as a promising technology for the high-resolution flat panel displays, in which OLEDs can be operated by the OTFT. Zyung et al. [39] fabricated such structure by a lamination method. The OLED and the OTFT were first fabricated on the plastic substrates separately. Then, both devices were laminated by silver paste that acts not only as the adhesive but also the electric connector between the drain electrodes of the OTFT and the anode of the OLED.

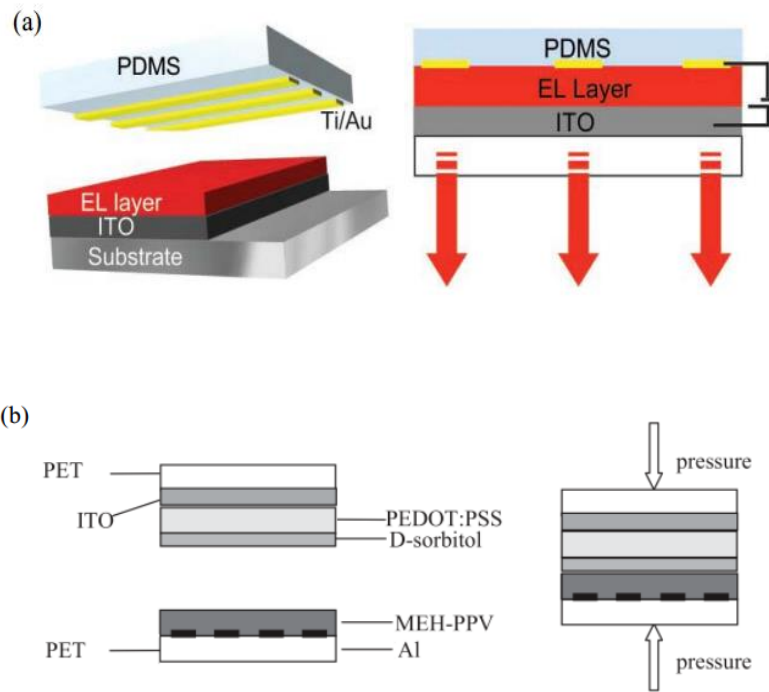


Figure 2.9: Lamination methods: (a) Soft Contact Lamination of OLEDs; (b) Electric glue-assisted lamination of OLEDs.

Soft contact lamination (SCL) [37] is an outstanding example of interfacial engineering in the context of organic electronic devices. As shown in Fig 2.9, the procedure does not consist of transferring material from stamp to substrate. Instead the overall goal of the lamination process is to bring a patterned electrode layer on an elastomeric substrate (PDMS) and the active organic layers (prepared on a rigid or flexible substrate) into optimal contact. Optimal contact is accomplished by employing only the natural van der Waals forces between the PDMS substrate and the active organic layers. In other words, the device configuration is achieved without heat or applied pressure.

Many of the above soft contact devices have achieved greater operating efficiencies than their thermally evaporated counterparts. Their superior performance has been attributed to the

reduction of metal diffusion into the active organic layers. This is normally aided by the high deposition temperatures required by thermal evaporation. The absence of dark-spots after hours of operation typically point towards a high operating lifetime in SCL fabricated devices. This was explained by the lack of pinholes in the elastomeric substrate onto which the electrodes were patterned.

The properties exhibited by SCL and other advantageous lamination processes have prompted the use of laminated devices as model systems for explaining the role of interfaces in the overall electrical performance of organic electronic devices. Chabinye et al. [40] have used laminated OTFTs to study the role of interfaces in determining the overall mobility of charge carriers in fabricated devices. The properties exhibited by laminated devices have also prompted the synthesis of organic semiconductors with specific molecular properties that enable easier use in fabrication scenarios that involve lamination [41].

The versatility and robustness of this fabrication technique was also demonstrated by Liu et al, [42], who fabricated an active matrix OLED pixel (AMOLED) by lamination procedures. This was different from the results obtained by Zyung et al. [39], who used lamination techniques to fabricate an AMOLED circuit coupled to an OTFT.

Apart from lamination-induced advantages, such as increased lifetime and current efficiencies in OLEDs, and enhanced carrier mobilities in OTFTs [40], low materials and processing costs are added incentives for the development of lamination processes. These are, perhaps, the major reasons for the pursuit of lamination fabrication techniques in organic electronic devices.

Furthermore, the lamination process has been used by Kim et al. [43] in the encapsulation of OLEDs. This was done by laminating an adhesive multilayer of polyacrylate-based adhesive

layers and aluminum passivation layers onto the devices. This was done to prevent the degradation of the device.

2.3.2 Contact and Adhesion in Organic Electronic Structures

The performance of organic electronic devices fabricated by the above fabrication methods have been reported to be better than those of the devices fabricated by conventional methods [36]-[37]. The performance of spin-coated and stamped devices have been compared by Joo et al. [36]. They showed that the morphologies of the spin-coated and stamped devices are similar. However, stamped devices were generally better than spin-coated devices, in terms of current density, light-emitting efficiency and lifetime. In particular, the lifetimes of the stamped devices were doubled, compared with those of spin-coated devices.

Devices made by the soft contact lamination method by Lee et al. [37] were also found to have better performance than those fabricated using standard processing techniques, such as direct evaporation of electrodes. Also, much slower growth of “dark spots” was observed in laminated devices than in evaporated ones. The observation indicated that laminated OLEDs have much longer lifetimes than non-laminated devices. Lee et al. [37] suggested that this was because the lamination approach avoids forms of disorder that can be introduced at the electrode/organic interface by metal evaporation and has a reduced sensitivity to pinhole or partial pinhole defects.

Even for those devices fabricated by conventional method, such as chemical vapor deposition, Kim et al. [44] demonstrated a compression treatment similar to the above unconventional fabrication methods. By applying and releasing physical pressure to the devices, a notable increase was observed in the performance of the devices, such as in luminance intensity and current efficiency. Increased pressure led to improved performance. They argued that the

improvement was due to more intimate contact between the organic molecules in the organic layer.

The above studies suggest that the adhesion and contact inside and between each layer of the organic electronic devices are crucial to the performance and the lifetime of OLEDs and organic electronic structures in general. It has also been suggested by Jeng et al. [45] that the surface roughness of the layers in the organic electronic devices influences the injection of hole-carriers. Since the injected current is dominated by the tunneling of hole-carriers at low bias, increasing the effect contact area at the interfaces lowers the barrier to the hole injection in the devices.

There is, therefore, a need to study the fundamental physics of adhesion and contact and their roles in the organic electronic devices. The ensuing insights could clearly lead to the future design of OLEDs and organic electronic structures with superior performance and longer lifetime.

In an effort to guide the design of cold welding processes, Cao et al. [46] conducted finite element simulations of the contact area evolution during the cold welding processes between the layers of organic device due to the dust particles interposed between the interfaces. These simulations showed that, when using an elastomeric soft stamp (PDMS), large areas of contact can be achieved at very low pressures, typically, 100 ~ 1000 times lower than those required for rigid (Si) stamp. Their predictions were consistent with experimental observation of Kim and Forrest [32], who fabricated OLEDs using elastomeric soft stamps at pressures that were ~ 1000 times lower than those required for rigid stamps. This allowed for the application of pressure directly to the device active region, without introducing damage. The simulations of Cao et al. [46] also optimized the thicknesses of the transferred metal films to achieve low resistance, as

well as large area cold-welded contacts. The optimized thickness was consistent with experimental results [32].

Subsequent experimental work by Cao et al. [47] and Akande et al. [48] revealed the role of interfacial impurities, i.e. dust particles, at the cold-welded interfaces between Au and Ag thin films. They also developed a theoretical model to predict the contact profiles around impurities between cold-welded surfaces. These provided new insights into how adhesion affects the surface contacts that occur during cold welding.

Zong et al. [49] presented a study of adhesion energies that are relevant to Au-Au micro-switch contacts at both the nano- and micron-scales. The micron-scale adhesion measurements were obtained from cantilever beam bending measurements and fracture mechanics models. The nanoscale adhesion measurements were achieved by AFM pull-off experiments and adhesion theory models. The adhesion energies obtained for both methods were found to be in good agreement.

Tong et al. [50] also used similar AFM force measurement techniques to measure the adhesion forces between materials relevant to organic solar cells and organic light-emitting devices. The contact pairs included organic-organic, organic-inorganic, and inorganic-inorganic interfaces. The measured pull-off forces and surface parameters were then incorporated into theoretical models for the estimation of surface energies. The results can be used to identify either interfaces with weak adhesion, that need to be modified to reduce the chances of failure, or interfaces with strong adhesion, that would be good candidates for organic electronic devices. However, the use of such adhesion energies in interfacial mechanics has not been fully explored. There is,

therefore, a need to integrate the measurements of adhesion energy with interfacial fracture mechanics models that will access the robustness of OLED structures.

2.4 Encapsulation and Red-Shift in Organic Light Emitting Devices

The active layers of organic electronic devices are sensitive to and react with moisture and oxygen in moisture and oxygen rich environments. The low work function metals used for the device cathodes are also prone to such reactions. This limits their immediate use as the cost effective and accessible alternatives earlier envisaged. In an effort to address this, various encapsulation schemes have been reported [51-53]. Barrier performance values anticipated to be necessary for suitable lifetimes in OLEDs are on the order of 10^{-6} g/m²/day for water vapor transmission rate (WVTR) and 10^{-3} - 10^{-5} cm³/m²/day/atm for Oxygen transmission rate (OTR) [54].

Nevertheless, there is still a need to develop improved encapsulation techniques for many OPVs and OLEDs. There is also the potential to use the improved encapsulation techniques to improve the reliability and lifetimes of the devices.

The conventional methods of encapsulating organic devices include: rigid lid, coated rigid lid and flexible thin film technologies (Figure 2.10)

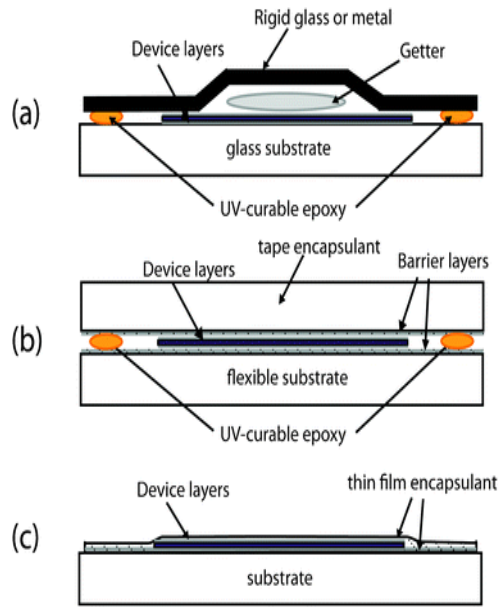


Figure 2.10: Conventional methods of encapsulation organic electronic devices (a) rigid lid (b) Coated lid and (c) thin film barrier layer.

Primarily, epoxy-glass seals [55] were employed to encapsulate organic electronic devices. Unfortunately, the UV-curable epoxy used in the upgraded manner of these routes is practically always trademarked and costly. Despite cost, these resins can be harmful to the device if they leach into or come in contact with the active organic layers in the course of processing, operation or storage. Moreover, the glass lids add substantial weight to the devices and thus eliminate the light-weight attraction of organic electronics.

Lately, a number of approaches have been proposed for the improvement of OLED lifetimes. Most of these methods use alternating inorganic, organic or inorganic-organic multi-layers [56-58]. Al-Li and HDPE multilayer barriers have been used to successfully encapsulate OLEDs on glass [56]. Lamination procedures have also been used to demonstrate reduced device sensitivity

to ambient conditions [57]. These encapsulation procedures, on the whole, have been proven to effectively control a bulk of extrinsic degradation mechanisms (dark spots, bubbles) that affect OLEDs due to oxygen and moisture in the operating environment [59].

An example of the above method can be seen in the work by Mandlik et al.[58], which has shown that plasma deposited SiO_xC_y hybrid layers can be used to extend the lifetimes of encapsulated OLEDs to about 7500 h. Although this method successfully improves the lifetimes of these devices, the essential vacuum deposition method is complex and not appropriate for low-cost applications. Furthermore the intrinsic defects from the growth mechanism, micro-size defects in vapor deposited films originating from particles on the substrate and geometrics shadowing by structural topography was reported to attribute to defect controlled permeation [60, 61].

The scanning electron microscope (SEM) image in Figure 2.11(a) shows a micro-sized defect caused by a particle. Similarly, the optical microscope image in Figure 2.11(b) shows the evolution of defect size with initially a 1 μm diameter after 120 min of atomic oxygen (AO) exposure [61].

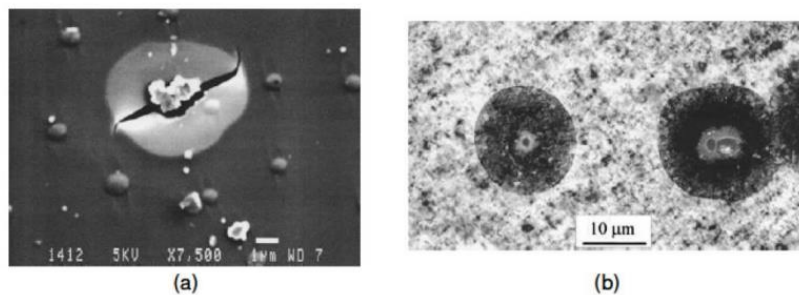


Figure 2.11: Effects of micron size particles on the encapsulation of electronic devices (a) contaminating particle at initial stage (b) evolution of contaminants after 120 min oxygen exposure [63]

In order to improve the appeal of organic electronics as low-cost, lightweight devices appropriate for flexible applications, more manageable and conformable encapsulation schemes must be developed. To this end, a number of simple encapsulation schemes have been developed that meet these criteria [64-66]. These techniques involve the use of solution processed polymer barriers such as Cytop [64, 65] or commercial non-proprietary laboratory processes [66] to realize satisfactory device stability. In particular, these techniques allow greater device stability in oxygen and moisture rich environments, while attaining the criteria necessary for flexible, light-weight and low cost applications. The use of polymer encapsulating layers also presents the prospect for added functionality. This subtle, yet potent advantage of polymer barrier layers has already been recently utilized in tuning the threshold voltage of organic field effect transistors [67].

It has been reported that the electroluminescence spectrum (EL) of polymer-encapsulated OLEDs showed a red-shift of the emitted photons [68]. This may be due to increased mobility of the polymer chains at temperatures higher than the glass transition temperature, T_g , which in turn results in an increased in packing of the polymer films [69]. Post deposition annealing of polymer light emitting diodes also has been reported to show a blue-shift in the EL spectrum [68]. The mechanisms responsible for this wavelength shifts still remain unclear and are a subject for research.

2.5 Transition metal oxides for organic electronics

Transition metal oxides (TMOs) like molybdenum trioxide (MoO_3), vanadium pentoxide (V_2O_5) or tungsten trioxide (WO_3) showcase remarkable electronic properties for charge injection and extraction in organic electronic devices. Tokito et al. in 1996 reported a considerable boost in hole injection when molybdenum, vanadium and ruthenium thin film

oxides were interposed between the organic active layer and anode of OLEDs [70]. TMOs have used these compounds in OLEDs and OPVs as hole injection and hole extraction interlayers and in charge generation and charge recombination layers [71-72]. These TMOs are very transparent and have high work functions making them appropriate for semiconductor electronics.

Highly efficient OLEDs have been reported with the use of MoO₃-doped 4, 4'-Bis(carbazol-9-yl)-biphenyl(CBP) as hole transport material (HTM) [73]. The MoO₃-doped HTM exhibited higher conductivity and thermal stability than the undoped counterpart.

Meyer et al. [74] have studied the energetics and electronic structures of TMOs and the key role they play as functional constituents in organic electronics. Figure 2.12 shows the energy diagram of MoO₃, V₂O₅ and WO₃ with their ionization energies, IE, electron affinities, EA and work functions, WF indicated. The measurements were carried out using ultraviolet photoemission spectroscopy (UPS) and inverse photoemission spectroscopy (IPES) for TMO films deposited by ultra-high vacuum thermal evaporation.

Solution-processing through spin-coating have also been shown by Meyer et al. [75] to produce high integrity TMO films. Figure 2.13 shows the atomic force microscopy image of the MoO₃ film obtained by spin-coating.

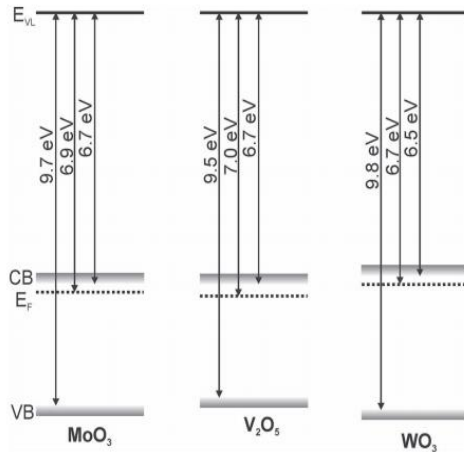


Figure 2.12: CB minimum and VB maximum with respect to the vacuum level (EVL) for MoO_3 , V_2O_5 and WO_3 , deduced from UPS and IPES measurements. The ionization energies, work functions and electron affinities are indicated.

Zilberberg et al. also reported TMO films deposited by solution processing with better properties relative to their vacuum deposited counterparts [76].

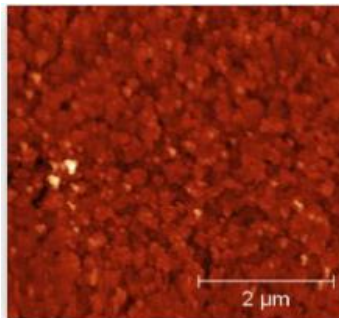


Figure 2.13: AFM image of MoO_3 nanoparticles deposited by spin-coating.

Kahn and co-workers [74] have explored the use of transition metal oxides like MoO_3 , V_2O_5 or WO_3 as buffer layers for semi-transparent devices and organic photovoltaic cells with improved charge extraction, enhanced power conversion efficiency and significantly improved long term stability. The effect of adhesion at the contacts on the performance of such systems remains underexplored. There is, therefore, the need to explore the effects of adhesion and contacts on OLED performance.

References

- [1] V. H. H. Hertz, "Ueber die Berührung fester elastischer Körper," *Journal für die reine und angewandte Mathematik (Crelle's Journal)*, 92,156 (1882).
- [2] K. L. Johnson, K. Kendall, and A. D. Roberts, "Surface energy and the contact of elastic solids," *Proceedings of the Royal Society A: Mathematical, Physical and Engineering Sciences*, 324, 301 (1971).
- [3] B. Derjaguin, "Effect of contact deformations on the adhesion of particles," *J. Colloid Interface Sci.*, 53,314 (1975).
- [4] D. Maugis, "Adhesion of spheres: The JKR-DMT transition using a Dugdale model," *J. Colloid Interface Sci.*, 150, 243 (1992).
- [5] R. Carpick, D. Ogletree, and M. Salmeron, "A general equation for fitting contact area and friction vs load measurements," *J. Colloid Interface Sci.*, 211,395, (1999).
- [6] M. A. Lantz, S. J. O'Shea, M. E. Welland, and K. L. Johnson, "Atomic-force-microscope study of contact area and friction on NbSe₂," *Phys. Rev. B*, 55, 10776,(1997).
- [7] O. Piétrement and M. Troyon, "General equations describing elastic indentation depth and normal contact stiffness versus load," *J. Colloid Interface Sci.*, 226,166 (2000).
- [8] W. Soboyejo, *Mechanical Properties of Engineered Materials*. New York: CRC, 2003.
- [9] S. Suresh, *Fatigue of Materials*, 2nd ed. Cambridge and New York: Cambridge University Press, 1998.
- [10] J. R. Rice and G. F. Rosengren, "Plane strain deformation near a crack tip in a power-law hardening material," *J. Mech.Phys Solids*, 16,1 (1968).
- [11] H. Corten, Ed., *STP 514 Fracture Toughness: Part II*. West Conshohocken, PA: ASTM International, 1972.
- [12] W. Brown and J. Kaufman, Eds., *STP 632 Developments in Fracture Mechanics Test Methods Standardization*. West Conshohocken, PA: ASTM International, 1977.

- [13] J. R. Rice, "A path independent integral and the approximate analysis of strain concentration by notches and cracks," *J. Appl. Mech.*, 35, 379 (1968).
- [14] J. W. Hutchinson, "Fundamentals of the phenomenological theory of nonlinear fracture mechanics," *J. Appl. Mech.*, 50, 1042 (1983).
- [15] J. Dundurs, "Discussion: Edge-bonded dissimilar orthogonal elastic wedges under normal and shear loading," *J. Appl. Mech.*, 36, 650 (1969).
- [16] A. H. England, "A crack between dissimilar media," *J. Appl. Mech.*, 32, 400, (1965).
- [17] F. Erdogan, "Stress distribution in bonded dissimilar materials with cracks," *J. Appl. Mech.*, 32, 403 (1965).
- [18] J. R. Rice and G. C. Sih, "Plane problems of cracks in dissimilar media," *J. Appl. Mech.*, 32, 418 (1965).
- [19] B. M. Malyshev and R. L. Salganik, "The strength of adhesive joints using the theory of cracks," *Int. J. Fract.*, 26, 261 (1984).
- [20] J. W. Hutchinson and Z. Suo, "Mixed mode cracking in layered materials," *Adv. Appl. Mech.*, 29, 63 (1992).
- [21] W. O. Soboyejo, G.-Y. Lu, S. Chengalva, J. Zhang, and V. Kenner, "A modified mixed-mode bending specimen for the interfacial fracture testing of dissimilar materials," *Fatigue Fract. Eng. Mater. Struct.*, 22, 799 (1999).
- [22] H. C. Cao and A. G. Evans, "An experimental study of the fracture resistance of bimaterial interfaces," *Mech. Mater.*, 7, 295 (1989).
- [23] A. G. Evans and B. J. Dalgleish, "The fracture resistance of metal-ceramic interfaces," *Acta Metall. Mater.*, 40, 295 (1992).
- [24] M. Pope, H. P. Kallmann, and P. Magnante, "Electroluminescence in Organic Crystals," *J. Chem. Phys.*, 38, 2042 (1963).
- [25] C. W. Tang and S. a. VanSlyke, "Organic electroluminescent diodes," *Appl. Phys. Lett.*, 51, 913 (1987).

- [26] J. M. Shaw and P. F. Seidler, "Organic electronics: Introduction," *IBM J. Res. Dev.*, 45,3 (2001).
- [27] Y. Xia, J. a. Rogers, K. E. Paul, and G. M. Whitesides, "Unconventional methods for fabricating and patterning nanostructures," *Chem. Rev.*, 99, 1823 (1999).
- [28] Y. Xia and G. M. Whitesides, "Soft lithography," *Angewandte Chem. Int.Ed.*, 37,550 (1998).
- [29] Y. Xia and G. M. Whitesides, "Soft lithography," *Annual Rev. Mater. Sci.*, 28,153 (1998).
- [30] C. Kim, P. E. Burrows, and S. R. Forrest, "Micropatterning of organic electronic devices by cold-welding," *Sci.*, 288,831 (2000).
- [31] C. Kim, M. Shtein, and S. R. Forrest, "Nanolithography based on patterned metal transfer and its application to organic electronic devices," *Appl. Phys. Lett.*, 80, 4051 (2002).
- [32] C. Kim and S. Forrest, "Fabrication of organic light-emitting devices by low-pressure cold welding," *Adv. Mater.*, 15,541 (2003).
- [33] X. Xu, M. Davanco, X. Qi, and S. R. Forrest, "Direct transfer patterning on three dimensionally deformed surfaces at micrometer resolutions and its application to hemispherical focal plane detector arrays," *Org. Electron.*, 9,1122 (2008).
- [34] J. Rhee and H. H. Lee, "Patterning organic light-emitting diodes by cathode transfer," *Appl. Phys. Lett.*, 81, 4165 (2002).
- [35] C. Kim, Y. Cao, W. O. Soboyejo, and S. R. Forrest, "Fabrication of organic light-emitting devices by direct transfer of active organic materials using organic-organic adhesion," in *The 17th Annual Meeting of the IEEE Lasers and Electro-Optics Society*, 2004. LEOS 2004, 2004,1, 336 (2004).
- [36] C. W. Joo, S. O. Jeon, K. S. Yook, and J. Y. Lee, "Improved device performances in polymer light-emitting diodes using a stamp transfer printing process," *Org. Electron.*, 10, 372 (2009).
- [37] T.-W. Lee, J. Zaumseil, Z. Bao, J. W. P. Hsu, and J. A. Rogers, "Organic light-emitting diodes formed by soft contact lamination," *Proceedings of the National Academy of Sciences of the United States of America*, 101, 429 (2004).
- [38] J. Ouyang and Y. Yang, "Conducting polymer as transparent electric glue," *Adv. Mater.*, 8,2141 (2006).

- [39] T. Zyung, S. H. Kim, H. Y. Chu, J. H. Lee, S. C. Lim, J.-I. Lee, and J. Oh, "Flexible organic LED and organic thin-film transistor," *Proc. IEEE*, 93, 1265 (2005).
- [40] Chabinyc Michael L, Salleo Alberto, Wu Yiliang, Liu Ping, Ong Beng S, Heeney Martin, McCulloch Iain, "Lamination method for the study of interfaces in polymeric thin film transistors" *J. Am. Chem. Soc.*, 126, 13928 (2004)
- [41] Masato Ofuji, Andrew J. Lovinger,, Christian Kloc,, Theo Siegrist,, Ashok J. Maliakal, and, Howard E. Katz "Organic Semiconductor Designed for Lamination Transfer between Polymer Films" *Chem. Mater.* 17, 5748 (2005).
- [42] Hongyu Liu and Runguang Sun, Laminated active matrix organic light-emitting devices *Appl. Phys. Lett.* 92, 063304 (2008)
- [43] G. H. Kim, J. Oh, Y. S. Yang, L.-M. Do, and K. S. Suh, "Lamination process encapsulation for longevity of plastic-based organic light-emitting devices," *Thin Solid Films*, 467, 1 (2004).
- [44] J. H. Kim, S.-min Seo, and H. H. Lee, "Nanovoid nature and compression effects in organic light emitting diode," *Appl. Phys. Lett.*, 90, 143521 (2007).
- [45] Y.-R. Jeng, M.-L. Guo, H.-C. Li, and T.-F. Guo, "Interfacial morphology in polymer light-emitting diodes," *Electrochem. Solid-State Lett.*, 139 (2007).
- [46] Y. Cao, C. Kim, S. R. Forrest, and W. Soboyejo, "Effects of dust particles and layer properties on organic electronic devices fabricated by stamping," *J. Appl. Phys.*, 98, 033713 (2005).
- [47] Y. Cao, N. Yao, K. McIlwrath, J. Zhou, G. Osinkolu, and W. O. Soboyejo, "An investigation of Au-Ag interface formed by cold welding using focused ion beam/transmission electron microscopy," *MRS Proc.*, 965,1, (2011).
- [48] W. O. Akande, Y. Cao, N. Yao, and W. Soboyejo, "Adhesion and the cold welding of gold-silver thin films," *J. Appl. Phys.*, 107, 043519 (2010).
- [49] Z. Zong, Y. Cao, N. Rahbar, and W. Soboyejo, "Nano- and microscale adhesion energy measurement for Au-Au contacts in microswitch structures," *J. Appl. Phys.*, 100,104313 (2006).

- [50] T. Tong, B. Babatope, S. Admassie, J.Meng, O. Akwogu, W. Akande, and W. O. Soboyejo, "Adhesion in organic electronic structures," *J. Appl. Phys.*, 106, 083708 (2009).
- [51] Roge'rio Toniolo, Ivo A. Hu'mmelgen "Simple and Fast Organic Device Encapsulation Using Polyisobutene" *Macromol. Mater. Eng.* 289, 311 (2004).
- [52] Zhang Y, Andreasson M, Zhou H, Liu J, Andersson T Fan J-Y "Encapsulation of OLED device by Using Anisotropic Conductive Adhesive" *Proc. 9th IEEE CPMT Symposium on High Density Packaging and Microsystems Integration* (2007)
- [53] A. P. Ghosh, L. J. Gerenser, C. M. Jarman, and J. E. Fornalik, "Thin-film encapsulation of organic light-emitting devices", *Appl. Phys. Lett.* 86, 223503 (2005).
- [54] Han J-M, Han J-W, Chun J-Y, Ok C H, and Seo D-S, "Novel Encapsulation Method for Flexible Organic Light-Emitting Diodes using Poly(dimethylsiloxane)",*Jpn. J. Appl. Phys.* 47 8986 (2008).
- [55] Burrows P.E., Bulović V., Forrest S. R., Sapochak L S, McCarty D M, and Thompson M E "Reliability and Degradation of Organic Light Emitting Devices," *Appl. Phys. Lett.* 652922 (1994).
- [56] Seung Ho Kwon, Sang Yoon Paik, Oh Jun Kwon, and Jae Soo Yoo, "Triple-layer passivation for longevity of polymer light-emitting diodes",*Appl. Phys. Lett.* 79, 4450 (2001)
- [57] Gi Heon Kim, Jiyoung Oh, Yong Suk Yang, Lee-Mi Do, Kyung Soo Suh, "Lamination process encapsulation for longevity of plastic-based organic light-emitting devices,"*Thin Solid Films*, 467,1 (2004).
- [58] Prashant Mandlik, Jonathan Gartside, Lin Han, I-Chun Cheng, Sigurd Wagner, Jeff A. Silvernail, Rui-Qing Ma, Michael Hack, and Julie J. Brown, "A single-layer permeation barrier for organic light-emitting displays", *Appl. Phys. Lett.* 92, 103309 (2008).
- [59] R.E Gill, P van de Weijer, C.T.H Liedenbaum, H.F.M Schoo, A Berntsen, J.J.M Vleggaar, R.J Visser, "Stability and characterization of large area polymer light-emitting diodes over extended periods," *Opt. Mater.*, 12, 183 (1999)
- [60] A.S. da Silva Sobrinho, G. Czeremuskin, M. Latreche, and M. R. Wertheimer, "Defect permeation correlation for ultrathin transparent barrier coatings on polymers," *J. Vac. Sci. Technol. A*, 18,

149 (2000)

- [61] A. S. da Silva Sobrinho, M. Latreche, G. Czeremuszkin, J. E. Klemberg-Sapieha, and M.R. Wertheimer, "Transparent barrier coatings on polyethylene terephthalate by single- and dual frequency plasma enhanced chemical vapor deposition," *J. Vac. Sci. Technol. A*, 16, 3190 (1998).
- [62] A. S. da Silva Sobrinho, G. Czeremuszkin, M. Latreche, G. Dennler, M. R. Wertheimer, "A study of defects in ultra-thin transparent coatings on polymers", *Surf. Coat. Technol.*, 116, 1204 (1999).
- [63] Namsu Kim, "Fabrication and Characterization of thin-film encapsulation for Organic Electronics". Atlanta, Ga: Georgia Institute of Technology, Ph.D Thesis, 2009
- [64] J. Granstrom, J. S. Swensen, J. S. Moon, G. Rowell, J. Yuen, and A. J. Heeger, "Encapsulation of organic light-emitting devices using a perfluorinated polymer" *Appl. Phys. Lett.* 93, 193304 (2008).
- [65] Jimmy Granstrom, Michael Villet, Tirtha Chatterjee, Jeffrey A. Gerbec, Evan Jerkunica, and Anshuman Roy, "Multilayer barrier films comprising nitrogen spacers between free-standing barrier layers," *Appl. Phys. Lett.* 95, 093306 (2009).
- [66] M. E. Bahlke, S. P. Subbarao, I. Kymissis, "A Laboratory Process for Encapsulation of Air Sensitive Organic Devices," *IEEE Transactions on Electron Devices*, 57, 153, (2010).
- [67] M. Scharnberg, V. Zaporozhchenko, R. Adelung, F. Faupel, C. Pannemann, T. Diekmann, and U. Hilleringmann, "Tuning the threshold voltage of organic field-effect transistors by an electret encapsulating layer" *Appl. Phys. Lett.* 90, 013501 (2007)
- [68] T.W. Lee and O.O. Park, "The effect of different heat treatments on the luminescence efficiency of polymer light emitting diodes", *Adv. Mater.*, 12, 801 (2000).
- [69] J. Liu, T. F. Guo, and Y. Yang, "Effect of Thermal Annealing on the Performance of Polymer Light Emitting Devices", *J. Appl. Phys.* 91, 1595 (2002).
- [70] S. Tokito, K. Noda and Y. Taga, "Metal oxides as a hole-injecting layer for an organic electroluminescent device", *J. Phys. D. : Appl. Phys.* 29, 2750 (1996)
- [71] K. J. Reynolds, J. A. Barker, N.C. Greenham, R. H. Friend and G. L. Frey, "Inorganic solution-processed hole-injecting and electron-blocking layers in polymer light-emitting diodes", *J. Appl.*

- Phys. 92, 7556 (2002).
- [72] A. G. F. Janssen, T. Riedl, S. Hamwi, H. H. Johannes and W. Kowalky, “Highly efficient organic tandem solar cells using an improved connecting architecture”, Appl. Phys. Lett. 91,073519 (2007).
- [73] J. Meyer, A. Shu, M. Kroger and A. Kahn, “ Effect of contamination on the electronic structure and hole-injection properties of MoO₃/organic semiconductor interfaces”, Appl. Phys. Lett. 96, 133308 (2010).
- [74] J. Meyer, S. Hamwi, M. Kroger , W. Kowalsky, T. Riedl and A. Kahn, “ Transition Metal Oxides for Organic Electronics: Energetics , Device Physics and Applications”, Adv. Mater. 24, 5408(2012)
- [75] J. Meyer, R. Khalandovsky, P. Gorn and A. Kahn, “MoO₃ Films for Efficient Hole-injection in Organic Electronics”, Adv. Mater. 23, 70 (2011).
- [76] K. Zilberberg, J. Meyer and T. Riedl, “Solution processed metal-oxides for organic electronic devices”, J. Mater. Chem. C, 1, 4796 (2013).

Chapter 3

Pressure Effects on the Performance of Organic Light Emitting Devices

3.1 Introduction

Organic light emitting diodes (OLEDs) are layered structures that usually consist of successive organic layers that are stacked between a metallic cathode and an inorganic anode [1] (Figure 3.1). The diode is usually built on a transparent substrate (such as glass) that eventually forms the display through which the emitted light is observed. On top of this substrate, there is a layer of highly conductive and transparent indium tin oxide (ITO), which forms the anode of the diode. On top of the ITO anode, there is a thin layer of material that is used to facilitate hole-injection from the anode into the active layer. Poly(3, 4-ethylene dioxythiophene) doped with poly(styrene sulphonate) (PEDOT:PSS) is extensively used as a hole-injection layer (HIL) material. Next, the emissive layer of the OLED is deposited. To complete the diodes, conventional shadow masks are used to deposit a patterned aluminum layer to form the cathode.

However, the widely used hole-injection layer material, PEDOT:PSS, is not chemically stable [2]. The chemical reaction at the interfaces between PEDOT:PSS and other layers can give rise to degradation of the device [2]. Also, its relatively limited work function hinders charge injection into organic materials with large ionization energy [3]. This has motivated recent

interest in transition metal oxides (TMOs), such as molybdenum trioxide (MoO_3), tungsten trioxide (WO_3), nickel oxide (NiO), or vanadium pentoxide (V_2O_5), that have been shown to have the potential to effectively replace PEDOT:PSS in OLEDs [4-6], organic photovoltaic (OPV) cells[2,7], and organic thin film transistors (OTFT)[8]. As novel HIL materials, TMOs can minimize charge injection barriers at organic semiconductor interfaces [9]. Hence, TMOs can lower operating voltages, while improving device efficiency. Furthermore, they have excellent optical transparency in the visible range, moderate conductivity and low thermal evaporation temperature [9].

A number of researchers [10-16] have explored the effects of pressure on the fabrication and performance of organic electronic devices. Kim et al. [10] observed that OLEDs fabricated after pressure treatment exhibited a notable increase in luminance intensity and current efficiency, when compared with pressure-free diodes. It was later confirmed by Fina et al. [11]. The current density, photoluminescence, electroluminescence improvement when the pressure is applied on the OLEDs was reported by other researchers [12]. Kim and Forrest [13] found that the pressures required to fabricate OLEDs could be 1000 times smaller when using flexible polydimethylsiloxane (PDMS) than rigid Si stamps in the cold welding processes. Cao et al.[14] have used finite element simulation to show that, in the cold welding processes, soft stamps are expected to deform easily around dust particles at relatively low pressures. However, considerably higher pressures are needed to deform stiff stamps over similar contact areas. In the case of lamination processes, the evolution of the contact profiles around dust particles has also been studied in prior work by Du et al.[15] in which numerical simulations were used to study the effects of pressure.

In this work, OLEDs are fabricated with the novel hole-injection layer material, MoO₃. For comparison, they are also fabricated with a more conventional hole-injection layer material, PEDOT:PSS. Subsequently, the effects of pressure are studied by applying pressure to fabricated OLED structures with MoO₃ or PEDOT:PSS hole-injection layers. The current-voltage characteristics of both the MoO₃-based and PEDOT:PSS-based OLED structures are shown to be significantly improved by pressure treatment. In an effort to understand the underlying causes of the effects of pressure treatment, numerical finite element simulations are used to study the contacts between layers in the OLED structures. These utilize measurements of layer mechanical properties (Young's moduli and adhesion energies) that are obtained using nanoindentation and atomic force microscopy techniques. These are incorporated into finite element models that were used for the simulation of the pressure-assisted OLED fabrication process. The models explore the effects of applied pressure on OLED structures with dust particles interposed between the hole-injection and emissive layers. The results show that pressure effects (on the electrical properties of OLEDs) can be explained by the increase of contact area under pressure. The implications of the current results are then discussed for the fabrication of robust organic electronic devices.

3.2 Experiments

OLEDs with the conventional sandwich structure (Figure 1) were fabricated at room temperature (~ 25°C). The ITO-coated glass substrates (Delta technologies, Stillwater, MN) were cleaned by sonication in methanol, acetone and isopropyl alcohol (IPA) for 30 minutes. The substrates were further cleaned in an Ozone ultraviolet cleaner for 10 minutes (UVOCS, Lansdale, PA).

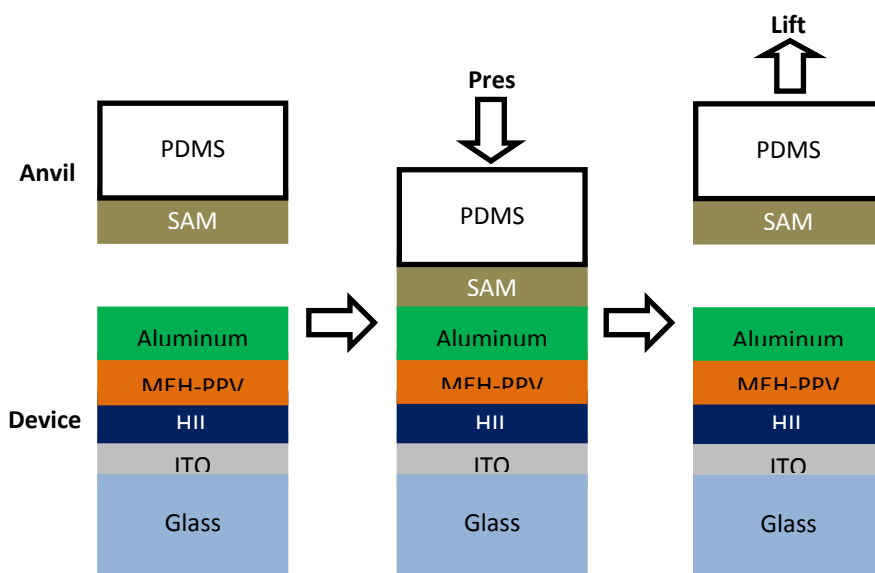


Figure 3.1: Schematic of the pressure treatment for the pressure-assisted OLED fabrication process. The device was made with the MoO_3 or PEDOT:PSS as the HIL material. The self-assembled monolayer (SAM) coated anvil was pressed onto the device to add a pressure and then lifted from the device to remove the pressure.

MoO_3 (Sigma-Aldrich, St. Louis, MO) was deposited onto the cleaned ITO anode by thermal evaporation using an Edwards E306A thermal evaporator deposition system (Edwards, Sussex, UK). For comparison, another group of samples were fabricated with PEDOT:PSS, instead of MoO_3 . Baytron P VP Al-4083 PEDOT:PSS (Heraeus Clevios, Hanau, Germany) was filtered through a $0.2 \mu\text{m}$ filter for 1 minute at a rate of 3000 revolutions per minute (rpm) to further improve the smoothness and uniformity. The filtered solution was then spin-coated onto the cleaned ITO anode at 1500 rpm for 15 s. The samples were then cured at 120°C for 5 minutes to remove any residual moisture.

Poly[2-methoxy-5-(2'-ethyl-hexyloxy)-1,4-phenylene vinylene] (MEH:PPV) (Aldrich, St. Louis, MO), with molecular weight between 150,000 and 250,000, was used to form the emissive layer. It was dissolved in chloroform to produce a 5 mg/ml solution. After stirring the resulting solution

for 6 hours, it was filtered and then spin-coated onto the hole-injection layer at 800 rpm for 60 s. The aluminum cathode was thermally deposited onto the emissive layer using an Edwards E306A thermal evaporator (Edwards, Sussex, UK) operated at a vacuum of 10^{-7} Torr. The device area of 3 mm^2 was defined using conventional shadow masks. The resulting OLED structure has a pattern of cylinder array with a radius of $\sim 0.98 \text{ mm}$ for each cylinder and a distance of $\sim 4 \text{ mm}$ between the centers of adjacent cylinders.

Polydimethylsiloxane (PDMS) was used to prepare the anvil. The PDMS mixture (Sylgard 184, Dow Corning) was prepared by mixing a pre-polymer base with a curing agent. This was done in a 10:1 ratio (by weight) in a petri dish. The resulting mixture was then cured in a vacuum oven at $80 \text{ }^\circ\text{C}$ for 2 hrs. The cured PDMS anvil was then removed from the petri dish. On top of the PDMS anvil, a layer of (tridecafluoro-1,1,2,2,-tetrahydrooctyl)-trichlorosilane (FOTCS) (Gelelest Inc., Morrisville, PA) was deposited as a self-assembled monolayer (SAM) that reduces the adhesion between the anvil and the device. The SAM was deposited by vapor deposition. This was done in a desiccator at room temperature for 6 hrs.

The coated PDMS anvil was then brought into contact with the device using an Instron mechanical tester (Instron, Norwood, MA). This was used to apply a pressure between 5.6 MPa and 8.3 MPa to the fabricated OLEDs for 10 minutes at room temperature. Subsequently, the pressure was then removed from the OLEDs by lifting up the anvil. It is important to note here that the SAM reduces the adhesion between the anvil and the device. This ensures that the anvil and the OLEDs are separated during the lifting stages. Electrical characterization of the OLEDs was carried out before and after pressure treatment. This was done using a Keithley 2400 broad purpose source meter (Keithley Instruments, Inc., Cleveland, Ohio).

3.3 Characterization of layers and device

3.3.1 Nanoindentation

Since the mechanical properties of the MoO₃ layer have not been well characterized in the literature, nanoindentation experiments were used to measure the Young's modulus of MoO₃. Firstly, the MoO₃ (Sigma-Aldrich, St. Louis, MO) was deposited onto the surface of glass slides by thermal evaporation using an Edwards E306A thermal evaporator deposition system (Edwards, Sussex, UK). The resulting MoO₃ thin films had thicknesses of around 50 nm, as measured using a KLA-Tencor P15 Surface Profiler (KLA-Tencor, Milpitas, CA).

Nanoindentation measurements were then carried out on the MoO₃ thin films. The experiments were performed with a TriboScope nanomechanical testing system (Hysitron Inc., Minneapolis, MN), coupled to a Dimension 3100 scanning probe microscope (Veeco Instruments Inc., Woodbury, NY). A Berkovich indenter tip, a three sided pyramidal-type tip, with an included angle of 142.3°, was used. This was chosen for its large angle, hence large contact area, with the samples. The loading profile consisted of the following three steps: loading to a peak load in 2 s, holding at the peak load for 2 s, and returning to zero load in 2 s. A peak load ranging from 60 μN to 200 μN was applied. To minimize the possible interactions between adjacent indents, all the indents were separated by at least 20 μm. Images of the surfaces (before and after the indentation) were obtained using a contact-based scanning probe technique.

The indentation depths were generally much greater than the surface roughness levels. Commonly, for metallic materials, indentation depths should be at least 20 times greater than the average surface roughness to minimize the possible effects of rough surfaces [16]. Also, the, indentation depths should be less than 10% of the film thickness to minimize substrate effects

[17], especially for those films harder than the substrate. In this study, a range of peak loads was selected, which generated a range of contact depths during the indentation experiments, to study the possible effects of indentation depth. Finally, the peak loads were maintained for sufficient durations to minimize the possible effects of viscoelasticity on the measured Young's moduli.

3.3.2 Atomic Force Microscopy Measurements

AFM adhesion measurements were used to study the adhesion between the hole-injection layer and the emissive layer, i.e. between MoO₃ and MEH-PPV. As a more conventional hole-injection layer material, PEDOT:PSS was studied for comparison. The adhesion between PEDOT:PSS and MEH-PPV was also measured.

The filtered PEDOT:PSS solution described above was spin-coated onto glass slides and then cured. The filtered MEH-PPV solution described above was also spin-coated onto other glass. Using a Dimension 3000 AFM (Digital Instruments, Plainview, NY) under tapping mode, the root mean square surface roughness of each film was measured from the surface profile.

Etched silicon contact AFM tips (Veeco Instruments, Woodbury, NY) were coated with MoO₃ (Sigma-Aldrich, St. Louis, MO) using the same thermal evaporator described earlier. The AFM tips were also coated with filtered MEH-PPV solution described above using a dip-coating technique developed in prior studies by Wolf et al. [18]. After coating, scanning electron microscopy (SEM) images were obtained in a FEI XL30 FEG-SEM (Philips, Hillsboro, OR). These were used to validate the coating and measure the AFM tip radii from the tip profile.

Contact AFM experiments were performed using the MoO₃ coated tips and the MEH-PPV substrates. They were also performed using the MEH-PPV coated tips and PEDOT:PSS

substrates. The experiments were performed in air, over a temperature range of 22–25 °C and relative humidity range of 31%–46%. At least six force curves were collected for each interaction using the same Dimension 3000 AFM described earlier. This was used to measure the deflection of the AFM tips as they were pulled off from the substrate. The spring constant of each tip was measured using the thermal tune method [19] with a Nanoscope IIIa AFM (Digital Instruments, Plainview, NY). By substituting the spring constant and the measured deflections into Hooke's Law, the adhesion forces were estimated for the interfaces between the coated tips and the substrates.

3.3.3 Optical Measurements

The optical transmittance of each individual layer that makes up the complete organic light emitting device that was fabricated in this study was measured using a UV/Vis AvaSpec 128 Fiber-Optic Spectrophotometer (Avantes BV, USA). Organic layers are known to emit light when voltage is applied across electrodes that sandwich them. We therefore seek highly transparent layers that can facilitate the exit of the emitted light. For the transmission spectra study, thin films of different substances were deposited on glass and ITO-coated glass. The optical properties were then studied using a UV/Vis Spectrophotometer consisting of a light source and detector, all connected by optical fiber.

3.4 Analytical and Numerical Modeling

3.4.1 Adhesion Models and Adhesion Energy

There are several existing models describing the adhesion interaction between two spheres. To select the appropriate model, Maugis [20] defined a transition parameter, λ , which is given

by:

$$\lambda = 2\sigma_0 \left(\frac{R}{\pi\kappa^2\gamma} \right)^{1/3} \quad (1)$$

where γ is the adhesion energy per unit area; R is the combined radius given by $R = R_1R_2 / (R_1 + R_2)$, where R_1 and R_2 are the radii of the two spheres, respectively; κ is the combined elastic modulus for two spheres in contact, which is given by $\kappa = 4/3[(1-\nu_1)^2/E_1 + (1-\nu_2)^2/E_2]^{-1}$, where E_1 and E_2 are the elastic moduli of the two spheres, and ν_1 and ν_2 are the Poisson's ratios of the two spheres, respectively. By choosing σ_0 to match the minimum adhesive stress of a Lennard-Jones potential with equilibrium separation distance z_0 , it follows that $\delta_0 = 0.97z_0$. The Johnson-Kendall-Roberts (JKR) model [21] applies when $\lambda > 5$. The Derjaguin-Muller-Toporov (DMT) model [22] applies when $\lambda < 0.1$. The Maugis-Dugdale (MD) model [20] applies for the intermediate values of λ .

For the two extreme cases, the adhesion energy is given in JKR and DMT theories by:

$$\gamma_{JKR} = \frac{2F_{ad}}{3\pi R} \quad (2)$$

$$\gamma_{DMT} = \frac{F_{ad}}{2\pi R} \quad (3)$$

where F_{ad} can be the adhesion force measured by the AFM adhesion experiments.

For MD model, the calculation was simplified using an iterative process, introduced by Carpick et al. [23] and further developed by Piétrement and Troyon [24]. Another dimensionless

parameter α was defined and calculated through curve fitting to be

$$\lambda = -0.913 \ln(1 - 1.018\alpha) \quad (4)$$

A dimensionless adhesion force was defined by

$$\hat{F}_{ad} = \frac{F_{ad}}{\pi\gamma R} \quad (5)$$

They also determined empirical equations supplying direct conversion equations between parameter α and \hat{F}_{ad} by:

$$\hat{F}_{ad} = 0.267\alpha^2 - 0.767\alpha + 2.000 \quad (6)$$

The AFM force measurement measures F_{ad} . With R and κ known, the adhesion energy can be calculated by solving the Equations (1), (4), (5) and (6).

3.4.2 Analytical Models for Pressure-Free Contact

Dust particles in the clean room environment include silicon, iron, aluminum, quartz, textile polymer, silicone and photoresist [14]. The typical dust particle diameter ranges from ~ 0.1 to $20 \mu\text{m}$ [25-26]. During the fabrication of organic electronic devices, the dust particles are interposed between the layers in the devices. They, therefore, affect the evolution of contact areas between adjacent layers. It is important to note here, that prior work [27] has used transmission electron microscopy and electron energy loss spectroscopy to reveal dust particles and interfacial gaps between both cold-welded interfaces and the electron-beam evaporated interfaces.

Several analytical models are relevant to the study of contact profile of the initial interfaces around the dust particles before pressure treatment. Considering the model of a membrane suspended on top of a particle, a blister forms under the suspended beam, with a radius, a . Malyshev and Salganik [28] solved for the problem of the classical penny crack under plate bending. According to them, the relationship between the adhesion energy and the contact profile can be represented by

$$\gamma = \frac{2Et^3h^2}{3(1-\nu^2)a^4} \quad (7)$$

where E and ν are the Young's modulus and Poisson's ratio of the membrane material, respectively; t is the thickness of the membrane; h is the height of the blister under the beam, which again equals to the diameter of the interposed particle.

If the thickness of the suspended membrane is much smaller compared with the height and the radius of the blister, instead of membrane bending, the stretching of the membrane dominates the mechanical energy restored in the membrane, according to the study by Wan and Mai [29]. Thus, the adhesion energy between the membrane and the substrate could be calculated by

$$\gamma = \frac{Eth^4}{16a^4} \quad (8)$$

This model has been used to describe the contact profile between a graphene sheet and a silicon substrate with silver particles trapped in the middle [30].

3.4.3 Finite Element Analysis

Cao et al. [14] have shown the evolution of contact areas between layers of materials during the cold welding processes. The evolution of the contact area during the lamination process has also

been studied in our previous work [15]. This work examines the effects of pressures on the evaporated and spin-coated organic light emitting diodes. Finite element simulations of the pressure treatment processes were conducted using the ABAQUS software package (Dassault Systèmes Simulia Corporation, Providence, RI). The effects of dust particles were considered in the simulations of contact between hole-injection layer (MoO_3 or PEDOT:PSS) and the emissive layer (MEH-PPV).

The simulation considered part of the device in the vicinity of a dust particle. Axisymmetric geometries were used to simplify the cylindrical geometry of the structure. The simulated part of the structure has a radius of 200 μm . Also, the thicknesses of the simulated portions of the PDMS stamp and the glass substrate were all 200 μm . It was assumed that the other part of the device, which is further away from the dust particle, has a negligible effect on the mechanics around the dust particle.

A typical finite element model is presented in Figure 3.2. It shows a PDMS stamp about to compress onto an evaporated device. Note that the material of each layer is marked in the figure. The hole-injection layer (HIL) material could be either MoO_3 or PEDOT:PSS. The layer thicknesses are 200 nm, 100 nm, 50 nm and 200 nm for aluminum, MEH-PPV, HIL and ITO, respectively. The diameter of dust particle was chosen to be 1 μm . The radius of the blister was calculated using the analytical models described earlier in this work.

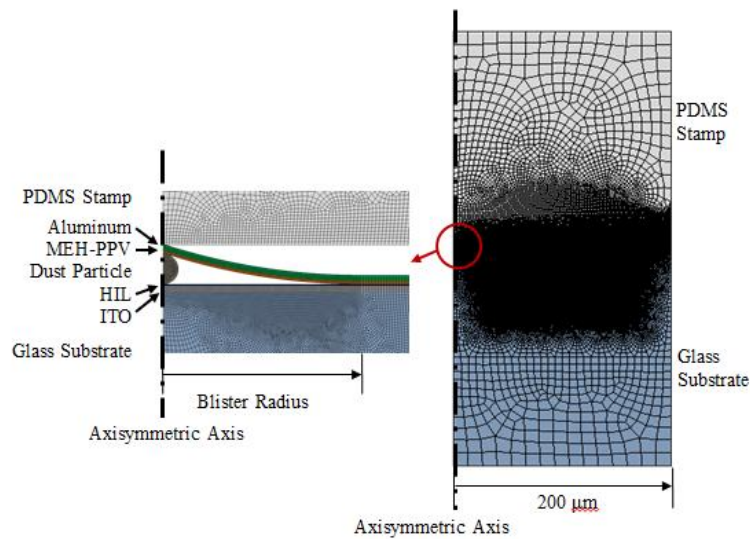


Figure 3.2: FEA Model for the pressure treatment in the pressure-assisted fabrication of OLEDs. The HIL material could be either MoO₃ or PEDOT:PSS.

A 4-node bilinear axisymmetric quadrilateral element was used in the mesh. The mesh was dense in the regions near the dust particle and the contact surfaces. Similar mesh sizes were also used in the regions near the surface contact regimes to enable convergence in contact simulation. It was assumed that all the materials exhibited isotropic elastic behavior. Young's moduli were obtained from the nanoindentation experiments described earlier in this work as well as from prior studies [14, 15, 31-34]. The Young's modulus and Poisson's ratio of each material used in the simulation are summarized in Table 3.1.

The axisymmetric boundary condition was applied at the symmetry axis (Figure 3.2). The bottom of the substrate was fixed to have no displacements and rotations. The outer edge of the model was fixed to have no lateral movement for continuity. The top of the stamp moved downward. A pressure was applied from the stamp onto the device. For simplicity and convergence, frictionless contact was assumed between contact surfaces.

Table 3.1: Material properties used in the finite element simulations

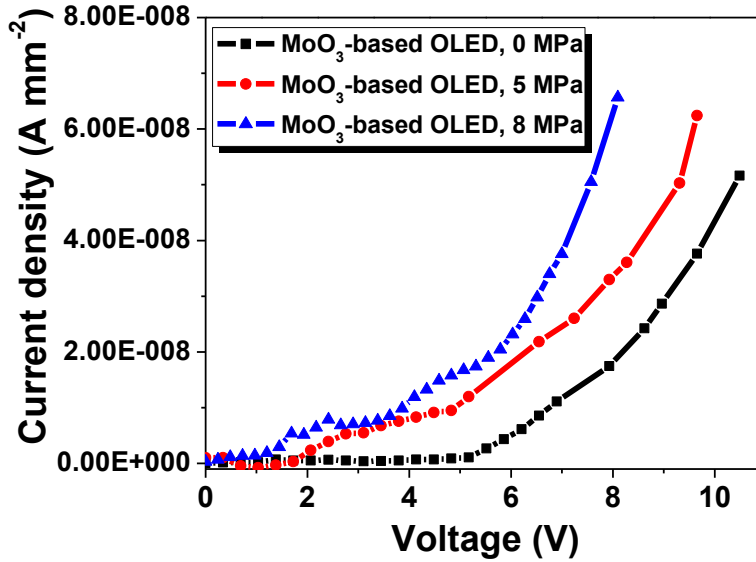
Material	Young's modulus (GPa)	Poisson's Ratio	Reference
PDMS	0.003	0.48	Refs. 31,32
Aluminum	70	0.3	Ref. 33
PEDOT:PSS	1.42	0.3	Ref. 15
MoO ₃	64.6	0.3	Current study
MEH-PPV	11.5	0.3	Ref. 15
ITO	116	0.35	Ref. 34
Glass	69	0.3	Ref. 33
Particle	70	0.3	Ref. 14

3.5 Results and Discussion

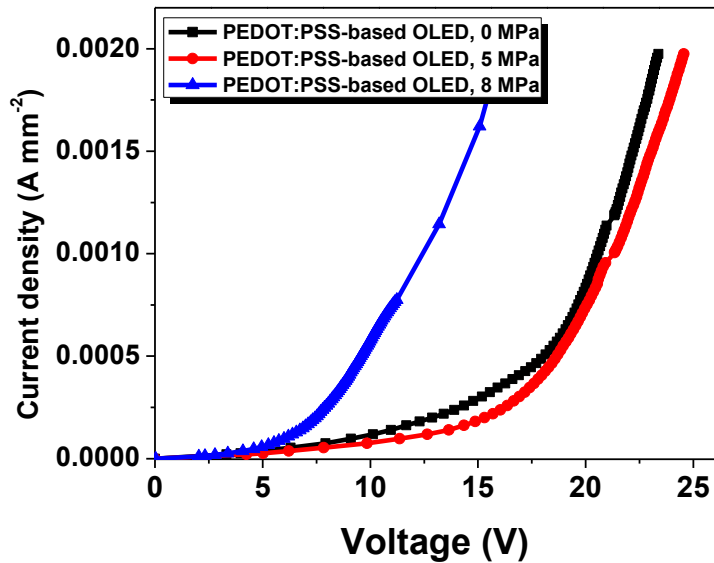
3.5.1 Electrical Characterization of OLEDs

The current-voltage characteristics obtained for the OLEDs (both before and after the pressure treatments) are presented in Figures 3.3(a) and 3.3(b), for the MoO₃-based and PEDOT:PSS-based devices, respectively. It is shown that the current density for a given voltage increases with applied pressure for both MoO₃-based and PEDOT:PSS-based devices. It is also shown that with the applied pressure, the threshold voltage decreases for the PEDOT:PSS-based devices from ~10 V to ~6 V. Before the pressure treatment, the threshold voltage for the devices fabricated with novel hole-injection layer material, MoO₃, ~5 V, is already lower than that of PEDOT:PSS,

~10V. After the pressure treatment, the threshold voltage for the MoO₃ based-devices further decreased further to ~3 V.



(a)



(b)

Figure 3.3: Current-voltage characteristic for (a) MoO₃-based devices and (b) PEDOT:PSS-based devices before and after pressure treatment.

3.5.2 Optical Transmittance Measurements

This section describes the Spectral properties of the different layers making up the OLED mainly considering the Transmittance T. When light travels through a thin film layer, it is absorbed, reflected or transmitted. Absorbance, Reflectance, and Transmittance are optical properties which can be analyzed from the spectrum produced during the process of light travel. A simple equation which relates these three properties is given by:

$$I = T + R + A \quad (9a)$$

in terms of percentage,

$$100 = T + R + A \quad (9b)$$

where T is a measure of the Transmittance, R is the Reflectance and A is the Absorbance. For a good OLED, we wish to increase the transmittance of the ITO layer and reduce the absorbance and reflectance. Figure 4 gives the results obtained for different layers using the UV/Vis spectrophotometer to analyze the transmittance spectrum. The optical transmittance of the glass substrate was found to be 90 % in the visible spectrum. A transmittance of 100% was obtained with air between the slits and detector on the optical fiber. However on inserting a glass slide, transmittance T reduced to about 90%.

At wavelengths less than 300 nm, there is no transmittance through the glass slide. For ITO thin-film layer on glass, it was observed that annealing increased its optical transmittance from 85 % to about 95% at wavelengths of 400 - 450 nm range. A maximum transmittance of 81% was obtained for the MoO₃ layer whilst for the MEH-PPV layer, a transmittance value of about 84% within a wavelength of 600-700nm was obtained (Figure 3.4). These high transmittance values imply that the layers will easily allow the light produced to emanate from the device anode.

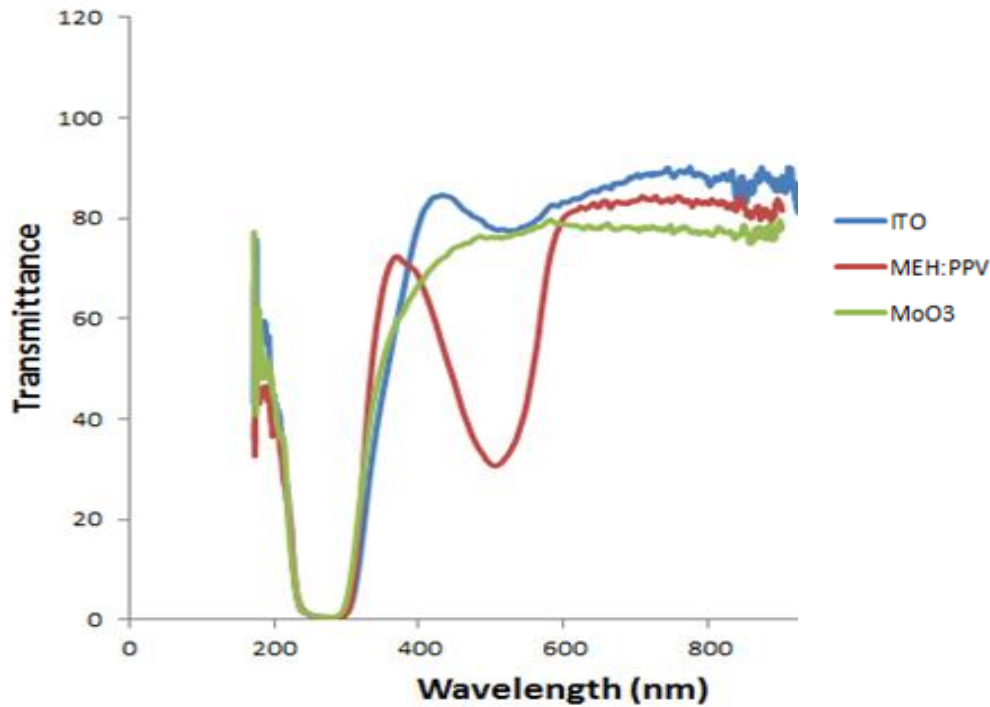


Figure 3.4: Transmittance spectrum of ITO, MEH:PPV and MoO₃ all deposited on glass.

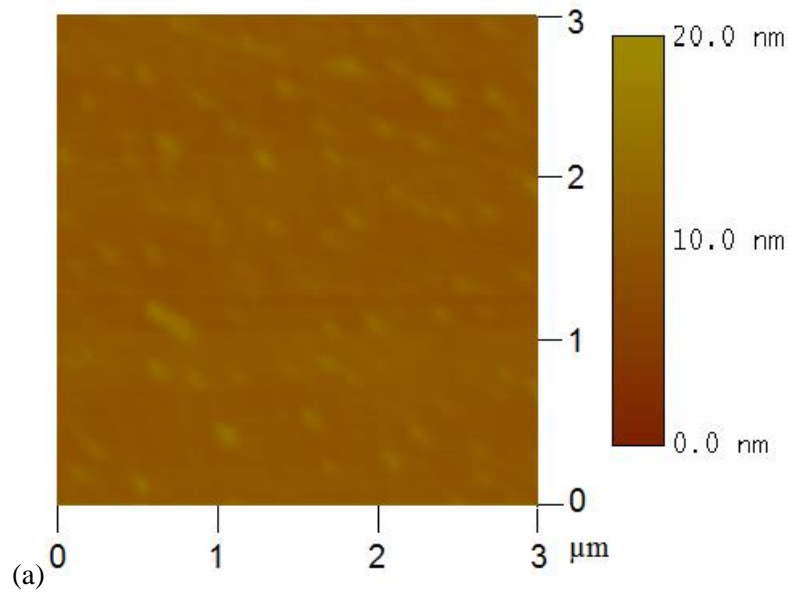
3.5.3 Nanoindentation Results

Typical scans of the MoO₃ thin film surfaces, obtained before and after indentation, are presented in Figure 3.5. In some materials, the volume under the indenter pushes out into the sides of the indenter during the indentation to form a pile-up profile. In those cases, the actual contact depth may be larger than the measured contact depth [35]. The image of Figure 3.5 shows that there is no significant pile-up during the indentation of MoO₃ thin films.

The resulting reduced Young's moduli and hardness values (obtained over a range of contact depths) are summarized in Figure 3.6. The results suggest that there is no strong correlation between the contact depth and the reduced Young's modulus or hardness. The measured root

mean square surface roughness for the MoO₃ substrate before indentation is 0.696±0.287 nm. The measured indentation depth at a range of 9 to 22 nm was to overcome the effects of surface roughness. The measured Young's modulus of MoO₃ was also lower than that of glass substrate, which is 70 GPa [33]. The results also show that the substrate effects are negligible when the moduli of the coating is smaller than that of the substrate, since the plastic deformation is constrained in the coating layer, as suggested by prior works of Saha and Ni_x [36].

The reduced Young's modulus and hardness of MoO₃ were measured to be 66.8±6.1 GPa and 2.6±0.7 GPa, respectively. The Young's modulus of MoO₃ was determined to be 64.6±6.2 GPa, assuming that the Poisson's ratio is 0.3.



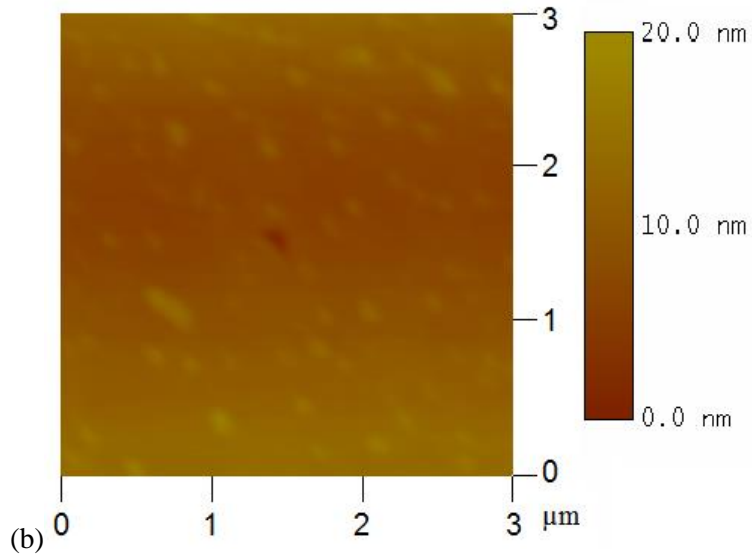


Figure 3.5: Typical surface profiles of MoO₃ thin film (a) before and (b) after nanoindentation measurement.

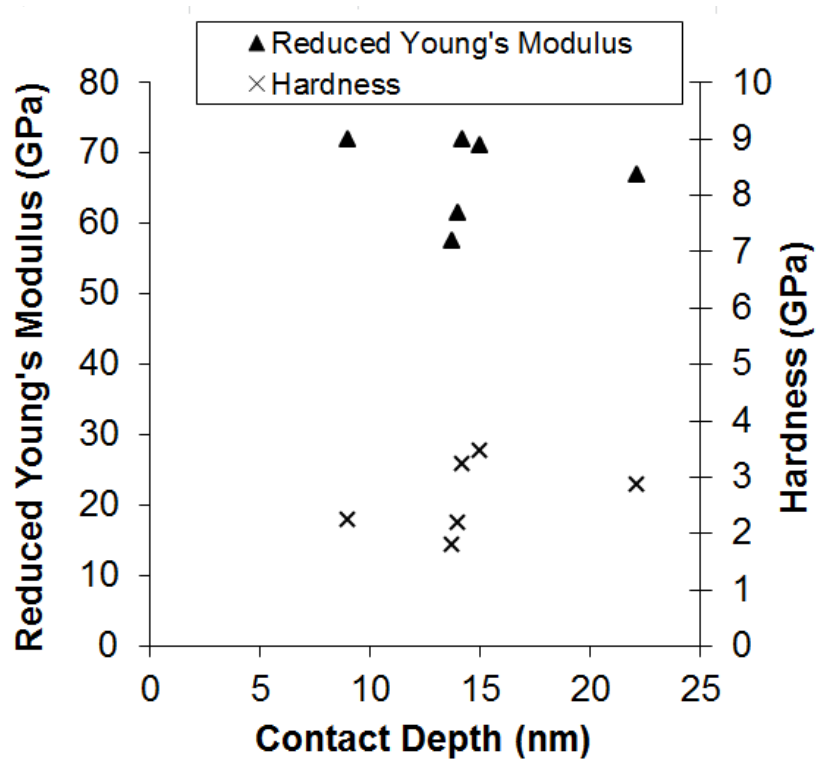


Figure 3.6: Reduced Young's modulus and hardness of MoO₃ thin film measured by nanoindentation.

3.5.4 Adhesion Measurements and Adhesion Energy

The tip radii of the MoO₃-coated AFM tips were measured to be 157.5 nm from the SEM images. The root mean square surface roughness of MEH-PPV substrates was measured from the surface profile obtained from AFM tapping scans to be 2.2±0.7 nm. Contact AFM experiments were performed using the MoO₃ coated tips and the MEH-PPV substrates. The pull-off force measured by AFM was 31.8±7.8 nN.

Also, the contact AFM experiments were performed using the MEH-PPV coated tips and PEDOT:PSS substrates. The tip radii of the MEH-PPV coated tip were measured to be 222 nm from the SEM images. The root mean square surface roughness of PEDOT:PSS substrate was measured from the AFM surface profile to be 0.6±0.1 nm. The pull-off force between the MEH-PPV coated tips and the PEDOT:PSS substrates were measured to be 59.3±8.4 nN.

The Young's modulus of MoO₃ was measured to be 64.6 GPa in this study. The Young's modulus of MEH-PPV was measured to be 11.5 GPa in prior studies [15]. The combined elastic modulus was calculated, assuming the Poisson's ratios of them to be both 0.3. The combined radius was calculated by assuming the substrate is a flat surface with an infinitely large radius, since the surface roughness of the substrate, 2.2 nm, is much smaller than the radius of the tip, 157.5 nm. The transition parameter, λ , was calculated to be in the intermediate range, where the MD model applies. The adhesion energy was determined to be 0.0398 J/m², by numerically solving equations (1), (4), (5) and (6).

In the case of the adhesion interaction between PEDOT:PSS and MEH-PPV, the Young's moduli

were measured in a previous study [15] to be 1.42 GPa and 11.5 GPa, respectively. The combined elastic modulus was calculated, assuming the Poisson's ratios of them to be both 0.3. The combined radius was determined by assuming the substrate is a flat surface with an infinitely large radius, since the surface roughness of the substrate, 0.6 nm is much smaller than the radius of the tip, 222 nm. The transition parameter, λ , was calculated to be greater than 5. Thus, the JKR model applies. Hence, the adhesion energy was calculated by JKR model from equation (2) to be 0.0567 J/m².

3.5.5 Evolution of Contact Profiles under Pressure

There are several analytical models relevant to the contact profile between thin layers. Most of the dust particles in the clean room have diameters of $\sim 1 \mu\text{m}$ [25]. The thickness of the emissive layer is $\sim 100 \text{ nm}$ and much smaller than that of height of the blister, i.e. the diameter of the dust particle. Hence, the stretching dominates the strain energy and membrane stretching model applies. By substituting the adhesion energy measured previous in this study, the radius of the blister between the emissive layer and hole-injection layer, before any pressure was applied, was calculated by equation (8) to be $6.52 \mu\text{m}$ for MoO₃-based OLEDs and $5.97 \mu\text{m}$ for PEDOT:PSS-based OLEDs.

The calculated initial blister radius was then incorporated into the finite element models to calculate the evolution of contact profile under pressure. The PDMS stamp compressed on the device and applied pressure onto the device. A typical calculated profile of a stamp on a MoO₃-based device under 14 MPa pressure is presented in Figure 3.7. The stamp has clearly deformed under pressure and made full contact with the top of the device. Being compressed by the stamp,

the top of the blister deformed and made contact with the substrate HIL. The radius of the blister decreased, since part of the internal surfaces of the blister made contact under pressure. Due to adhesion, the contacted internal surface of the blister remains in contact after the pressure is removed. The radius and the area of the blister can be used to characterize the efficiency of the pressure treatment.

It is also important to note that Figure 7 also shows that the dust particle indent into the substrate HIL, due to the applied pressure. Hence, the lowest point of the substrate surface was right beneath the dust particle, while the highest point of the substrate was at the edge of the model. The height difference between the highest and lowest points was defined as the sink-in depth. This was used to characterize the damage to the device.

The blister radius and area both decreased with increasing pressure, for either MoO₃-based or PEDOT:PSS-based device, as shown in Figure 3.8(a). However, the rate of decrease of blister radius and the area decreased at higher pressures. This was especially true when the pressure was greater than 8 MPa.

The blister radius and area are normalized in Figure 8(b). This shows that the normalized blister radius and area, for MoO₃-based and PEDOT:PSS-based device, exhibits a similar trend of evolution under pressure. The blister area for both the MoO₃-based and PEDOT:PSS-based devices decreased to ~ 60% of its initial value when the applied pressure reached 5.6 MPa. Also, the blister area further decreased to ~ 50% of its initial value, when the applied pressure reached 8.3 MPa.

Figure 3.8 (b) also shows that the sink-in depth increased under pressure. The rate of increase also decreased under pressure. The thickness of the MoO₃ and PEDOT:PSS layers are the same in the simulation. However, the sink-in depth into the MoO₃ layer is ~ 4 times smaller than that into the PEDOT:PSS layer. This is because the Young's modulus of MoO₃ is much greater than that of PEDOT:PSS. This phenomenon indicates that another advantage of MoO₃-based device over more conventional PEDOT:PSS-base device is that it has higher resistance to damage due to mechanical loads since it has higher stiffness.

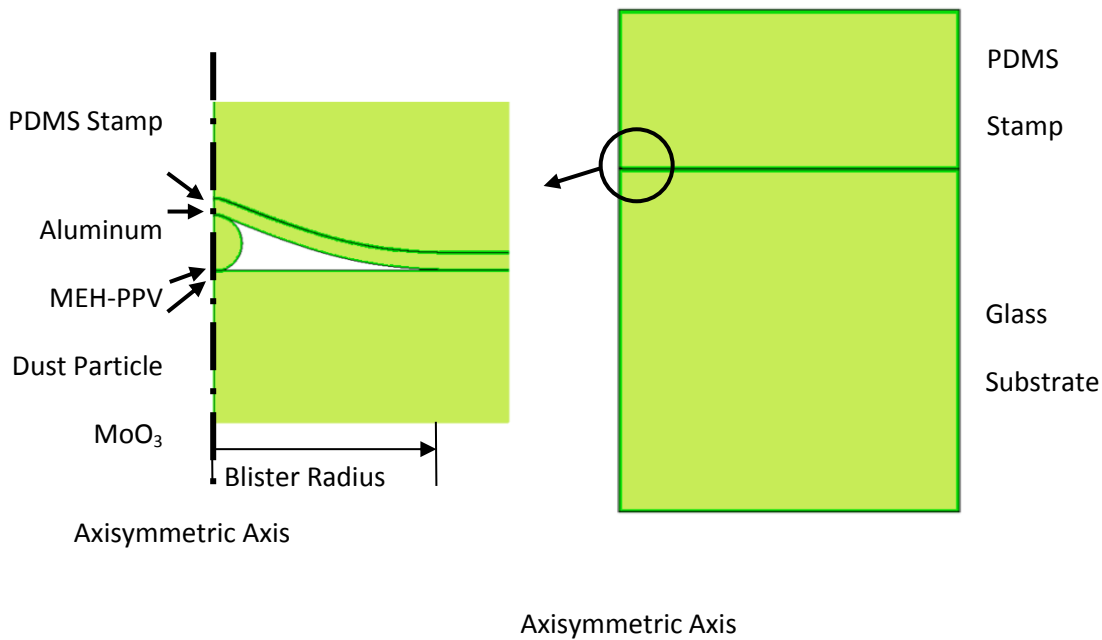
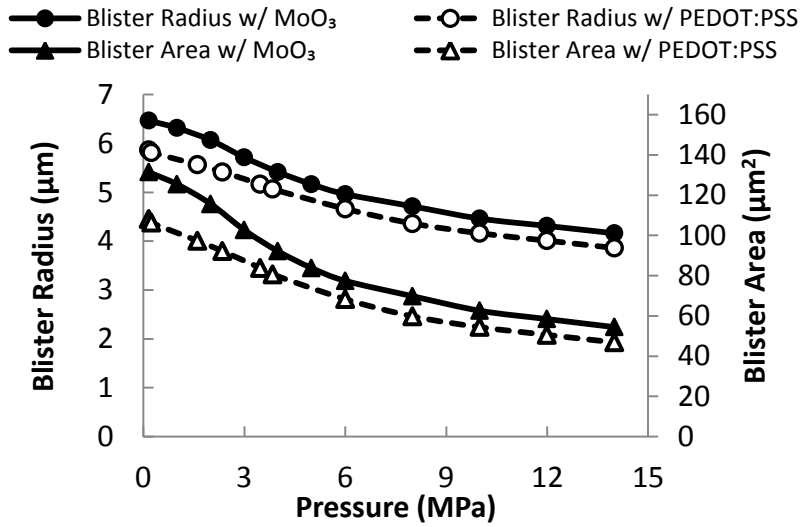
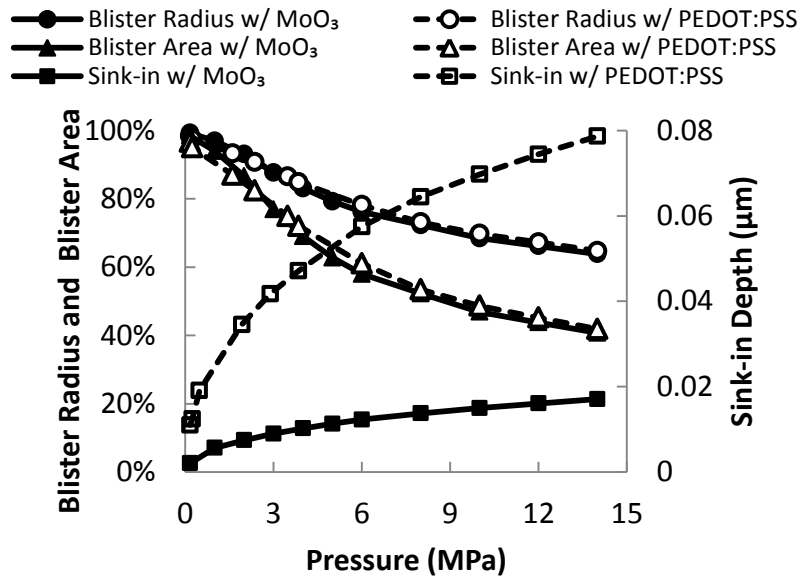


Figure 3.7 : FEA predicted contact profile of MoO₃-based device under 14 MPa pressure.



(a)



(b)

Figure 3.8: The evolution of blister morphology during the pressure treatment with (a) blister radius and area and (b) normalized blister radius and area and the sink-in depth.

3.5.6 Implications

This study provides a model for the mechanism of the electrical properties improvement of OLEDs after pressure treatment. The cause of the void space in the layered electronic devices could be the impurities in the environment, as modeled in this study. It is important to note here that the voids could also be intrinsic voids inside the materials. Also, the surface roughness of each layer could cause void spaces between the layers. In any case, all void spaces could shrink under pressure.

Furthermore, upon contact, the surfaces are likely to stay in contact, and thereby enhance charge transport across the layers. Hence, the resulting pressure-assisted increase of contact area should assist the hole transmission and charge transport through the layered structure of the OLEDs that were examined in this study. Hence, the reduced threshold voltages observed after the application of pressure (Figures 3(a) and 3(b)) are attributed largely to the effects of increased contact area after the application of pressure.

Also, the results of this study show a current-voltage characteristics improvement for the OLED fabricated using both spin-coating and thermal evaporation techniques prior to the pressure treatment. This suggests that the pressure treatment has a potential to improve the current-voltage characteristics for the devices fabricated by a range of deposition method.

However, the results of this study also show that the current-voltage characteristics of the OLED containing the MoO₃ HIL are better than those of the OLED with the conventional PEDOT:PSS HIL. This suggests that the combined use of pressure-assisted fabrication and improved hole-

injection layers could facilitate the future development of organic light emitting devices for applications in low cost lighting and displays.

Further work is clearly needed to explore the potential of other transition metal oxides as hole-injection layers in organic light emitting devices. These include: WO_3 , NiO , or V_2O_5 , that have been shown to have the potential to effectively replace PEDOT:PSS in OLEDs [4-6], OPV cells [2,7], and OTFTs [8].

There is also a need to explore a range of deposition methods for the fabrication of organic layers in polymer-based devices. These include spin-coating and thermal evaporation techniques that must be optimized prior to pressure-assisted fabrication. Such developments could facilitate the development of fast, low-cost stamping and roll-to-roll processes [37] for the fabrication of organic light emitting devices. The current work suggests that these are possible, provided sufficient pressures are applied, without inducing significant damage (sink-in) in the layered structures of the devices.

3.6 Summary and Concluding Remarks

In this chapter, we have presented the results of a combined experimental, theoretical and computational study on the pressure effects on the pressure facilitated fabrication of OLEDs. The OLEDs were fabricated using novel HIL material, MoO_3 , and the more conventional material, PEDOT:PSS, respectively. The current-voltage characteristics of the devices were measured before and after the pressure treatment. The results showed a dramatic decrease of the threshold voltage after the application of pressure. This was true for both the MoO_3 -based and

PEDOT:PSS-based devices. In order to study the mechanism of the pressure effects, nanoindentation method and AFM techniques were used, respectively, to measure the key mechanical properties (Young's moduli and hardness values) and adhesion energies of the layers and interfaces. The measured properties were then incorporated into analytical models for the calculation of the contact profiles around dust particles interposed between the HIL and EML. A finite element model was used to simulate the evolution of contact profile under pressure. The results suggest that the application of pressure, to the evaporated or spin-coated device layers, reduces the blister area surrounding the interposed dust-particle. This increases the contact area between the HIL and EML. Since such significant increase in the contact area would facilitate charge transport across interfaces in the OLED structures, we attribute the reduction of the threshold voltages of the pressure-assisted devices to the improvement of the charge transport across interfaces with increased contacts. However, it is important to note that excessive lamination pressure may also induce device damage due to the sink-in of dust particles. This suggests the need to optimize the pressure for improved surface contact without significant damage.

References

- [1] T. W. Lee, J. Zaumseil, Z. Bao, J.W.P. Hsu and J.A. Rogers, "Organic light-emitting diodes formed by soft contact lamination", *Proc. Natl. Acad. Sci. U.S.A.* 101,429-33 (2004).
- [2] V. Shrotriya, G. Li, Y. Yao, C. W. Chu and Y. Yang, "Transition metal oxides as the buffer layer for polymer photovoltaic cells", *Appl. Phys. Lett.* 88, 073508 (2006).
- [3] J. Meyer, K. Zilberberg, T. Riedl and A. Kahn, "Electronic Structure of Vanadium pentoxide: An efficient hole injector for organic electronic materials", *J. App. Phy.* 110, 033710 (2011).

- [4] K. J. Reynolds, J. A. Barker, N. C. Greenham, R.H. Friend and G. L. Frey, “Inorganic solution-processed hole-injecting and electron-blocking layers in polymer light-emitting diodes”, *J. App. Phy.* 92, 7556 (2002).
- [5] H. You, Y. Dai, Z. Zhang and D. Ma, “Improved performances of organic light-emitting diodes with metal oxide as anode buffer”, *J. App. Phy.* 101, 026105 (2007).
- [6] W.-J. Shin, J.-Y. Lee, J.C. Kim, T.-H. Yoon, T.-S. Kim, and O.-K. Song, “Bulk and interface properties of molybdenum trioxide-doped hole transporting layer in organic light-emitting diodes”, *Org. Electron.* 9, 333–338 (2008).
- [7] Y.-C. Tseng, A.U. Mane, J.W. Elam, and S.B. Darling, “Ultrathin molybdenum oxide anode buffer layer for organic photovoltaic cells formed using atomic layer deposition”, *Sol. Energy Mater. Sol. Cells* 99, 235–239 (2012).
- [8] C.-W. Chu, S.-H. Li, C.-W. Chen, V. Shrotriya, and Y. Yang, “High-performance organic thin-film transistors with metal oxide/metal bilayer electrode”, *Appl. Phys. Lett.* 87, 193508 (2005).
- [9] J. Meyer, A. Shu, M. Kröger, and A. Kahn, “Effect of contamination on the electronic structure and hole-injection properties of MoO₃/organic semiconductor interfaces”, *Appl. Phys. Lett.* 96, 133308 (2010).
- [10] J.H. Kim, S. Seo, and H.H. Lee, “Nanovoid nature and compression effects in organic light emitting diode”, *Appl. Phys. Lett.* 90, 143521 (2007).
- [11] M. Fina, D. Liu, L. Ren, and S.S. Mao, “Improving organic light-emitting diode performance with patterned structures”, *Appl. Phys. A* 105, 323–327 (2011).
- [12] Z.Y. Jiang and X.A. Cao, “Stress-induced current and luminescence modulations in an organic light-emitting device”, *Appl. Phys. Lett.* 97, 203304 (2010).
- [13] C. Kim and S. Forrest, “Fabrication of Organic Light-Emitting Devices by Low-Pressure Cold Welding”, *Adv. Mater.* 15, 541–545 (2003).
- [14] Y. Cao, C. Kim, S.R. Forrest, and W. Soboyejo, “Effects of dust particles and layer properties on organic electronic devices fabricated by stamping”, *J. Appl. Phys.* 98, 033713 (2005).
- [15] J. Du, T. Tong, W. Akande, A. Tsakiridou, and W. Soboyejo, “Pressure Effects on the Lamination of Organic Light-Emitting Diodes”, *J. Disp. Technol.* 9, 601–606 (2013).

- [16] International Organization for Standardization, ISO 14577-1:2002, Metallic Materials, Instrumented Indentation Test for Hardness and Materials Parameters - Part 1: Test Method (2002).
- [17] W.C. Oliver and G.M. Pharr, “An improved technique for determining hardness and elastic modulus using load and displacement sensing indentation experiments”, *J. Mater. Res.* 7, 1564–1583 (1992).
- [18] K. V Wolf, Z. Zong, J. Meng, A. Orana, N. Rahbar, K.M. Balss, G. Papandreou, C.A. Maryanoff, and W. Soboyejo, “An investigation of adhesion in drug-eluting stent layers”, *J. Biomed. Mater. Res. A* 87, 272–81 (2008).
- [19] F.M. Serry, Improving the Accuracy of AFM Force Measurements: The Thermal Tune Solution to the Cantilever Spring Constant Problem (Veeco Instruments Inc., Santa Barbara, pp. 1–4 (2005),).
- [20] D. Maugis, “Adhesion of spheres: the JKR-DMT transition using a Dugdale model”, *J. Colloid Interface Sci.* 150, 243–269 (1992).
- [21] K.L. Johnson, K. Kendall, and A.D. Roberts, “Surface energy and the contact of elastic solids”, *Proc. R. Soc. A Math. Phys. Eng. Sci.* 324, 301–313 (1971).
- [22] B. V Derjaguin, V.M. Muller, and Y.P. Toporov, “Effect of contact deformations on the adhesion of particles”, *J. Colloid Interface Sci.* 53, 314–326 (1975).
- [23] R. Carpick, D. Ogletree, and M. Salmeron, “A general equation for fitting contact area and friction vs load measurements”, *J. Colloid Interface Sci.* 211, 395–400 (1999).
- [24] O. Piétremont and M. Troyon, “General equations describing elastic indentation depth and normal contact stiffness versus load”, *J. Colloid Interface Sci.* 226, 166–171 (2000).
- [25] W.M. Moreau, *Semiconductor Lithography: Principles, Practices, and Materials* (Plenum Press, New York, 1988).
- [26] International Organization for Standardization, ISO 14644-1:1999 Cleanrooms Of, and Associated Controlled Environments-Part I: Classification of Air Cleanliness (ISO, Switzerland, 1999).
- [27] W.O. Akande, Y. Cao, N. Yao, and W. Soboyejo, “Adhesion and the cold welding of gold-silver thin films”, *J. Appl. Phys.* 107, 043519 (2010).
- [28] B.M. Malyshev and R.L. Salganik, “The strength of adhesive joints using the theory of cracks”, *Int. J. Fract.* 26, 261–275 (1984).
- [29] K. Wan and Y. Mai, “Fracture mechanics of a shaft-loaded blister of thin flexible membrane on rigid substrate”, *Int. J. Fract.* 74, 181–197 (1990).

- [30] Z. Zong, C.-L. Chen, M.R. Dokmeci, and K. Wan, “Direct measurement of graphene adhesion on silicon surface by intercalation of nanoparticles”, *J. Appl. Phys.* 107, 026104 (2010).
- [31] A. Bietsch and B. Michel, “Conformal contact and pattern stability of stamps used for soft lithography”, *J. Appl. Phys.* 88, 4310 (2000).
- [32] N. Bowden, S. Brittain, A.G. Evans, J.W. Hutchinson, and G.M. Whitesides, “Spontaneous formation of ordered structures in thin films of metals supported on an elastomeric polymer”, *Nature* 393, 146 (1998).
- [33] W. Soboyejo, *Mechanical Properties of Engineered Materials* (CRC, New York, 2003).
- [34] D. Neerincx and T.J. Vink, “Depth profiling of thin ITO films by grazing incidence X-ray diffraction”, *Thin Solid Films* 278, 12–17 (1996).
- [35] W.C. Oliver and G.M. Pharr, Measurement of hardness and elastic modulus by instrumented indentation: Advances in understanding and refinements to methodology, *J. Mater. Res.* 19, 3–20 (2004).
- [36] R. Saha and W.D. Nix, Effects of the substrate on the determination of thin film mechanical properties by nanoindentation, *Acta Mater.* 50, 23–38 (2002).
- [37] S.R. Forrest, The path to ubiquitous and low-cost organic electronic appliances on plastic, *Nature* 428, 911–8 (2004).

Chapter 4

Adhesion in Organic Light Emitting Devices

4.1 Introduction

Adhesion which is the attraction between dissimilar materials is very critical in micro- and nano-electronic structures. Interfacial delamination represents a major reliability issue in organic electronic diodes and other organic electronic systems. It arises due to poor adhesion at their interfaces. The interfacial properties are therefore crucial for materials selection and process control.

In this chapter, we use atomic force microscopy (AFM) to measure the adhesion between layers that are relevant to OLEDs [1]. Adhesion measurements can also be made using procedures such as contact angle test [2], scratch test [3,4] and peel [3,4]. These methods fall short of capturing micro- and nano-scale details in adhesion measurements. AFM tips are coated with one material and a rigid substrate such as soda lime glass is coated with the other material. Pair-wise interactions to determine the adhesion force in this bi-material setup is carried out.

Linear elastic fracture mechanics (LEFM) is usually employed to study interfacial adhesion and fracture toughness [5]. This has some shortcomings because it doesn't fully characterize the nonlinearity of the interfaces. This is implemented using the FEA package, ABAQUS vs 6.12.

In this study, we consider six model system by approaches based on LEFM. The interfaces of interest here are glass/Indium Tin Oxide (glass/ITO); poly (3,4-ethylenedioxythiophene)-

polystyrene sulfonate/poly(1,2-methoxy-5(2'-ethylhexyloxy)-poly(phenylene vinylene) (PEDOT:PSS/MEH-PPV); PEDOT:PSS/MEH-PPV + Titanium oxide (TiO₂); MEH-PPV/Aluminum (Al); MEH-PPV + TiO₂/Al. In general we study interfacial fracture behavior at different organic/organic, inorganic/organic or metal/organic interfaces.

For each system, we analyze the effect of initial defects on the strain energy release rate. The implications of the results are discussed for the material selection and design of robust interfaces for OLEDs systems.

4.2 Theory of Adhesion

In the contact mode, AFM can be used to measure the pull-off force between two surfaces [6]. Figure 4.1 illustrates the steps involved in the measurement of pull-off forces. First, the micro-fabricated cantilever probe is attached to a scanner head that is lowered towards the surface at a constant velocity (Figure 4.1A). Since the probe approaches the surface under ambient conditions, the cantilever experiences negligible interactions with the surrounding medium and the cantilever deflection remains close to zero.

However, as the cantilever is lowered further down, it is eventually pulled into contact with the surface by adhesive force interactions (Figure 4.1B) between the tip of the cantilever and the surface. Subsequently, the scanner continues to move down but with the substrate and probe in continuous contact, the cantilever bends (Figure 4.1C) under elastic deformation. Upon reversal of the cantilever displacement direction, the scanner head is raised and the cantilever's elastic deformation is reversed. However, residual adhesive interactions prevent the tip from detaching from the substrate's surface at zero load (Figure 4.1D).

Hence, the reversed loading of the cantilever must be continued until the adhesive forces are eventually overcome at a negative force that corresponds to the pull-off force (Figure 4.1E). The measured displacement deflection can then be related to the adhesion force via Hooke's Law. This gives:

$$F = kx \quad (4.1)$$

where F is the adhesion force, k is the spring constant of the cantilever, and x is the cantilever deflection after the tip separates from the substrate upon retraction. The accuracy of these measurements of the adhesion force depends significantly on the careful measurement of the spring constant, k , of the AFM cantilever.

While values for the spring constant are provided by most cantilever manufacturers, these are batch estimates that are often significantly different from actual values for each k . A thermal tune method has been developed [7] that offers a real time and accurate technique for the measurement of spring constants that are used in the calculation of pull-off forces. This method involves the measurement of the cantilever's response in the presence of thermal agitations. It then uses a Lorentzian line shape fit to obtain an accurate estimate of the spring constant from the resulting frequency spectrum of harmonic oscillations. This method was used in the measurement of the spring constant of each of the cantilevers that were used in this study. Details of the thermal tune method are given by Veeco Instruments, Inc. [7].

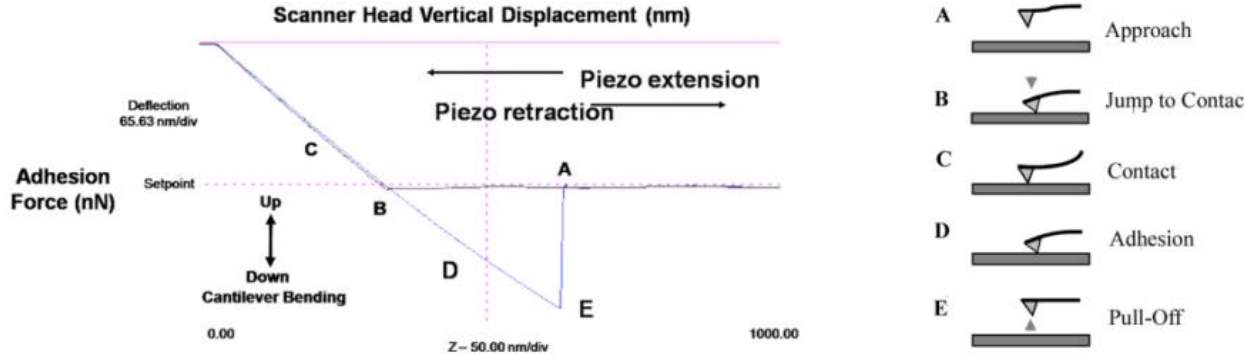


Figure 4.1: Schematic Force-Displacement Curve Depicting the Various Stages (A-E) of Cantilever-Surface Engagement

It is possible to extend measurements of the adhesion force between two surfaces to determine the adhesion energies for the interfaces between dissimilar materials. Various adhesion models exist to take into account the different material and geometric properties of the interacting layers. At one end of the spectrum, the Derjaguin-Muller-Toporov (DMT) model [8] can be used to characterize weak long-range interactions between stiff materials with small radii. In this case, the adhesion energy, γ , is related to the adhesion force, $F_{adhesion}$, experienced between a spherical particle of radius, R , and a planar surface, by:

$$\gamma_{DMT} = \frac{F_{adhesion}}{2\pi R} \quad (4.2)$$

Note that in the case of two contacting spheres, R , can be calculated through: [37]

$$R = \frac{R_1 R_2}{R_1 + R_2} \quad (4.3)$$

Equation 4.3 for the effective radius also applies to idealizations of curved contacts with partial arcs. In practice, atomic scale roughness of the surface layers can affect the calculation of surface energies predicted through conventional continuum mechanics theories [9]. However, first-order

simplifications can be used to approximate the contact radii. In the case of contact mode atomic force microscopy, the cantilever's tip radius can be approximated as R_1 and the root means square (rms) roughness of the asperities on the substrate layer can be considered as an approximation of R_2 [10], [11]-[13].

On the other end of the spectrum, the Johnson-Kendall-Robert (JKR) model [9] applies to strong near-range adhesive forces between compliant materials with large radii. In this case, the adhesion force and energy is related by:

$$\gamma_{JKR} = \frac{2F_{adhesion}}{3\pi R} \quad (4.4)$$

For the Maugis-Dugdale (MD) model [11] that lies between these two limiting cases, analytical methods must be used to calculate the relationship between the adhesion force and energy. This can be a cumbersome task that can be somewhat simplified using an iterative process, introduced by Carpick et al. [12] and further developed by Pietrement and Troyon [13], to reach a generalized approximation of the MD adhesion energy to within 1% accuracy. Such calculations require knowledge of a combination of material and geometric properties, and can be used to characterize the entire range of adhesion models through the calculation of a non-dimensionalized parameter, λ :

$$\lambda = 2\sigma_o \left(\frac{R}{\pi k^2 \gamma} \right)^{1/3} = -0.913 \ln(1 - 1.018\alpha) \quad (4.5)$$

Here, α is another non-dimensionalized parameter whereby $\alpha = 1$ corresponds to the JKR case and $\alpha = 0$ corresponds to the DMT case. Meanwhile, the constant, κ , in Equation 5 is obtained from:

$$k = \frac{4}{3} \left[\frac{(1-\nu_1^2)}{E_1} + \frac{(1-\nu_2^2)}{E_2} \right]^{-1} \quad (4.6)$$

where ν_i is the Poisson's ratio for layers $i = 1, 2$ and E_i corresponds to the elastic moduli for these layers. Furthermore, σ_o in Equation 5 is a constant adhesive force between two bodies, and is non-zero at small distances, h . Separation between the bodies will occur at a separation height, defined as h_o , after which $\sigma_o = 0$. The two terms are related to the adhesive energy through:

$$\sigma_o h_o = \gamma \quad (4.7)$$

According to the Carpick model [12], the adhesion energy is then related to the adhesion force through:

$$\gamma = \frac{F_{adhesion}}{\pi R \bar{F}_{adhesion}} \quad (4.8)$$

where:

$$\bar{F}_{adhesion} = 0.267\alpha^2 - 0.767\sigma + 2 \quad (4.9)$$

Values of $\lambda < 0.1$ correspond to the DMT model, while scenarios in which $\lambda > 5$ correspond to the JKR model. Intermediate values correspond to the MD range. As a result of the inter-dependence of terms in Equations (4.5)-(4.9), an iterative approximation is necessary. Nevertheless, the above expressions can be used to convert the pull-off forces, obtained from the AFM adhesion experiments, to measurements of adhesion energy over a wide range of scenarios.

4.3 Experiments

4.3.1 OLED Fabrication

In this work, a model OLED (Figure 4.2a) was studied in an effort to quantify the adhesion between organic-organic, organic-inorganic, and inorganic-inorganic material interfaces that are found in organic electronic structures. These configurations were selected as representative multilayer devices with constituents that are commonly found in organic structures [14]-[16] deposited on rigid glass substrates. For our experiments, substrate layers were isolated and patterned directly on cleaned silica substrates in order to remove effects of material interlayers on mechanical properties such as elastic modulus or roughness.

Indium tin oxide (ITO) was deposited onto soda lime glass substrates by sputtering from an ITO ceramic target using an Edwards Auto E306A r.f. magnetron sputtering deposition system (Edwards Limited, Sussex, UK). The sputtering process parameters were 0.64 W/cm^2 r.f. power density, 0.8 sccm Ar flow rate, deposition pressure of 3.2×10^{-3} Torr and deposition temperature of $\sim 25\text{-}30^\circ\text{C}$. The ITO layer in the devices is typically coated by a conducting polymer based on special formulations of poly(3, 4-ethylene dioxythiophene) (PEDOT) doped with poly(styrene sulphonate) (PEDOT:PSS) that facilitates hole transport between the ITO and active layer. Baytron P VP Al-4083 PEDOT:PSS (now Heraeus Clevios, Hanau, Germany) was chosen because of its reduced mean particle size and narrower size distribution, which reduces electrical “shorts” in the device and smoothens the surface. It was filtered through a $0.2 \mu\text{m}$ filter to further improve smoothness and uniformity.

This was done for 1 minute at a rate of 3000 rpm. The spin-coated mixture was then cured at 120°C for 5 minutes to remove moisture.

The OLED used poly[2-methoxy-5-(2'-ethyl-hexyloxy)-1,4-phenylene vinylene] (MEH:PPV) as a photo-emissive layer in which electrons and holes supplied by the cathode and anode recombine to generate an orange-reddish light. The MEH:PPV (Sigma Aldrich, St. Louis, MO) was mixed with chloroform at a 5 mg/mL ratio. The mixture was then covered and stirred continuously for at least 6 hours at room temperature. The mixture was passed through a 0.45 μm Teflon filter. The filtered solution was then spin-coated onto the above deposited PEDOT:PSS layer 1000 rpm for 60 seconds.

To complete the devices, Aluminum was used as the cathode layer. 100 nm thick, of Al was thermally evaporated on the above MEH:PPV layer using an Edwards E306A deposition system (Edwards, Sussex, UK).

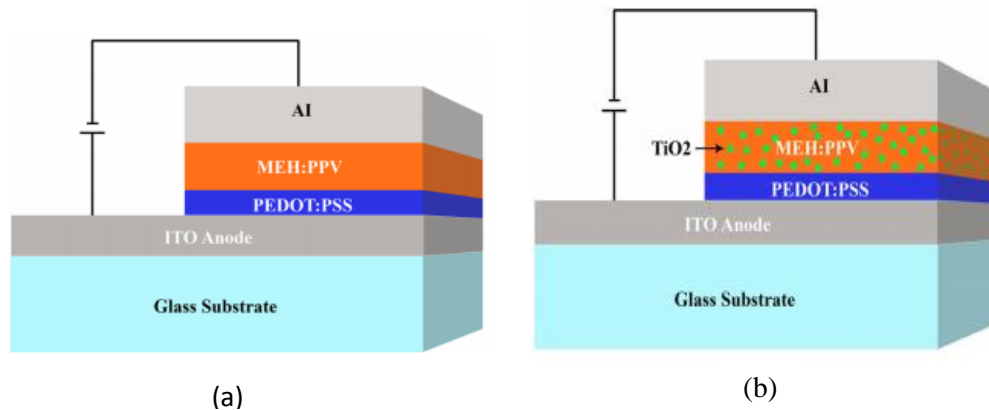


Figure 4.2: Schematic of (a) model OLED and (b) model HOILED structure.

4.3.2 HOILED Fabrication

Material preparation of the Hybrid Organic/Inorganic LEDs (HOILEDs) followed similar procedures as those outlined in Section 4.1, with the exception of active layers that were prepared to study the effects of TiO₂ nanoparticles. In the HOILED devices, only the effects of TiO₂ nanoparticle additives in the MEH:PPV layer were considered, since MEH:PPV is a single polymer blend (Figure 4.2b). MEH: PPV: TiO₂ was, therefore, prepared by mixing 15 mg of MEH: PPV in 2 mL of chloroform at room temperature for 6 hours. 5 mg of TiO₂ was sonicated in 2 mL of chloroform for 45 minutes and then the two mixtures were combined and sonicated for an additional 30 minutes.

Spin coating of the filtered solutions was then carried out in a Laurell spin coating system (WS-650MZ, Laurell, North Wales, PA, USA) at 500 rpm for 30 seconds yielded layer thicknesses of ~107 nm, as measured with a KLA-Tencor/ P-15 Surface Profiler (KLA-Tencor, Milpitas, CA).

4.3.3 AFM Experiments

Etched silicon Contact AFM cantilever probes were purchased from Veeco Instruments (Woodbury, NY). These cantilevers were coated with the complementary materials that make direct contact with the surfaces that simulate the wide range of interfaces in Figures 4.2a and 4.2b. The substrates were coated with the same deposition methods that were used in the fabrication of the model OLED and OPV structures. However, the polymer coating of the AFM cantilever probes were done using a dip-coating technique developed in prior studies by Zong et al. [17]. ITO coating of the cantilevers was performed at the Sheda

Science and Technology Complex (SHESTCO) in Abuja, Nigeria, using a Radio Frequency (RF) magnetron sputtering system (Edwards, Sussex, UK) [18].

Contact mode AFM experiments were performed in air, over a temperature range of 22-25°C and relative humidity range of 31-46%. At least six force curves were collected for each interaction using a Digital Instruments Dimension 3000 AFM (Digital Instruments, Plainview, NY). This was used to measure the deflection of the AFM cantilevers as they came into contact with the substrate. The stiffness of each cantilever was measured using the thermal tune method [7], [19]. This was carried out with a Digital Instruments Nanoscope IIIa AFM (Digital Instruments, Plainview, NY). In this way, the spring constants of the individually-coated cantilevers were obtained to measure the adhesion forces. Since the AFM measurements are highly sensitive to surface roughness, the tip radii and substrate roughnesses were measured before each experiment.

The tip radii were calculated from profile images captured with a Scanning Electronic Microscope (Philips FEI XL30 FEG-SEM, Hillsboro, OR) at 3500-4000 magnification (FIG. 4). Selected tip radii were measured before and after AFM characterization in order to take into account potential tip deformation during the course of the experiments. For example, an OLED PEDOT:PSS-coated tip's radius increased from 88 nm to 110 nm (125% increase) after one set (six measurements) of contact AFM interactions. However, this difference was not considered to be significant, since the small surface roughness values overshadowed these tip radii measurements in the calculations of effective radius.

Using the Dimension AFM under tapping mode, 8 height and phase images of each layer (Figure 4. 4) were used to measure the root mean squared (rms) surface roughnesses

within areas ranging from $1 \times 1 \mu\text{m}$ to $10 \times 10 \mu\text{m}$ (Tables 4.1 and 4.2). The measured surface roughnesses and tip radii were then incorporated into Equations (4.2) and (3) to calculate the adhesion energies.

4.4 Finite Element Modeling of Interfacial Fracture/Delamination

Interfacial failure represents a major reliability issue in micro- and nano-electronic systems [20]. In order to study the integrity of the bi-material interfaces relevant in the OLED structures considered in our current study, finite element analysis (FEA) was carried out in this section. This was used to predict the failure behavior of such interfaces. Interfacial adhesion and fracture toughness were characterized using linear elastic fracture mechanics (LEFM) concepts. The energy release rates (of each relevant interface) were determined studied as a function of interfacial crack size. Since the interfaces were subjected to mix mode loading, we study the evolution of the energy release rate with mode mixity. This was implemented using the FEA package, ABAQUS Version 6.12(ABAQUS, Pawtucket, Rhode Island, USA).

In this study, we consider six model systems within an LEFM framework. The interfaces of interest here are: glass/Indium Tin Oxide (glass/ITO); poly (3,4-ethylenedioxythiophene)-polystyrene sulfonate/poly(1,2-methoxy-5(2'-ethylhexyloxy)-poly(phenylene vinylene) (PEDOT:PSS/MEH-PPV); PEDOT:PSS/MEH-PPV + Titanium oxide (TiO_2); MEH-PPV/Aluminum (Al); MEH-PPV + TiO_2 /Al. In general we study interfacial fracture behavior at different organic/organic, inorganic/organic or metal/organic interfaces

For each system, we compare the critical values of the energy release rate with measured interfacial adhesion of the multilayers. The implications of the results are discussed for the material selection and design of robust interfaces for OLEDs systems with enhanced lifetimes.

A typical finite element model is presented in Figure 4.3. It shows an MEH-PPV layer on a PEDOT:PSS layer. Note that the material of each layer is marked in the figure.

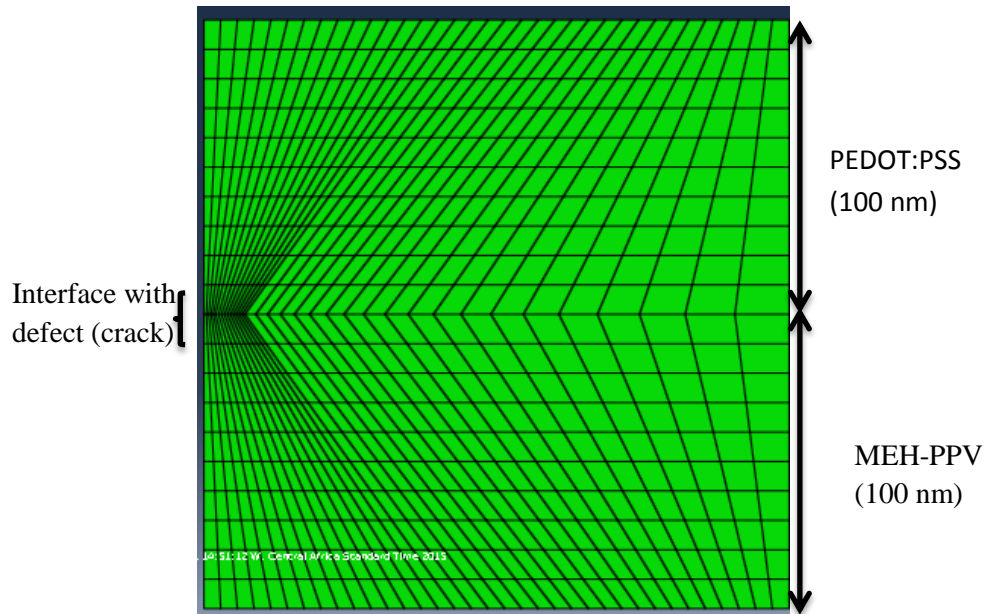


Figure 4.3: Typical finite element model with initial interfacial crack shown.

A 4-node bilinear plane strain quadrilateral element was used in the mesh. The mesh was dense in the regions near the cracks and the contact surfaces. Similar mesh sizes were also used in the regions near the surface contact regimes to enable convergence in contact simulation. It was assumed that all the materials exhibited isotropic elastic behavior.

Young's moduli were obtained from the nanoindentation experiments described earlier in chapter 3, as well as from prior studies [21-24]. The bottom of the substrate was fixed to have no displacements and rotations. The outer edge of the model was fixed to have no lateral movement for continuity. A uniformly distributed tensile load was applied from the top of the bimaterial

structure. For simplicity and convergence, frictionless contact was assumed between contact surfaces. In each bimaterial structure, the effect of the initial crack size on the energy release rate is studied for three different loads of 10 N, 20 N and 30 N. The results are compared with the interfacial adhesion energies obtained from the AFM measurements.

4.5 Results and Discussion

4.5.1 Surface Morphology

The different materials in the OLED exhibited a wide range of surface morphologies when deposited directly onto plain glass (Figure 4.4). Differences were visibly apparent from the height and phase scans and quantified by the average roughness results (Table 4.1). The majority of the layers in the OLEDs were highly-uniform and rms roughness values averaged between 0.1 to 2.9 nm. Measured tip radii, on the other hand, averaged around 170 ± 60 nm, with an uncoated tip radius of ~ 100 nm. Nano-scale roughnesses, therefore, dominated the interactions between asperities.

Table 4.1: Average roughness (Ra) and thickness of different OLED layer structures.

Structure	Average roughness (nm)	Thickness (nm)
ITO/Glass	0.70 ± 0.03	100
PEDOT:PSS/Glass	3.5 ± 0.3	100
PEDOT:PSS/ITO (annealed at 100°C)	3.9 ± 0.3	100
PEDOT:PSS/ITO	3.6 ± 0.2	100

(annealed at 250°C)		
MEH-PPV/Glass	11.7 ± 0.8	110
Aluminum/Glass	1.7 ± 0.3	200

4.5.2. Force-Displacement Characteristics

A typical AFM force curve is presented in Figure 4.5. This shows a plot of cantilever displacement against scanner displacement, for a pair-wise interaction between an MEH:PPV-coated cantilever and PEDOT:PSS-coated glass slide. No hysteresis was observed in the force-displacement curve. The surface pair interactions exhibited a wide range of adhesive forces, as shown in Figure 4.6 in which the pull-off forces are presented. In the case of the pair-wise interactions between the individual OLED layers, the pull-off forces ranged from 10 ± 2.0 nN for MEH:PPV-Al to 59 ± 14 nN for glass-ITO and 59 ± 8.4 nN for PEDOT:PSS-MEH:PPV. For the OPV cells, these values ranged from 9.2 ± 1.9 nN for the ITO-PEDOT: PSS interaction to 59 ± 14 nN for the glass-ITO pair.

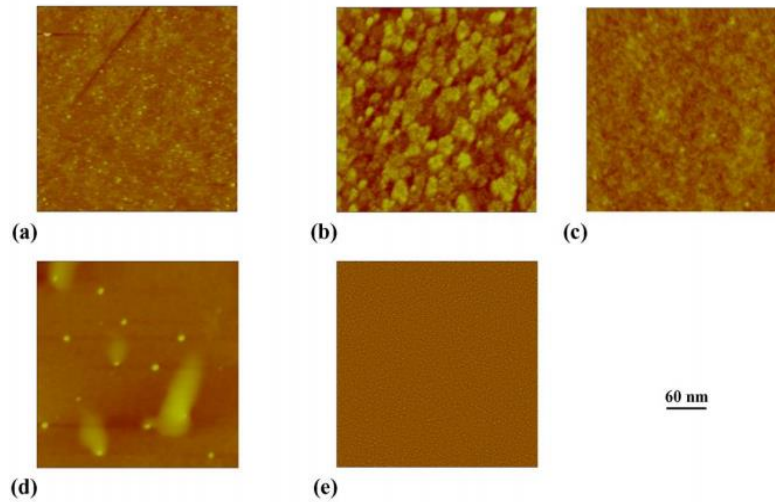


Figure 4.4: Sample 3 μm Tapping AFM Height Images for Different Layers in OLED Structures. (a) plain glass, (b) ITO-coated glass, (c) Baytron P VP AL-4083 PEDOT:PSS, (d) MEH:PPV, (e) Al

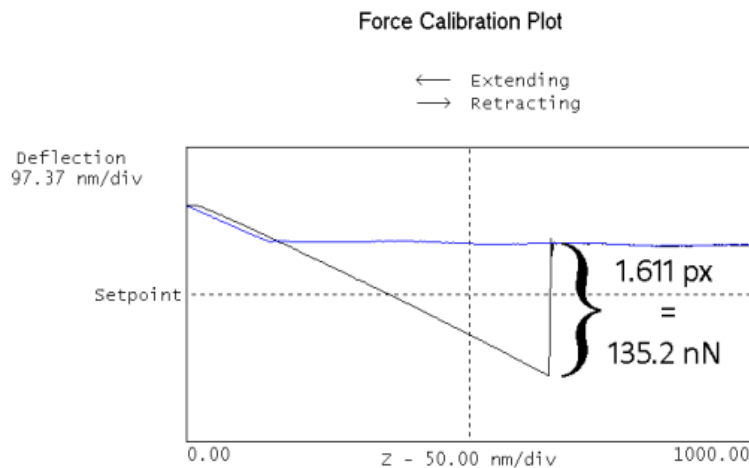


Figure 4.5: Typical AFM Force-Displacement Curve Obtained Between MEH: PPV and PEDOT: PSS. In this image, the separation height is 1.611 pixels. With a measured tip spring constant of 0.323 N/m, this corresponds to a pull-off force of 135.2 nN (from Hooke's Law).

4.5.3. Adhesion Energies of Organic Electronic Devices

The disparity in the adhesive interactions between the different layers becomes more evident once adhesion energies are taken into account. This is because the calculation of the adhesion energy takes into account the geometric and material properties of the different materials. By performing the iterative calculations using equations 4.5-4.9, λ was found to be on the order of $10^{-8} \ll 0.1$ for each experiment. This confirmed that the interactions could be characterized by the DMT model (Equation 4.2), as would be expected, given the relatively weak range of forces in question.

While converting the measured adhesion forces into adhesion energies, the surface roughnesses of the contacting surfaces (Figure 4.7) were found to have a significant effect on correcting the relative strengths of the adhesive interactions. For example, the high surface roughness of MEH: PPV could be seen to have a significant effect on the adhesion energy considering its interactions with Aluminum.

In the OLED, the PEDOT: PSS/MEH: PPV interface exhibited an adhesion energy of $\sim 15 \pm 2.1 \text{ J/m}^2$. This was greater than that of all other material pairs without TiO_2 particles in the MEH-PPV system, since all other adhesion energies were under 10 J/m^2 (Figure 4.6).

The adhesive interactions between organic-organic (PEDOT: PSS/MEH: PPV), organic-inorganic (ITO/PEDOT: PSS, or MEH: PPV/Al), or inorganic-inorganic (Glass/ITO) materials are summarized in Table 4.2. These results show clearly that for the OLEDs, the organic-organic pairs exhibited the strongest adhesion (at $\sim 15 \text{ J/m}^2$), while the organic-inorganic interactions were the weakest (range: $0.8 - 1.7 \text{ J/m}^2$, average $\sim 1.2 \pm 0.7 \text{ J/m}^2$). The intermediate adhesion strengths were obtained for the inorganic-inorganic

glass-ITO interaction ($\sim 9.3 \text{ J/m}^2$). In this case, the organic-inorganic interactions (range: 0.50 - 12 J/m^2 , average $\sim 6.2 \pm 0.8 \text{ J/m}^2$) presented the intermediate case.

The (sometimes large) variation in adhesion forces are presumed to stem from a number of potential factors. These include: surface roughnesses, water adsorption, and surface charge variations. While rms roughness values capture the peak-trough variations in surface morphology, the calculations ignore textures on the surfaces that could give rise to sub-scale roughness variations on the peaks and valleys themselves. This is particularly likely when the measured peaks and troughs arose from the accumulation of particles, such as polymer chains, spread out through the film layer.

In contrast, the extremely low rms roughness of the Baytron P VP Al-4083 PEDOT: PSS ($0.6 \pm 0.1 \text{ nm}$) demonstrates that the material has surface smoothing effect, which it is often used, in the devices. The measured variations in the adhesion forces may also partly be due to variations of the amount of water absorption within the range of relative humidities (31-46 %) associated with the current experiments.

Table 4.2: Summary of adhesion forces and energies (computed using DMT adhesion model)

Substrate coating	Tip Coating	Average force (nN)	Adhesion energy (J/m^2)
PEDOT:PSS	MEH-PPV:TiO ₂	81.93 ± 23.23	20.75 ± 4.55
Glass	MEH-PPV:TiO ₂	101.30 ± 26.58	16.03 ± 3.83
MEH-PPV	Aluminum	10.00 ± 1.20	0.80 ± 0.05
MEH-PPV:TiO ₂	Aluminum	31.00 ± 2.20	5.90 ± 1.70
ITO	MEH-PPV:TiO ₂	93.54 ± 28.72	5.15 ± 1.04
Glass	ITO	58.24 ± 14.33	9.31 ± 1.20
PEDOT:PSS	ITO	30.00 ± 6.70	1.70 ± 0.38

PEDOT:PSS	MEH-PPV	59.00 ± 6.00	15.00 ± 3.00
-----------	---------	--------------	--------------

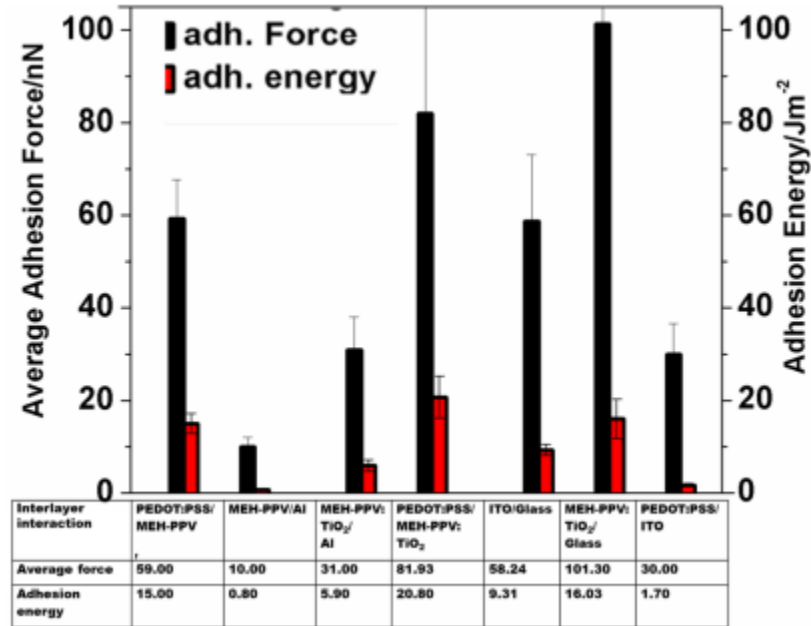


Figure 4.6: Summary of measured adhesion forces and energies.

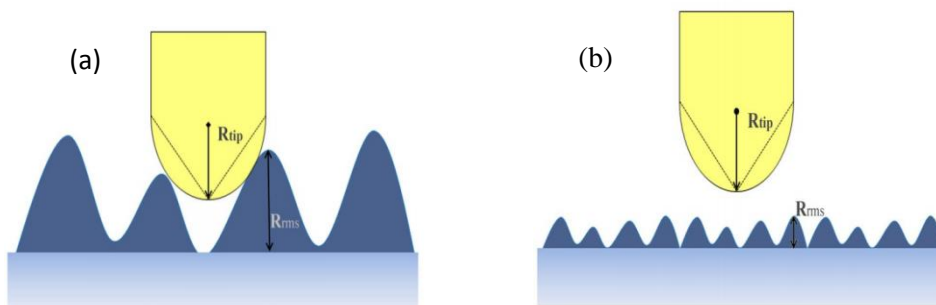


Figure 4.7: Scenarios for AFM Contacts between a Coated AFM Tip (yellow) and Substrate (blue) with: (a) High RMS Surface Roughness and (b) Low RMS Surface Roughness

4.5.4 Effects of Inorganic Nanoparticle Additives on Device Behavior

While there have been considerable improvements in device performance characteristics over the past decade, devices based exclusively on single-layer organic materials such as MEH:PPV face considerable challenges and may have nearly reached the limit of what they can achieve [26]. One way of improving the light/charge transport between and within layers in OPVs and OLEDs, is to introduce materials that can enhance charge transport and optical absorption. Within this context, the use of inorganic materials, such as titanium dioxide, has received recent attention [27].

The above materials are promising because they are affordable [27]. They also have good optical properties that can be further enhanced and tuned [28]. Furthermore, they can be structurally modified to self-assemble or form structures that facilitate directed charge transport [29]. Prior work has been done that shows theoretical solar cell efficiency gains using titanium dioxide nanorods or nanoporous layers [26]-[29], while OLEDs with titanium dioxide additives have been shown to demonstrate lower turn-on voltages and enhanced luminous efficiencies [23,27-29].

However, the addition or substitution of titanium dioxide particles, within the active layers themselves, can alter material properties, such as blend densities, charge conversion, and film elasticity. It is, therefore, important to determine the role of such material modifications on adhesive properties that can improve device integrity without compromising device efficiency and performance. There is, therefore, a need to consider the mechanical and electrical requirements in the design and application of TiO₂ nanoparticle enhancements for light emitting devices.

4.5.5 Inter- and Intra-facial Adhesion Energies for Hybrid Organic/Inorganic Light Emitting Devices

The above methods were used to determine the adhesion forces and adhesion energies of interfaces between layers that are relevant to HOILEDs. They were also used to study the effects of TiO₂ nanoparticles on adhesion. In the case of hybrid devices, the adhesion energies were determined at the interfaces between active layers and the underlying PEDOT: PSS and overlaying Aluminum cathode layer, as well as between the constituents of the active layers themselves. This was done to ascertain the direct effect of TiO₂ on interfacial adhesion – both through direct comparisons and by isolating each material's individual interactions.

Clear trends were observed for the adhesion between the TiO₂ additives in the active layer. The adhesion energies obtained for the HOILEDs are presented in Figure 4.6. Inter- and intra-facial adhesion with adjacent PEDOT: PSS and Aluminum layers are identified. To better understand the role of TiO₂ in affecting the relative adhesion of the film, film compositions and relative adhesion rankings are presented in Table 4.2.

The addition of TiO₂ can for example be shown to increase the adhesion with PEDOT: PSS from ~15 to ~21 J/m². Similarly, the adhesion with Aluminum increases from ~ 0.8 to ~ 5.9 J/m². This suggests that the presence of TiO₂ has a favorable effect on the active layer's adhesion.

TiO₂'s adhesion to Al is consistent with a metal-oxide bond. Meanwhile, the weak MEH: PPV-Al adhesion can be attributed to the twisted conformation of the MEH: PPV molecules, when dissolved in a non-aromatic solvent such as chloroform [53]. Since interactions are

associated with, Van der Waals forces and, hence, sensitive to surface contact area, the conformational mismatch results in poor packing and weak interfacial bonds. The reasons for these differences are not fully understood at the moment. There is, therefore, a need for further studies to provide molecular insights into the reasons for these differences. Nonetheless, it is clear that the intra-layer interactions help elucidate some of the preferential bonding tendencies that affect combined inter-layer adhesion phenomena.

4.5.6 Finite Element Simulations

In the finite element analysis of the bimaterial structures, similar trends for the variation of energy release rate ahead of crack tip with crack size were noticed. In figure 4.8, we present the results for the interfaces with weak, intermediate and strong interfacial adhesion. This corresponds to the Al/MEH-PPV, ITO/PEDOT:PSS and MEH-PPV:TiO₂/PEDOT:PSS interfaces respectively. Delamination between two surfaces occurs when the crack driving force (G) exceeds the critical interfacial adhesion energy (γ). In figure 4.8, we notice that the minimal crack length necessary to induce delamination decreases as the external load imposed on the system increases e. g. in figure 4.8a, a crack driving threshold, $G_c = 0.8 \text{ J/m}^2$ with a critical crack length of $6 \text{ }\mu\text{m}$ at a load of 20 N reduces to $3.2 \text{ }\mu\text{m}$ when the load is increased to 30 N . Interfacial interaction between surfaces may also increase the overall energy release rates compared to predictions from AFM calculations when higher mode mixities are present [18].

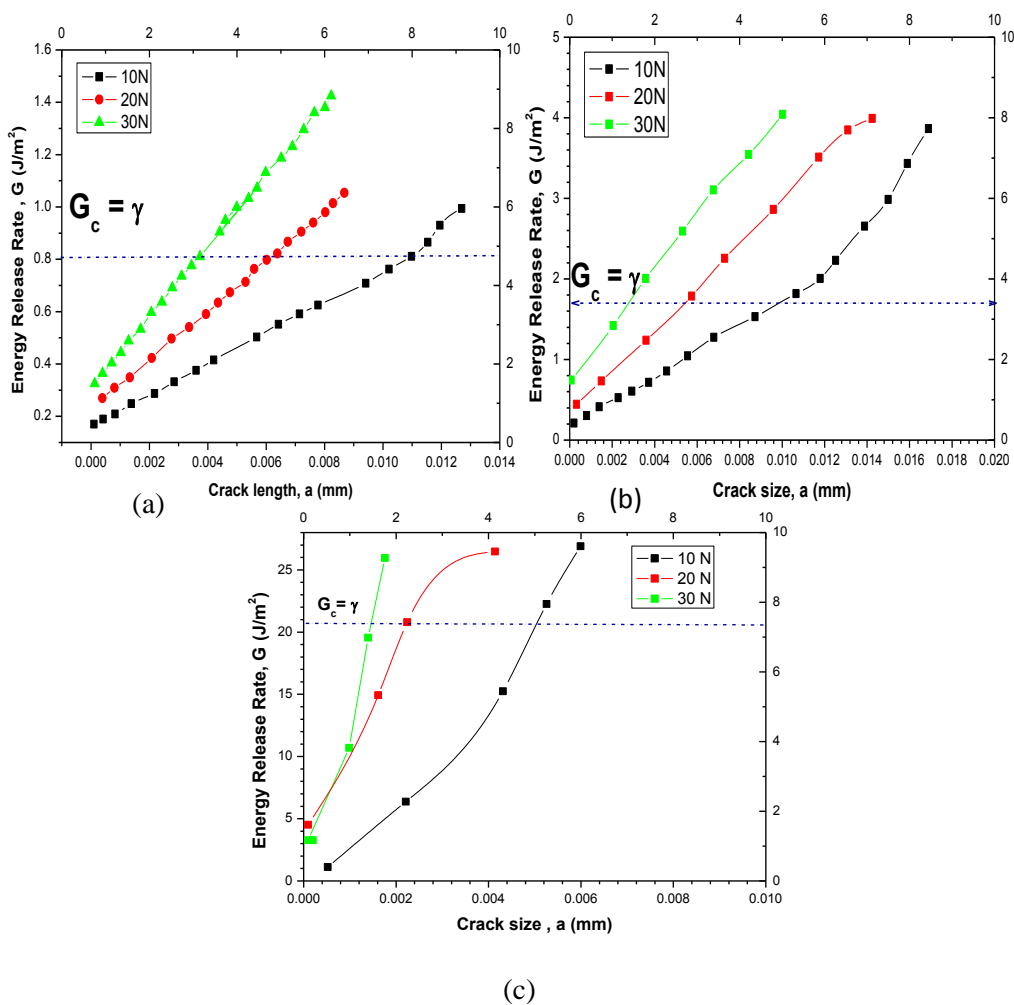


Figure 4.8: Dependence of energy release rate on crack size for (a) Al/MEH-PPV, (b) ITO/PEDOT:PSS and (c) MEH-PPV:TiO₂/PEDOT:PSS bimaterial systems subject to different loads. The critical point for interfacial delamination is shown.

4.5.7 Implications

The implications of the above results are quite significant. First, the AFM results has been shown to be a suitable method for ranking adhesion between different pairs of surfaces that are relevant to organic and hybrid organic/inorganic electronic structures. Such ranking is important in the selection of material pairs in LEDs where a wide range of materials

may be considered for possible applications. These applications include large-scale soft contact lamination processing techniques in which portions of the device are fabricated separately and pressure is applied to physically join the components together.

Strongly-adhering interfaces are thus good candidates for the contact layers, whereas weakly-adhering interfaces may be better for stamping interfaces at which the stamp is eventually lifted off and separated from the underlying layer. For those pairs with low adhesion energies, charge transport across the interfaces may be affected by the partial de-bonding that can occur between adjacent layers. The relatively high current densities in regions of partial contact may also lead to localized heating and oxidation phenomena that can degrade the performance of LEDs.

Conversely, in the cases with high adhesion energies, charge transport may be facilitated by the improved surface contact between the adjacent layers. Future work should, therefore, focus on large-scale surface contact at these interfaces to compare lamination-induced pressure effects on surface morphologies and strength of adhesion.

Coupled with studies of device performance and charge transport, a clear understanding of the geometry of contact between adjacent layers in LED could have a potential impact on the long-term robustness of interfaces in electronic structures. Such studies will also inform the validity of emerging trends to include inorganic materials to create hybrid structures with potential adhesion and device performance trade-offs.

Future work should also build on this exploration of the impact of adhesion energies on device performance through the relation of these AFM measurements with fracture mechanics estimates of the robustness of the interfaces. As in prior work on bi-material

pairs, [10], [30], the AFM measurements can be related to mode I fracture energies that provide the basis for the estimation of critical stresses or crack lengths in flexible or rigid organic electronic structures. This study can, therefore, be viewed through the lens of understanding large-area surface interactions and the need to measure interfacial fracture energies over a range of mode mixities that represent the range of stress states that can be encountered in real devices.

4.6 Summary and Concluding Remarks

In this chapter, an atomic force microscopy technique for the quantification of nano-scale adhesion between thin film interfaces in organic and hybrid organic/inorganic electronic devices is presented. The AFM technique is used for the characterization of the adhesion of a wide range of interfaces that are relevant to organic electronic structures. The study also considers the effects of TiO₂ nanoparticles on the adhesion within/ between the active layers.

The results show that TiO₂ nanoparticles enhance the adhesion between the active layers and hole injection layers of the different structures. The dependence of energy release rate on crack size is also studied for different bimaterial configurations. Such measurements can be used to improve existing device designs, while motivating large-scale processing methods, such as soft-contact lamination.

References

- [1] T. Tong, B. Babatope, S. Admassie, J. Meng, O. Akwogu, W. Akande, and W. O. Soboyejo, "Adhesion in organic electronic structures," *Journal of Applied Physics*, 106, 083708 (2009).
- [2] Robert J. Good, "Contact angle, wetting, and adhesion: a critical review", *Journal of Adhesion Science and Technology*, 6, 1269 (1992).

- [3] S. J. Bull and E.G. Berasetegul, “An overview of the potential of quantitative coating adhesion measurement by scratch testing”, *Tribology International*, 39, 2, 99-114 (2006).
- [4] K Kendall, “The adhesion and surface energy of elastic solids”, *J. Phys. D: Appl. Phys.*, 4, 1186 (1971)
- [5] A. A. Volinsky, N.R. Moody, and W.W. Gerberich, “Interfacial toughness measurements for thin films on substrates”, *Acta Materialia*, 50, 441 (2002).
- [6] Veeco Metrology: Force Imaging: Support Note No. 228, in Rev. E., (Digital Instruments, City, 1999).
- [7] Veeco Instruments Inc.: Improving the Accuracy of AFM Measurements: The Thermal Tune Solution, in Rev. AO, City, 2005).
- [8] B.V. Derjaguin, V.M. Muller and Y.P. Toporov: Effect of contact deformations on the adhesion of particles. *Progress in Surface Science* 45, 131 (1994).
- [9] K.L. Johnson, K. Kendall and A.D. Roberts: Surface Energy and the Contact of Elastic Solids. *Proceedings of the Royal Society of London. Series A, Mathematical and Physical Sciences* 324, 301 (1971).
- [10] N. Rahbar, K. Wolf, A. Orana, R. Fennimore, Z. Zong, J. Meng, G. Papandreou, C. Maryanoff and W.O. Soboyejo: Adhesion and interfacial fracture toughness between hard and soft materials. *Journal of Applied Physics* 104, 103533 (2008)
- [11] D. Maugis: Adhesion of spheres: The JKR-DMT transition using a dugdale model. *Journal of Colloid and Interface Science* 150, 243 (1992).
- [12] R.W. Carpick, D.F. Ogletree and M. Salmeron: A General Equation for Fitting Contact Area and Friction vs Load Measurements. *Journal of Colloid and Interface Science* 211, 395 (1999).
- [13] O. Piétrement and M. Troyon: General Equations Describing Elastic Indentation Depth and Normal Contact Stiffness versus Load. *Journal of Colloid and Interface Science* 226, 166 (2000).
- [14] J.H.C. Yoo, H. J. Gong, S. C. Baek, I. J. Lim, H. S. Chang, G. K. Chang, Y. C. Kim, H. J.: Preparation and Characterization of Polymer Light Emitting Diodes with ITO/PEDOT:PSS/MEH-PPV/LiF/A Structure. *Key Engineering Materials* 321/323, 1699 (2006).
- [15] X. Chen and M. Liu: Improvement of brightness and efficiency in organic light-emitting diodes using 1,3-bis(4-tert-butylphenyl-1,3,4-oxadiazoyl) phenylene as the hole buffer layer. *Displays* 28, 31 (2007).
- [16] X.D. Feng, D. Grozea and Z.H. Lu: Chemical Structure of MEH-PPV/LiF/Al Interface. *Materials Research Society Symposium Proceedings* 734, 175 (2003).
- [17] K.V. Wolf, Z. Zong, J. Meng, A. Orana, N. Rahbar, K.M. Balss, G. Papandreou, C.A. Maryanoff and W.O. Soboyejo: An investigation of adhesion in drug-eluting stent layers. *Journal of Biomedical Materials Research Part A* 87A, 272 (2008).
- [18] D.Y. Momodu, T. Tong, M.G. Zebaze Kana, A. V. Chioh, and W.O. Soboyejo : Adhesion and degradation of Organic and Hybrid Organic-Inorganic Light Emitting Devices. *Journal of Applied Physics* 115, 084504 (2014).
- [19] Benjamin Ohler : Cantilever Spring constant calibration using laser Doppler vibrometry. *Rev. Sci Instrum.* 78, 063701 (2007)
- [20] B. Wunderle and B. Michel, “Progress in reliability research in the micro and nano region”, *Microelectronics Reliability*, 46, 1685 (2006).
- [21] Y. Cao, C. Kim, S.R. Forrest, and W. Soboyejo, “Effects of dust particles and layer

- properties on organic electronic devices fabricated by stamping”, J. Appl. Phys. 98, 033713 (2005).
- [22] J. Du, T. Tong, W. Akande, A. Tsakiridou, and W. Soboyejo, “Pressure Effects on the Lamination of Organic Light-Emitting Diodes”, J. Disp. Technol. 9, 601–606 (2013).
- [23] W. Soboyejo, Mechanical Properties of Engineered Materials (CRC, New York, 2003).
- [24] D. Neerincx and T.J. Vink, “Depth profiling of thin ITO films by grazing incidence X-ray diffraction”, Thin Solid Films 278, 12–17 (1996).
- [25] J.Y. Kim, K. Lee, N.E. Coates, D. Moses, T.-Q. Nguyen, M. Dante and A.J. Heeger: Efficient Tandem Polymer Solar Cells Fabricated by All-Solution Processing. Science 317, 222 (2007).
- [26] M.T. Laugier: An Energy Approach to the Adhesion of Coatings Using the Scratch Test. Thin Solid Films 117, 243 (1984).
- [27] Mi-Hyae Park, Juo-Hao Li, Ankit Kumar, Gang Li and Yang Yang: Doping of the Metal Oxide Nanostructure and its influence in Organic Electronics. Advanced Functional Materials 19, 1241 (2009)
- [28] A.M. Hussain: Improved performance of polymer light-emitting diodes with nanocomposites. Appl. Phys. Lett. 94, 073306 (2009).
- [29] S.A. Haque, S. Koops, N. Tokmoldin, J.R. Durrant, J. Huang, D.D.C. Bradley and E. Palomares: A Multilayered Polymer Light-Emitting Diode Using a Nanocrystalline Metal-Oxide Film as a Charge-Injection Electrode. Advanced Materials 19, 683 (2007).
- [30] Z. Zong, Y. Cao, N. Rahbar and W.O. Soboyejo: Nano- and microscale adhesion energy measurement for Au--Au contacts in microswitch structures. Journal of Applied Physics 100, 104313 (2006).

Chapter 5

Stamping and Transfer Printing of Organic Light Emitting Diode Layers

5.1 Introduction

In the last two decades, intense research has been going on in the field of organic electronics especially for the development of cost-effective photovoltaic cells and light emitting devices [1],[2]. These research interests and developments have been greatly triggered by the potential for significant cost reductions compared to their amorphous or crystalline silicon counterparts [3]-[6]. Organic Light Emitting Devices (OLEDs) have become very popular in commercial applications due to their higher resolution and lower power consumption over traditional displays and solid state lighting devices [7]. Recent improvements in the efficiencies of organic photovoltaics (OPVs) from ~1 to ~10% [8] have brought them closer to commercialization. Such potentials imply that organic electronic devices may evolve to be widely utilized in both rural and urban applications [9]-[11].

A wide variety of methods are being used in the deposition of the layers relevant to the fabrication of OLEDs. Some of these methods used for depositing the active layers of the device include among others ink-jet processing, dip-coating, spin-coating and thermal vacuum evaporation. Thermal vacuum evaporation involves temperatures that may be detrimental to underlying organic layers. Soft-contact lamination is an alternative, cost effective technique for OLED layer deposition that can be employed in large area fabrication such as roll-to-roll

printing [12],[13]. Adhesion between adjacent layers is also important in soft-contact lamination procedure. Lamination has the potential to close up interfacial voids that impede charge injection and transport across device interfaces. Therefore, devices produced by the lamination of the active layers have potentials for improved performance and fabrication of large area displays and lighting systems relative to their spin-coated counterparts.

In this chapter, we present the results of experiments that show the transfer of poly[2-methoxy-5(2-ethylhexyloxy)-1,4 phenylenevinylene] (MEH-PPV), the active layer of the OLED structure on a glass substrate and also on poly(3,4-ethylenedioxythiophene)-poly(styrene sulfonate) (PEDOT:PSS), the hole injection layer material of the OLED structure. This transfer was done using an instron microtester. Atomic Force Microscopy (AFM) was used to image the deposited layers. The infusion of TiO_2 nanoparticles in the active layer of these OLED structures have been observed to yield devices with better performances [14]-[17]. We also used this technique to study the deposition of thin films of MEH-PPV solution mixed with TiO_2 nanoparticles. Finite element simulations are also used to study the effects of surface contacts and interfacial fracture during the contact and pull-off stages of soft-contact lamination. The results are used to provide insights into the conditions required for successful, unsuccessful or partial transfer of the thin film layer during soft lamination processes.

5.2 Experimental Methods

5.2.1 Spin-Coating of Polymer Layers

Soda lime glass substrates of dimensions 25 mm x 25 mm were cleaned using isopropyl alcohol and decon 90 before being placed in an ultrasonic bath for 30 minutes. The substrates were then blow-dried using pure nitrogen gas. Baytron P VP Al-4083 PEDOT:PSS (Heraeus Clevios, Hanau, Germany) was filtered through a 0.2 μm filter for 1 minute at a rate of 3000 revolutions per minute (rpm) to further improve the smoothness and uniformity.

The filtered solution was then spin-coated onto the cleaned glass substrate at 1500 rpm for 15 s. The samples were then cured at 120°C for 5 minutes to remove any residual moisture. Poly[2-methoxy-5-(2'-ethyl-hexyloxy)-1,4-phenylene vinylene] (MEH:PPV) powder (Aldrich, St. Louis, MO), with molecular weight between 150,000 and 250,000, which is used to form the emissive layer was dissolved in chloroform to produce a 5 mg/ml solution. After stirring the resulting solution for 6 hours, it was filtered and then spin-coated onto the hole-injection layer at 800 rpm for 60 s. Some samples were prepared by coating MEH-PPV on the glass substrates directly.

MEH: PPV: TiO₂ which constitutes the active layer for Hybrid Organic-Inorganic Light Emitting Diodes was prepared by mixing 15 mg of MEH: PPV in 2 mL of chloroform at room temperature for 6 hours. 5 mg of TiO₂ was sonicated in 2 mL of chloroform for 45 minutes and then the two mixtures were combined and sonicated for an additional 30 minutes. This was also spin-coated on glass substrates and PEDOT:PSS-coated glass substrates using the procedure described above for spin-coating MEH:PPV without TiO₂.

5.2.2 Preparation of PDMS anvil

Polydimethylsiloxane (PDMS) was used to prepare the anvil. The PDMS mixture (Sylgard 184, Dow Corning) was prepared by mixing a pre-polymer base with a curing agent. This was done in a 10:1 ratio (by weight) in a petri dish. The resulting mixture was then cured in a vacuum oven at 80 °C for 2 hrs. The cured PDMS anvil was then removed from the petri dish. On top of the PDMS anvil, a layer of (tridecafluoro-1,1,2,2,-tetrahydrooctyl)-trichlorosilane (FOTCS) (Gelelest Inc., Morrisville, PA) was deposited as a self-assembled monolayer (SAM) that reduces the adhesion between the anvil and any adjacent layer. The SAM was deposited by vapor deposition. This was done in a desiccator at room temperature for 6 hrs.

5.2.3 Lamination of MEH-PPV layers

The coated PDMS anvil was then dip-coated in the MEH-PPV solution before being brought into contact with the glass substrate using an Instron mechanical tester (Instron, Norwood, MA). This was used to apply a force between 200 N to 500 N at room temperature. Subsequently, the force was then removed from the substrate by lifting up the anvil. It is important to note here that the SAM reduces the adhesion between the anvil and the device. This ensures that the anvil and the MEH-PPV layer to be transferred are separated during the lifting stages. Some layers of MEH-PPV were transferred onto glass and others transferred onto PEDOT:PSS-coated glass.

In the lamination process, the anvil was mounted on a fixture in the Instron Microtesting machine as shown in Fig. 5.1. The machine was interfaced with a software/ wave-maker, using a three-block program to track the experiment progress. The test parameters which include the

force, time of press or hold and the rate of pull-off after deposition were all set on wave-maker software. The force range used in the experiment was between 100 and 500N, while the holding time was between 120 and 240 seconds. A 0.1mm/sec pull-off rate was used in all the experiments. The first block of the program involved push down, while, the second block involved a hold, while the third block was associated with pull-off. A complete transfer of the active layer material is shown in Fig. 5.2.



Figure 5.1 : Instron 5875 microtester setup.

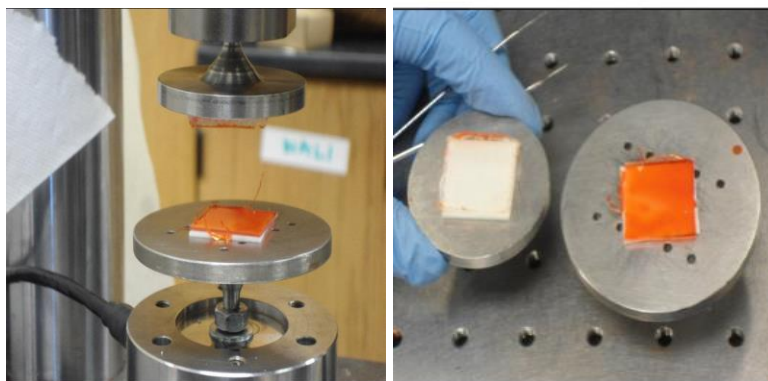


Figure 5.2: Complete Transfer of MEH:PPV on glass.

5.3 Atomic Force Microscopy Measurements

Etched silicon Contact AFM cantilever probes were purchased from Veeco Instruments (Woodbury, NY). These uncoated cantilevers were used to determine the surface morphologies of the different samples prepared earlier.

Since the AFM measurements are highly sensitive to surface roughness, the tip radii and substrate roughnesses were measured before each experiment. Selected tip radii were measured before and after AFM characterization in order to take into account potential tip deformation in the course of the experiments. Using the Dimension AFM under tapping mode, 8 height and phase images of each layer were used to measure the root mean squared (rms) surface roughnesses within areas ranging from $1 \times 1 \mu\text{m}$ to $10 \times 10 \mu\text{m}$ (Tables 5.2 and 5.3).

5.4 Finite Element Simulations

In order to study the mechanisms that govern transfer printing of a thin film layer on a substrate, we use a fracture mechanics approach and finite element analysis (FEA). The finite element code, ABAQUS Vs 6.12 is used in the modeling and simulations. In this work, we model a system made of three (3) layers, a transfer substrate (TS), a device substrate (DS) and a printable layer (PL). An example of a printable layer is the active layer of our OLED, MEH-PPV, whose transfer on a rigid substrate is described in the experiments in section 5.2.3. A typical trilayer structure used in our simulations is shown in Fig. 5.3.

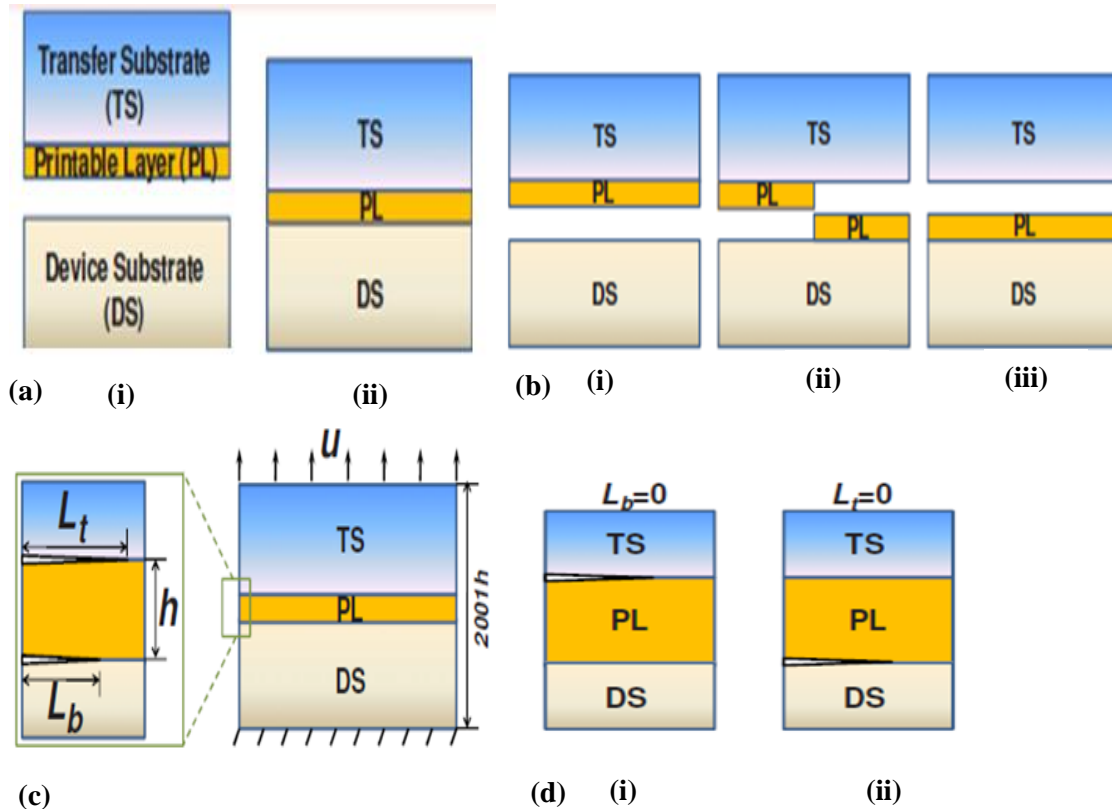


Figure 5.3: Schematic of transfer printing process with two (2) steps: (a) a printable layer (PL) sandwiched between a transfer substrate (TS) and a device substrate (DS); (b) TS lifted off; b(i) Unsuccessful transfer; b(ii) Partial transfer; b(iii) Successful transfer; (c) Effect of initial interfacial defects on the competing delamination in the trilayer structure of transfer printing. Interfacial edge cracks of initial lengths L_t and L_b , initiated at the top and bottom interfaces respectively; (d) Two limiting cases for transfer printing; d(i) Unfavorable situation for printing; d(ii) Favorable setup for printing.

Since our primary interest was in the interfacial cracking of the two interfaces (top and bottom) in the three-layer structure, the initial fracture mechanics models considered both edge and non-edge cracked geometries[22]. However, since the crack driving forces for the edge cracks were generally greater than those of center cracks of the same size, the modeling efforts focused largely on edge cracks, embedded in the bulk.

During the lift-off process, delamination can occur at the top and bottom interfaces. The driving force of the crack along the top interface is given by the energy release rate, G_t , at the top

interface crack tip. Likewise, the driving force for crack growth along the bottom interface is characterized by the energy release rate, G_b , at the bottom interface crack tip. Delamination occurs along the top interface, when G_t is greater than the interfacial adhesion of this interface, G_t^c . Similarly, delamination at the bottom interface occurs when G_b is greater than the interfacial adhesion of this interface, $\varepsilon = \frac{u}{2001h}$

In practice, the lift-off procedure is displacement-controlled, implying that the differential driving force for crack growth along the two interfaces is more crucial than their absolute values. The following condition must be satisfied for the top interfacial crack to grow and start delamination at the top interface:

$$\left(\frac{G_t}{G_b} \right) > \left(\frac{G_t^c}{G_b^c} \right) \quad (1)$$

Also,

$$\frac{G_t}{G_b} < \frac{G_t^c}{G_b^c} \quad (2)$$

for the bottom interfacial crack to evolve and start delamination at the bottom interface. The quantities $\left(\frac{G_t}{G_b} \right)$ and $\left(\frac{G_t^c}{G_b^c} \right)$, respectively, represent the external driving force for delamination and internal material resistance to delamination. In describing the integrity and quality of the printing process, we make use of equations (1) and (2). If equation (1) is satisfied, then the transfer will be successful. Equation (2) will represent an unsuccessful transfer process. Partial transfer can occur when a steady delamination along one interface results in fracture of the

printable layer. The PL fractures due to its own initial imperfections such as microvoids. This can give rise to delamination of the other interface.

In the finite element model described in this study, we consider the transfer of a thin layer of a printable layer under plane strain conditions. The thickness of the PL is h (e. g. 100 nm for our typical MEH-PPV active layer). Both the TS and DS have thickness of $1000h$ and length of $1000h$ (e.g. 100 μm in this study). The length of the initial cracks introduced at the top and bottom interfaces are L_t and L_b respectively. In the simulations, we varied L_t and L_b to study its impact on the strain energy release rate. For the boundary conditions setup in the model, we fixed the bottom edge of the DS by setting its vertical displacement to zero. We also applied a continuity boundary condition on the outer left and right edges of the trilayer structure to prevent any lateral displacement. The applied strain, ε , in the structure is given by:

$$\varepsilon = \frac{u}{2001h} \quad (3)$$

where, u is the applied displacement as a result of the displacement controlled loading. The structure is meshed with four-node quadrilateral plane strain elements. The mesh is made denser in the region near the tip of the cracks. The layers are modeled as isotropic elastic solids, which can be characterized by their Young's modulus, E and Poisson's ratio, ν . The mechanical properties of the trilayer materials used in the simulations are displayed in Table 5.1. This is obtained from prior work [18,19] and other sources in the literature [20-23]. The contour integral approach in ABAQUS is used to calculate the energy release rate of the interfacial cracks.

Table 5.1: Mechanical properties of trilayer materials used in simulations.

Transfer Substrate (TS)			Printable Layer (PL)			Device Substrate (DS)		
Material	E(GPa)	ν	Material	E(GPa)	ν	Material	E(GPa)	ν
PDMS	0.003	0.48	MEH-PPV	11.5	0.3	Glass	69	0.3
						PET	3	0.37
						PDMS	0.1	0.5
						PDMS	0.003	0.48

5.5 Results and Discussion

5.5.1 Spin-Coated versus Laminated Polymer Layers

The different layers deposited exhibited a wide range of surface morphologies. Differences were visibly apparent from the height and phase scans and quantified by the rms roughness results (Tables 5.2 and 5.3).

Table 5.2: Surface roughness of laminated layers

Layer	Rms roughness(nm)
MEH-PPV/GLASS	2.389
MEH-PPV/PEDOT:PSS	4.196
MEH-PPV+TiO ₂ /GLASS	5.273

MEH-	6.520
PPV+TiO ₂ /PEDOT:PSS	

Table 5.3: Surface roughness of spin-coated layers

Layer	Rms roughness(nm)
MEH-PPV/GLASS	8.859
MEH-PPV/PEDOT:PSS	10.345
MEH-PPV/GLASS	12.691
MEH-PPV/PEDOT:PSS	16.132

The layers deposited by lamination were highly-uniform compared to those deposited by spin-coating for both MEH:PPV on glass and MEH:PPV on PEDOT:PSS/glass samples and rms roughness values were within reasonable limits when compared to the layer thicknesses. Nano-scale roughnesses can dominate interactions between asperities on layer surfaces. Fig. 5.4 represents the force-displacement characteristic during the 3-block program that represents loading, holding and lifting up during the lamination process.



Figure 5.4: Force displacement curves from wave maker software during loading, holding and lifting up process.

AFM images of laminated MEH-PPV and MEH-PPV+TiO₂ on glass are respectively shown in Figures 5.5 and 5.6.

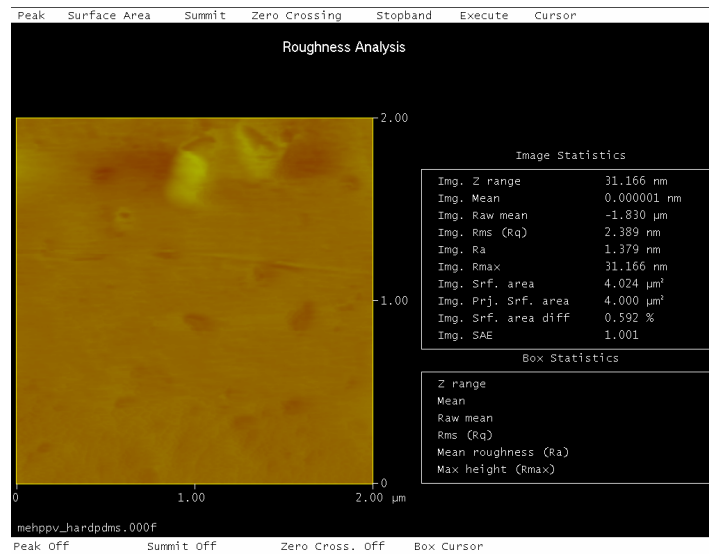


Figure 5.5: Surface Morphology of laminated MEH-PPV layer on glass.

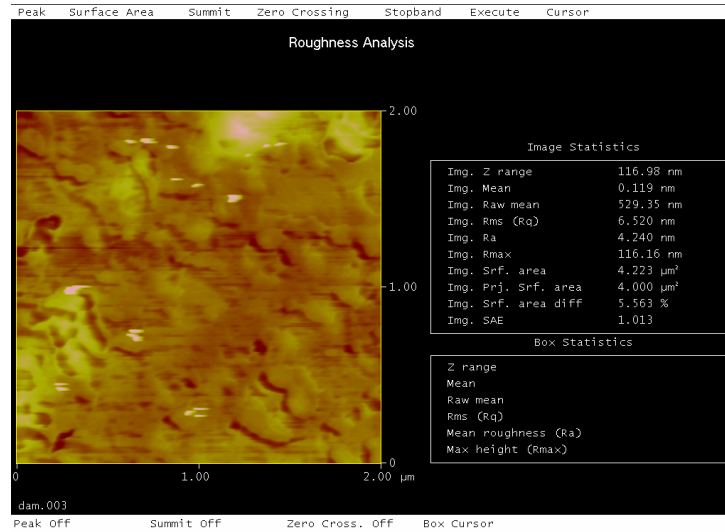


Figure 5.6: Surface Morphology of laminated MEH-PPV + TiO₂ layer on glass.

Fig. 5.7 of the scanning electron microscope (SEM) images, shows a visible difference between the surface morphology of layers deposited by lamination versus those done by spin-coating. These images show that the introduction of TiO₂ particles in the MEH-PPV layer increases the roughness of the thin film as expected. It has been shown that devices with TiO₂ incorporated into the active layer have higher efficiencies [14]. There is therefore a trade-off for the roughness in preference for device performance.

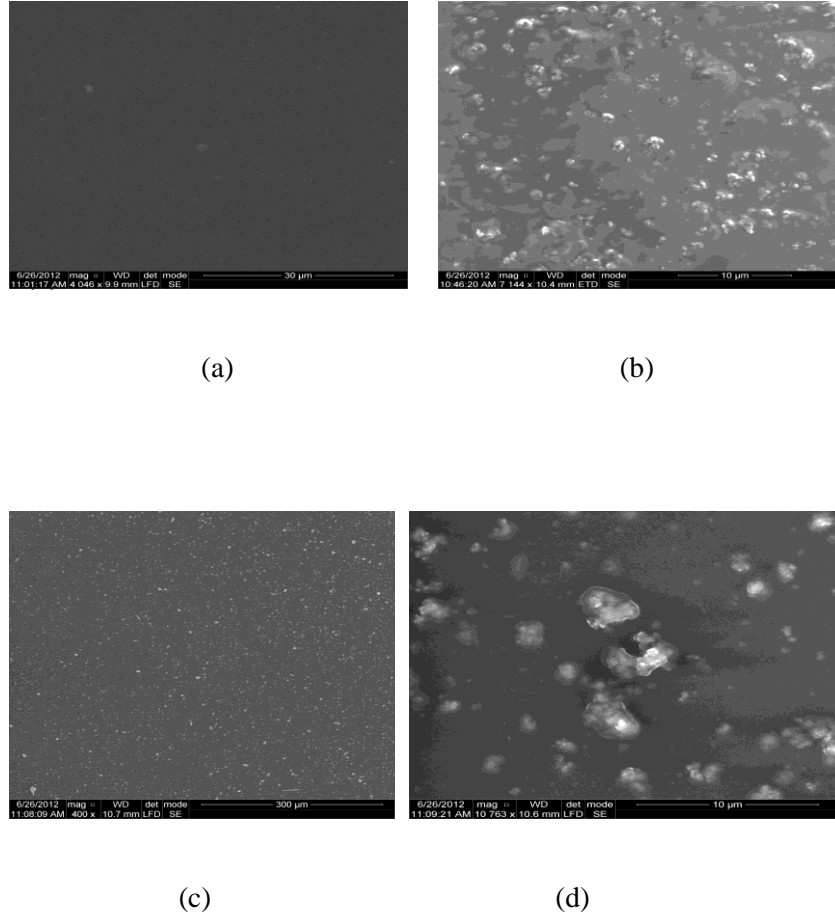


Fig 5.7: SEM images of (a) laminated MEH-PPV on glass, (b) laminated MEH-PPV+TiO₂ on glass, (c) spin-coated MEH-PPV on glass and (d) spin-coated MEH-PPV+TiO₂ on glass

5.5.2 Finite Element Simulations

For different device substrate stiffnesses, the variation of the energy release rate with top interfacial crack size (L_t) was studied or bottom interfacial crack size (L_b). Figure 5.8 shows plots of the normalized energy release rate ($G_t/E_{PL}\epsilon^2h$ or $G_b/E_{PL}\epsilon^2h$) versus normalized

interfacial crack sizes (L_t/h or L_b/h) for different device substrate stiffnesses (ranging from compliant to stiff substrates).

There are two limiting cases considered here. The first one is when $L_t/h = 0$, representing a situation where there is no delamination at the top interface. This is generally desirable since it translates into a complete transfer of the printable layer onto the device substrate. The second case is when $L_b/h = 0$, representing a situation where there is no delamination at the bottom interface. This is generally undesirable since it translates into a no transfer of the printable layer onto the device substrate.

In these two limiting cases, it was noticed that the energy release rate increases monotonically with crack size and saturates when the crack size reaches a value, several hundred times greater than the thickness of the printable layer. It was also noticed that the energy release rate increases significantly with device substrate stiffness. This is because for a very compliant device substrate, a large amount of the applied strain is accommodated by the bulk material than the interface. For cracks of a particular length, the strain energy release rate for the bottom interface is smaller than that for the top interface. This difference reduces as the device stiffness increases. This can still be attributed to the fact that the bulk material of the compliant substrate accommodates much of the applied strain.

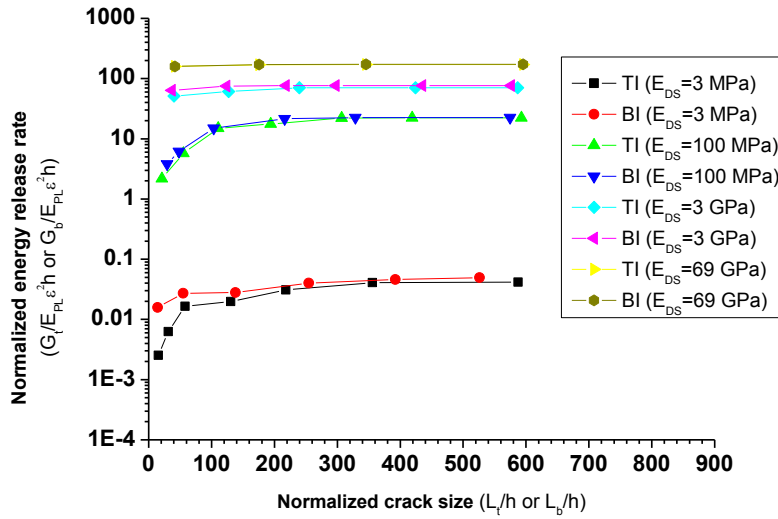


Figure 5.8: Dependence of energy release rate on initial interfacial crack size at the top interface (TI) and bottom interface (BI) of a typical trilayer structure relevant in organic electronics. This is done for device substrate with different stiffness values (E_{DS}).

The next case considered is the intermediate case. That is, when there is competing delamination in which the printable layer can delaminate from both interfaces. Since the energy release rate plots in Figure 5.8 saturates at values of L_t/h and L_b/h greater than 40, it is more relevant to study competing delamination for values less than 40. For different device substrate stiffness values, we examine the evolution of the strain energy release rate of a top interfacial crack with the bottom interfacial crack size and a particular top interfacial crack size (Figure 5.9).

Three top interfacial crack sizes ($L_t = 5h, 20h$ and $40h$) are considered for each device substrate. A total of three device substrate stiffness values are considered, $E_{DS} = 3$ MPa (Figure 5.9a), $E_{DS} = 100$ MPa (Figure 5.9b) and $E_{DS} = 69$ GPa (Figure 5.9c). This is representative of typical compliant and stiff substrates used in practical organic light emitting

devices. The energy release rate of the top interfacial crack generally decreases with increase in bottom interfacial crack size. As the device substrate stiffness increases, the energy release rate increases for a particular bottom and top interfacial crack sizes.

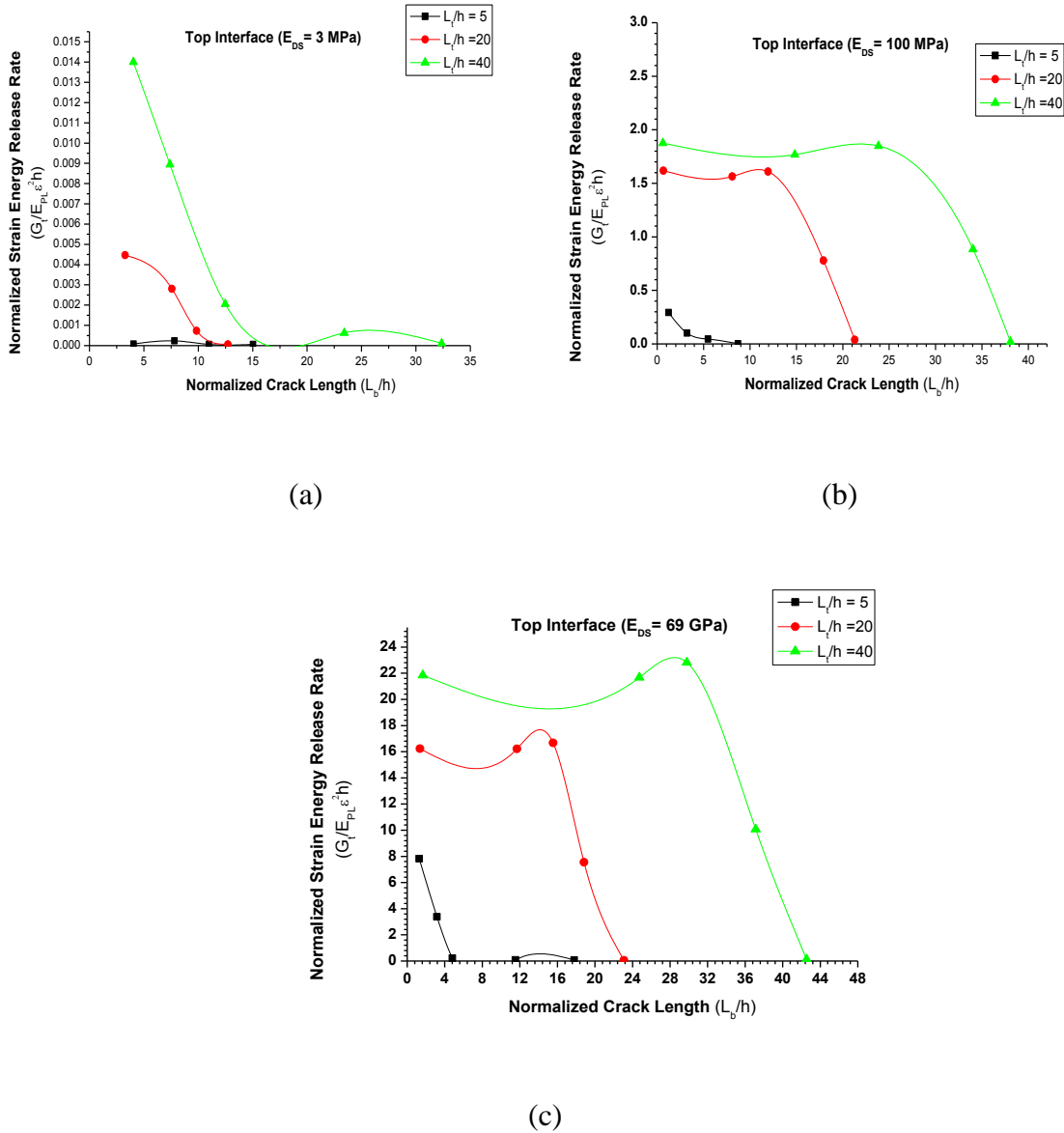
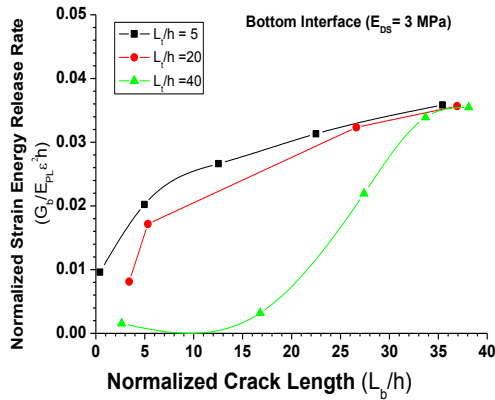


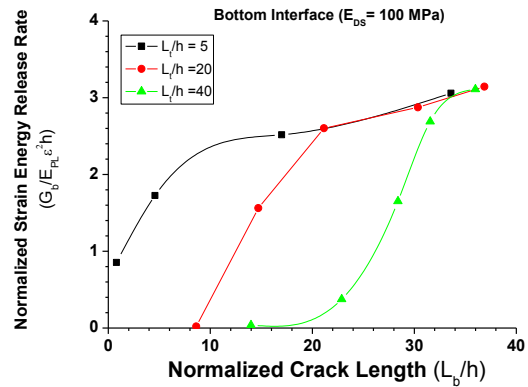
Figure 5.9: Dependence of energy release rate of top interfacial crack on initial interfacial crack size of bottom interface (BI) in a typical trilayer structure relevant in organic electronics. This is studied for device substrate with different stiffness values (E_{DS}) and top

initial interfacial crack sizes; (a) For a compliant device substrate of stiffness, 3 MPa; (b) For a device substrate with intermediate stiffness of, 100 MPa, and (c) For a stiff device substrate with stiffness, 69 GPa.

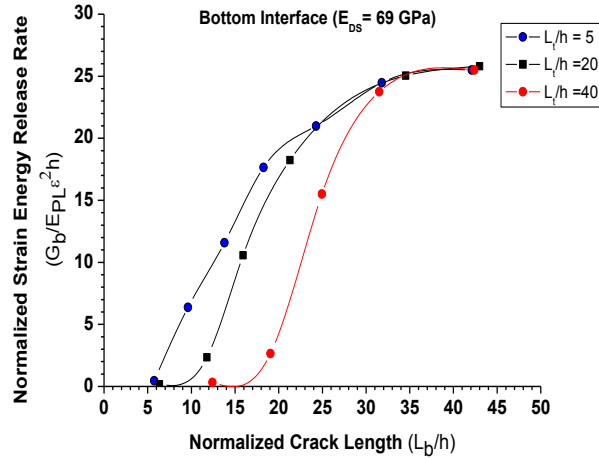
For different device substrate stiffness values, we examine the variation of the strain energy release rate of a bottom interfacial crack with the bottom interfacial crack size and a particular top interfacial crack size (Figure 5.10). Three top interfacial crack sizes ($L_t = 5h$, $20h$ and $40h$) are considered for each device substrate. A total of three device substrate stiffness values are considered, $E_{DS} = 3$ MPa (Figure 5.10a), $E_{DS} = 100$ MPa (Figure 5.10b) and $E_{DS} = 69$ GPa (Figure 5.10c). The energy release rate of the bottom interfacial crack generally increases with increase in bottom interfacial crack size. As the device substrate stiffness increases, the energy release rate increases for a particular bottom and top interfacial crack sizes.



(a)



(b)



(c)

Figure 5.10: Dependence of energy release rate of bottom interfacial crack on initial interfacial crack size of bottom interface (BI) in a typical trilayer structure relevant in organic electronics. This is studied for device substrate with different stiffness values (E_{DS}) and top initial interfacial crack sizes; (a) For a compliant device substrate of stiffness, 3 MPa; (b) For a device substrate with intermediate stiffness of, 100 MPa, and (c) For a stiff device substrate with stiffness, 69 GPa.

Figure 5.11 shows a variation of the differential driving force for interface crack growth along the top and bottom interfaces with crack size of the bottom interface, for a top interfacial crack of 20h. The study is carried out for different device substrates with stiffnesses of 3 MPa, 100 MPa, 3 GPa and 69 GPa. The line (when this driving force is unity)

corresponds to a case of differential interfacial adhesion, $\left(\frac{G_t^c}{G_b^c}\right)$, being unity as well. Below

this line, we will have unsuccessful transfer of the printable layer while above it, we will have a successful transfer of the layer. Clearly, it is seen that transferring on a compliant

substrate is challenging. As the device substrate stiffness increases, the critical bottom interfacial crack size beyond which successful transfer is possible increases.

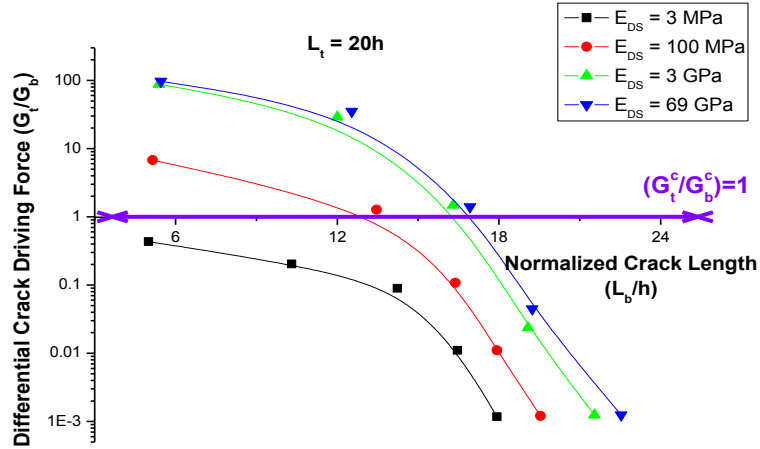


Figure 5.11: Dependence of the differential driving force for interfacial crack growth on initial interfacial crack size of bottom interface (BI) in a typical trilayer structure relevant in organic electronics. This is studied for device substrate with different stiffness values (E_{DS}). The top initial interfacial crack size here is $L_t = 20h$.

5.5.3 Implications

The above results show that layers of the active layer, produced by soft-contact lamination, have lower values of average roughness. This is very important because OLEDs are multilayered structures; the roughness of interfaces can impede the performance of the devices. Charge injection and transport are crucial. Interfacial and surface roughness can limit these processes. From the results of the simulations, we can determine the quality of the transfer printing not only by the relative interfacial adhesion, (G_t^c/G_b^c) in the tri-layer

structure, but also by the defects (e.g. cracks) along the two interfaces. This means that differential interfacial adhesion and defects both play a critical role in transfer printing.

Transfer printing onto a compliant substrate is more challenging than only a stiff device substrate. On a stiff device substrate, the process is dominated by the interfacial defects and is less sensitive to differential adhesion. On the other hand, transfer onto a compliant substrate, although challenging can be improved by tailoring the differential interfacial adhesion. In general, controlling the interfacial defects offers new methods to improve transfer printing quality and integrity which remains highly unexplored. Hence, the results obtained from this study provide us with a quantitative guidance on the role of interfacial defects in the control of transfer printing processes.

5.6 Summary and Concluding Remarks

In this chapter, we present experimental results that show the complete transfer of thin-films of the active layer material, MEH-PPV of OLEDs using soft-contact lamination. Spin-coated layers were used as controls. The lower roughness values obtained for laminated layers, both MEH-PPV and MEH-PPV infused with TiO₂ nanoparticles is an indication that such a procedure can be employed in large area display and lighting systems fabrication with the device performance not compromised.

Although the results of the surface layer roughness achieved so far are quite reasonable compared to earlier results from spin-coating, further enhancement of this technique is needed to optimize the layer properties. This optimization could be achieved by possibly tuning the 3-stage program parameters to have better detachment from the PDMS stamp.

Surface treatment and/or modification of the PDMS stamp are needed to improve the detachment conditions.

Finite element simulations are also needed to provide process design guidelines for the design of the role of interfacial defects in the contact transfer printing process.

References

- [1] C.W. Tang: An overview of organic electroluminescent materials and devices. *Journal of the Society for Information Display* 5, 11 (1997).
- [2] H. Hoppe and N.S. Sariciftci: Organic solar cells: An overview. *Journal of Materials Research* 19, 1924 (2004).
- [3] G. Malliaras and R. Friend: An Organic Electronics Primer. *Physics Today* 58, 53 (2005).
- [4] U. Mitschke and P. Bäuerle: The electroluminescence of organic materials. *Journal of Material Chemistry* 10, 1471(2000).
- [5] C.W. Tang and S.A. VanSlyke: Organic electroluminescent diodes. *Applied Physics Letters* 51, 913 (1987).
- [6] S. Forrest, P. Burrows and M. Thompson: The dawn of organic electronics. *IEEE Spectr.*37, 29 (2000).
- [7] S.R. Forrest: The road to high efficiency organic light emitting devices. *Organic Electronics* 4, 45, (2003).
- [8] Heliatek: Heliatek achieves new world record for organic solar cells with certified 9.8 % cell efficiency(2011).
- [9] D.F. Barnes and W.M. Floor: Rural Energy in Developing Countries: A Challenge for Economic Development 1. *Annual Review of Energy and the Environment* 21, 497 (1996).
- [10] E. Martinot, A. Chaurey, D. Lew, J.R. Moreira and N. Wamukonya: Renewable Energy Markets in Developing Countries. *Annual Review of Energy and the Environment* 27, 309 (2002).

- [11] S.R.F. B. W. D'Andrade: White Organic Light- Emitting Devices for Solid-State Lighting, *Advanced Materials* 16, 1585(2004).
- [12] J.W.P. Hsu: Soft lithography contacts to organics. *Materials Today* 8, 42 (2005).
- [13] T.-W. Lee, J. Zaumseil, Z. Bao, J.W.P. Hsu and J.A. Rogers: Organic light-emitting diodes formed by soft contact lamination. *Proceedings of the National Academy of Sciences of the United States of America* 101,429 (2004).
- [14] A.M. Hussain: Improved performance of polymer light-emitting diodes with nanocomposites. *Appl. Phys. Lett.* 94, 073306 (2009).
- [15] S.A. Haque, S. Koops, N. Tokmoldin, J.R. Durrant, J. Huang, D.D.C. Bradley and E. Palomares: A Multilayered Polymer Light-Emitting Diode Using a Nanocrystalline Metal-Oxide Film as a Charge-Injection Electrode. *Advanced Materials* 19, 683(2007).
- [16] K. Morii: Encapsulation-free hybrid organic-inorganic light-emitting diodes. *Appl. Phys. Lett.* 89, 183510 (2006).
- [17] Mi-Hyae Park, Juo-Hao Li, Ankit Kumar, Gang Li and Yang Yang: Doping of the Metal Oxide Nanostructure and its influence in Organic Electronics. *Advanced Functional Materials* 19, 1241 (2009).
- [18] Y. Cao, C. Kim, S.R. Forrest, and W. Soboyejo, "Effects of dust particles and layer properties on organic electronic devices fabricated by stamping", *J. Appl. Phys.* 98, 033713 (2005).
- [19] J. Du, T. Tong, W. Akande, A. Tsakiridou, and W. Soboyejo, "Pressure Effects on the Lamination of Organic Light-Emitting Diodes", *J. Disp. Technol.* 9, 601–606 (2013).
- [20] A. Bietsch and B. Michel, "Conformal contact and pattern stability of stamps used for soft lithography", *J. Appl. Phys.* 88, 4310 (2000).
- [21] N. Bowden, S. Brittain, A.G. Evans, J.W. Hutchinson, and G.M. Whitesides, "Spontaneous

formation of ordered structures in thin films of metals supported on an elastomeric polymer”, *Nature* 393, 146 (1998).

[22] W. Soboyejo, *Mechanical Properties of Engineered Materials* (CRC, New York, 2003).

[23] D. Neerincx and T.J. Vink, “Depth profiling of thin ITO films by grazing incidence X-ray diffraction”, *Thin Solid Films* 278, 12–17 (1996).

Chapter 6

Encapsulation of Organic Light Emitting

Diodes and Red-Shift of its

Electroluminescence Spectra

6.1 Introduction

In the years since the discovery of electroluminescence in small molecule OLEDs [1] and similar fluorescent emission in conjugated polymers [2], there has been increased interest in the commercial use of organic electroluminescent devices in displays and lighting applications [3-5]. However, environmental interactions with the organic active layers and low work-function metals that are used for the fabrication of these devices have limited their potential applications within moisture and oxygen rich environments. Such interactions have stimulated some interest in the development of low cost encapsulation methods that can reduce the impact of oxygen and moisture on the electrical performance of OLEDs [6-8].

Initially, epoxy-glass seals [6] were used to encapsulate organic electronic devices.

Unfortunately, however, the UV-curable epoxies used were proprietary and expensive. Apart from their cost, these resins can be detrimental to the device if they leach into or come in contact with the active organic layers during processing, operation or storage. Furthermore, the

glass lids add considerable weight to the devices and thus remove the light-weight appeal of organic electronics.

Recently, a number of approaches have been explored for the engineering of improved lifetimes in organic light emitting diodes (OLEDs). Most of these methods use alternating inorganic, organic or inorganic-organic multi-layers [9-11]. Al-Li and high density polyethylene (HDPE) multilayer barriers have been used to successfully encapsulate OLEDs on glass [9]. Lamination procedures have also been used to demonstrate reduced device sensitivity to ambient conditions [10]. These encapsulation procedures, in general, have been shown to efficiently handle a majority of extrinsic degradation mechanisms (dark spots, bubbles) that plague OLEDs due to their interactions with oxygen and moisture in the operating environment [12]. An example of this approach can be seen in the recent work by Mandlik et al [11] which has shown that plasma deposited SiO_xC_y hybrid layers can be used to extend the lifetimes of encapsulated OLEDs to about 7500 h. Although this method successfully improves the lifetimes of these devices, the required vacuum deposition method is complex and not suited for low-cost applications.

In order to enhance the appeal of organic electronics as low-cost, lightweight devices, suitable for flexible applications, more accessible and conformable encapsulation schemes need to be explored. To this end, a number of simple encapsulation schemes have been developed to meet these criteria [13-15]. These techniques involve the use of solution processed polymer barriers such as Cytop [13,14] or commercial, non-proprietary laboratory processes [15] to achieve reasonable device stability. In particular, these techniques enable greater device stability in oxygen and moisture rich environments, while achieving the criteria necessary for flexible,

lightweight and low cost applications. The use of polymer encapsulating layers also presents the opportunity for added functionality. This subtle, yet powerful advantage of polymer barrier layers has been recently employed in tuning the threshold voltage of organic field effect transistors [16].

Poly (dimethylsiloxane) (PDMS) has been widely used within the micro-fluidics community for creating micro scale channels for lab-on-chip applications. PDMS has also been used to add functionality and packaging to OLED-based microchip fluorescence applications [17]. Recently, Han et al. [18] have also successfully employed PDMS as a polymer barrier for encapsulating OLEDs on flexible substrates. The barrier and conformal properties were achieved by using the inherent mechanical flexibility and hydrophobic properties of PDMS [19, 20].

The prior PDMS encapsulation procedure in [18] included e-beam evaporation of SiO₂ as an adhesion promoting layer onto the surface of the OLED in addition to intermittent curing and peeling steps to create a composite (partially and fully cured PDMS) encapsulation plate. Thus, although PDMS is cheap and readily available, there are a number of steps required for the above encapsulation scheme that reduces its appeal as a parallel process suitable for large scale implementation.

Consequently, the current work investigates a parallel, inexpensive, polymer (PDMS) - based stamping technique for the encapsulation of organic electronic devices. The scalable technique is shown to have improved mechanical robustness (interfacial fracture toughness) and resistance to oxygen and moisture in the environment.

6.2 Experimental Procedures

6.2.1 Organic Light Emitting Diode Fabrication

Single layer organic light emitting diodes with the traditional sandwich structures (Figure 6.1) were fabricated under ambient conditions. Poly (2- methoxy-5-[2-ethylhexyloxy] 1,4-p-phenylenevinylene) (MEH-PPV; Aldrich, St. Louis, MO) with molecular weight between 150,000 and 250,000 was dissolved in chloroform to give a 0.5% solution by weight. The resulting solution was spin-coated onto patterned ITO substrates (Delta technologies, Stillwater, MN; $R_s = 4-8$ ohms) to give thicknesses between 200 and 250 nm, as measured using a KLA Tencor P15 Surface Profiler (KLA-Tencor, Milpitas, CA).

Prior to spin coating, the ITO substrates were cleaned, respectively, by sonication in acetone, trichloroethylene and isopropanol for 10 minutes. The substrates were further cleaned in a UVOCS ultraviolet/Ozone cleaner for 10 minutes before use (UVOCS, Lansdale, PA).

Aluminum films with thicknesses between 100 and 150 nm were thermally deposited onto the spin-coated substrates using an Edwards E306A thermal evaporator operated at a vacuum of 10^{-7} Torr .The device area was defined using conventional shadow masks. This resulted in devices with an area of 0.05 cm^2 .

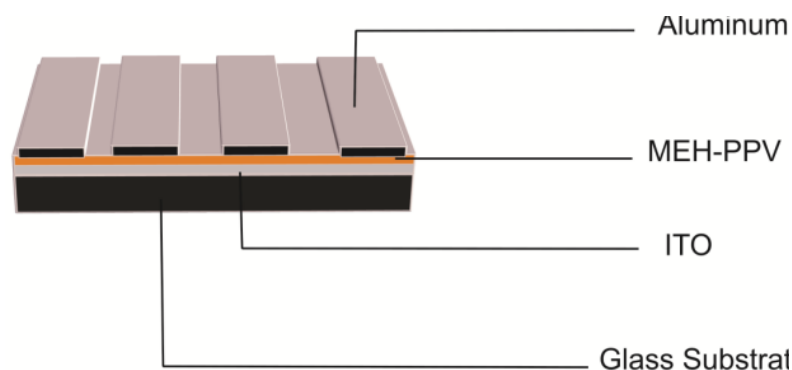


Figure 6.1: Schematic of OLED structure used in this study.

6.2.2 PDMS Encapsulation

A schematic of the stamping encapsulation process is presented in Figure 6.2. The PDMS mixture (Sylgard 184, Dow Corning) was prepared by mixing a pre-polymer base with a curing agent according to a 10:1 ratio (by weight) in a petri dish. After sufficient stirring, to ensure reaction between the components, the mixture was transferred to a vacuum chamber (10^{-3} Torr) for one hour to degas its contents. Aluminum stamps, suitably machined with the cathode patterns (as defined by the shadow mask), were dip coated with the uncured polymer mixture (Figure 6.2). The inherent adhesion forces between the Al stamps and the uncured PDMS mixture were sufficient to transfer a uniform coating to the patterned stamp surface.

The coated stamps were then pressed onto the surface of the fabricated OLEDs (for 30 seconds) with pressures ranging from 2.2 kPa to 5MPa. This was accomplished using an Instron table-top servo-hydraulic testing frame (Instron, Norwood, MA). The 2.2 kPa pressure level is equivalent to encapsulation by pressing the device and coated stamp by hand. The stamped devices were then annealed in a vacuum oven for 2 hrs at 80 °C to cure the PDMS layer.

For comparison, the encapsulated devices were also left at room temperature for 12 to 24 hrs as an alternative means to cure the PDMS layers. The transmission spectra of the prepared PDMS mixture were also obtained using a Unico 1200 spectrophotometer (Unico, Dayton, NJ). This was used to investigate the effects of the curing process on the optical characteristics of our sample.

The transmission properties of PDMS are important for investigating the suitability of this procedure for top emission organic light emitting diodes (TOLEDs) .The encapsulated

devices were characterized immediately or stored at a room-temperature of 20 to 23 °C and a relative humidity of 30% to 45%.

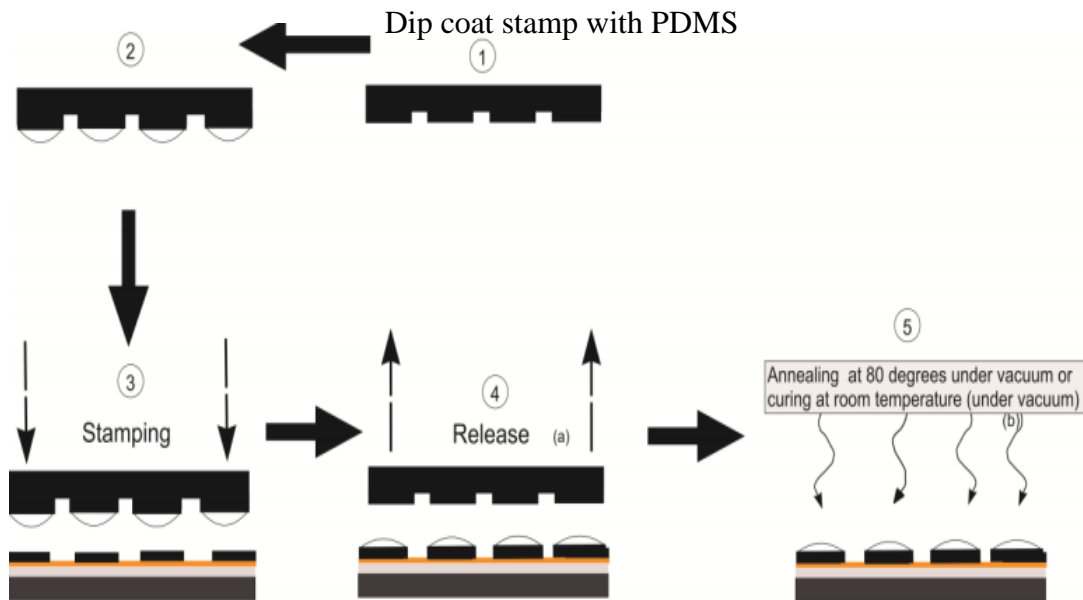


Figure 6.2: Flow diagram of the encapsulation process: (1) Stamp fabricated by micro-machining; (2) PDMS or suitable polymer material is dip coated onto the stamp; (3) The coated stamp is stamped onto the surface (electrodes) of the organic light emitting diode; (4) The stamp is released from the OLED surface, leaving behind the polymer barrier material; (5) The whole system is cured/annealed in a vacuum oven for 2 hrs at 80 °C.

6.3 Thin Film Layers/Device Characterization

6.3.1 Electrical Characterization

All the devices were tested within an hour of fabrication. Current-voltage characteristics for the encapsulated devices were obtained using a Keithley 2400 source meter under ambient conditions. The current-voltage relationships for encapsulated and exposed devices were

recorded over a period of days to compare the current-voltage characteristics for both types of specimens as a function of time. The current-voltage relationship for each device was also recorded before encapsulation. Device degradation from storage tests conducted in this manner is characterized by a reduction in the amount of current for a given voltage or equivalently, a higher voltage requirement for a given current density.

6.3.2 Optical Characterization

Optical spectral characteristics for both encapsulated and bare devices were obtained using a model GW-VIS2 Stellarnet spectrometer (Stellarnet, Tampa, Florida). Illumination from the OLEDs was collected using a suitably placed optical fiber cable that was attached to the spectrometer. The optical spectra were obtained and analyzed using a computer pre-loaded with SpectraWiz software (Stellarnet, Tampa, Florida) which interfaced directly with the spectrometer.

6.3.3 Sensitivity Tests

In order to characterize the effectiveness of the encapsulation procedure, tests were carried out in a humidified oven to investigate the sensitivity of the encapsulated devices to humidity and elevated temperature. Full immersion tests were also used to evaluate the resistance of encapsulated devices to totally moist environments. These tests involved controlled exposure to the environmental condition being investigated and subsequent characterization of the electrical characteristics, as described above.

6.3.4 Storage Tests

The current-voltage characteristics for both encapsulated and exposed devices were recorded for a number of days. The devices were stored in an amber acrylic container at

ambient conditions (23°C and 29% RH). The devices were stored in this manner to prevent excessive photo degradation.

6.3.5 Mechanical Test

A major objective of polymer encapsulation layers is the advantage of use in flexible device applications. Hence, the interfacial strength between the encapsulating layer and the surface of the device (the cathode) needs to be characterized under a variety of mechanical conditions that simulate real world device applications [21].

In this study, we use a fracture mechanics specimen known as the centrally-cracked Brazilian Disk (CCBD) [22, 23], to investigate the strength of the interface formed between the stamped, annealed encapsulation layer and the aluminum cathode material. This fracture specimen is also known as the “Brazil Nut”[23]. Furthermore, since fracture represents the reverse of adhesion, the interfacial strength is a useful measure of the adhesion between these two layers. References [22] and [24] contain detailed descriptions of the CCBD test.

The loading of a typical Brazil nut specimen is illustrated in Fig 6.3. Using this method, failure at any bi-material interface can be characterized by the mode of fracture (Figure 6.3). In that sense, interfacial failure occurs in mode I when there is a complete separation of the materials by “opening” [24]. This simply means that forces normal to the interface are responsible for the interfacial failure.

Mode II fracture occurs by in-plane shear forces [24]. In other words, forces that act parallel to the interface are responsible for interfacial failure. Reference [24] gives additional background information on the modes of fracture in interfacial failure. The Brazil nut specimen allows characterization of the interfacial/adhesive strength of two

dissimilar materials with respect to the failure “mode”. This is a preferred measurement method because it can be used to characterize the interfacial fracture toughness over a wide range of mode mixities (the ratio of mode II to mode I driving forces/displacements) that can occur in real flexible organic electronic structures.

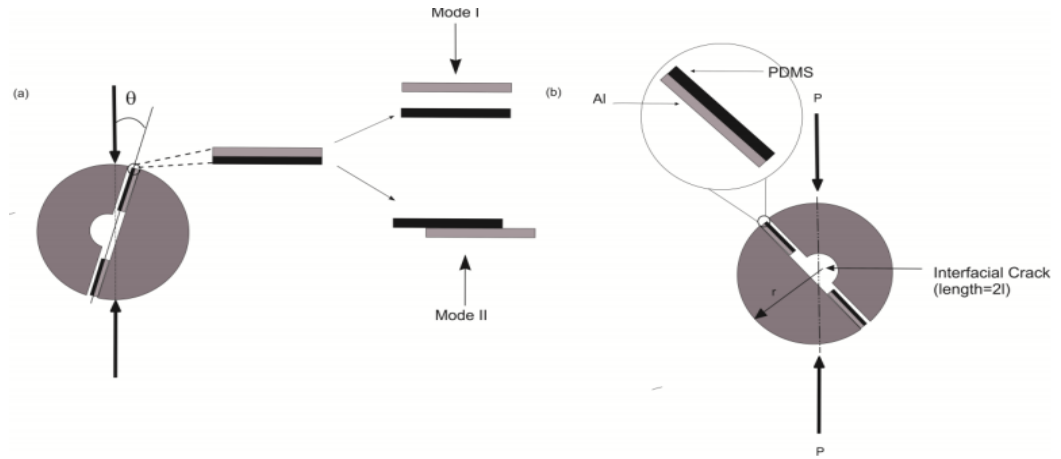


Figure 6.3: (a) Diagram showing the Brazil Nut specimen depicting the bi-material surface under consideration and the two possible modes of fracture being investigated; (b) Loading of the Brazil nut specimen.

The sample is loaded with respect to the axis as indicated in figure 6.3a. To vary the mode mixity, the angle between the notch axis and the loading direction, θ , was varied accordingly between 3° and 18° . The interfacial strength is proportional to the energy release rate of the center crack and is given by:

$$G = \frac{(f_I^2 + f_{II}^2) P^2}{a \bar{E}_1} \quad (6.1)$$

where f_I and f_{II} are tabulated functions that can be found in ref [25], P is the force/load that is used to completely separate the interface at a particular loading angle and \bar{E}_1 is the plane strain Young's modulus given by $\bar{E}_1 = \frac{E_1}{1-\nu^2}$, where ν is the

Poisson's ratio ($\nu = 0.3$) and E_1 is the Young's modulus of material 1. G is the energy release rate of the initial crack of length l within the Brazil nut specimen. G is a measure of the interfacial strength/ adhesion energy of the bimaterial interface. A high value of G can be interpreted as a high level of adhesion.

In this work, the configuration of each tested "Brazil nut" is shown in Fig 6.3b. For our specimens, the length, l , of the initial crack was 1 mm, while the radius, r , was 5.5 mm. The thickness, t (not shown), was 5 mm. The chosen dimensions are comparable to the size of a fully encapsulated OLED. The Al-PDMS interface investigated was chosen to represent the cathode-polymer interface of our device (Fig 6.1).

Using an Instron Model 8872 electro-mechanical testing machine equipped with a 10 kN load cell, load was continuously applied at a ramp rate of 0.001mm/sec. A linked computer interface was used to record Load and displacement data up to the point of interfacial separation/failure of the interface by using a linked computer interface.

At least three specimens were tested for each loading angle. The loading angle correlates with the mode mixity [22- 24] or loading phase parameter, ψ . The mode mixity is a function of the stress intensity factors, K_I and K_{II} , and ω , which is a material property parameter given in [22]. The relationship is given by:

$$\psi \approx \tan^{-1} \left(\frac{K_I}{K_{II}} \right) + \omega \quad (6.2)$$

where K_i is given by:

$$K_i = f_i \sigma \sqrt{\pi l} \quad (6.3)$$

where i designates Mode I vs. II. K_i is thus calculated independently for each mode (loading angle) and is a function of the stress, σ , crack length, l , and non-dimensional calibration factor, f . The factor, f , is itself a function of the specimen's relative crack length, l/r , and the loading angle θ [23]. The stress is a function of the necessary load applied to induce fracture, P , Brazil disk length and thickness parameters:

$$\sigma = \frac{P}{\pi r t} \quad (6.4)$$

The mode mixity can thus be used to infer the interfacial strength/adhesion that corresponds to a particular mode of fracture i.e. mode I or mode II. Generally, the $\psi=0^\circ$ condition corresponds to pure mode I fracture while $\psi=90^\circ$ corresponds to pure mode II fracture. Experimentally, values of ψ between pure mode I and pure mode II can be applied to the fracture specimen by varying the loading angle θ .

6.3.6 Adhesion Measurements

In order to gain additional insight into the nature of nano-scale interactions responsible for the adhesion between aluminum (cathode material) and PDMS, atomic force microscopy

was used to characterize the interface formed between cured PDMS and freshly deposited aluminum.

The surface roughness of PDMS material was characterized using a Dimension 3100 atomic force microscope (Veeco Instruments, Woodbury, NY) that was operated in the tapping mode. Adhesion force measurements were also made using an AFM pull-off technique [23]. This involved the measurement of the pull-off forces between the aluminum coated atomic force microscopy (AFM) tips and cured PDMS surfaces.

A Dimension 3100 atomic force microscope was used to measure the adhesion forces in the force mode. First, contact etched Silicon AFM probes (model CONT 20 by Veeco Instruments, Woodbury, NY) were coated with Al using a Denton/DV-502A e-beam evaporator (Denton Vacuum, Moorestown, NJ). Digital Imaging software was then used to determine the tip radii from scanning electron microscope (SEM) images similar to Figure 6.4a.

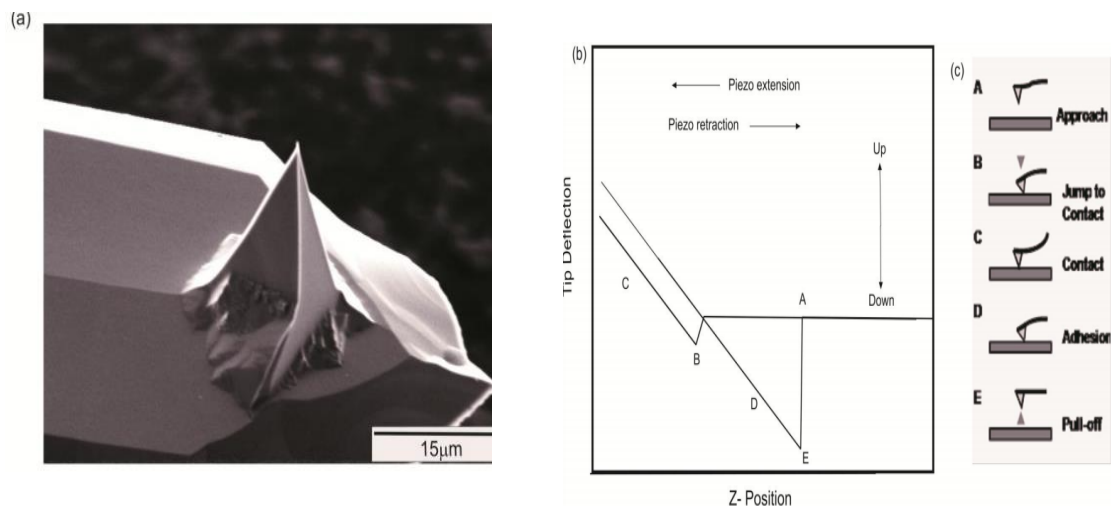


Figure 6.4: (a) Scanning Electron Microscopy (SEM) image of a coated Atomic Force Microscope tip. (b) Typical displacement curve. Note that the deflection of the tip is graphed on the vertical axis while the out of plane displacement of the cantilever tip is along the horizontal axis. (c) Corresponding physical description of points (A-E) on the displacement curve.

A force-displacement curve is obtained by moving the tip towards the sample surface until attractive forces enabled a “jump-to-contact” to occur between the coated tip and substrate surface. The cantilevered AFM probe then deformed elastically, as the displacement continued in the same direction. Subsequently, the displacement direction was reversed until the AFM tip pulled off from the substrate. This last “pull off” step occurred with a characteristic displacement, which, in conjunction with the stiffness of the cantilever tip, was used to determine the pull-off force from Hooke’s law [23]. A typical force-displacement plot is presented in Figure 4b, along with the corresponding physical scenarios in Figure 4c.

In order to calculate the contact lengths using the model described above, the surface (adhesion) energies (Γ) need to be determined. This requires the measurement of substrate surface roughness values (root mean squared roughness values) and coated AFM tip radii. The former were measured using tapping mode AFM images while the latter were obtained from SEM images. These were incorporated into the Derjaguin-Muller-Toropov (DMT) model [23] for the calculation of adhesion energies. The DMT model gives the adhesion energy between two surfaces as:

$$\gamma_{DMT} = \frac{F_{adhesive}}{2\pi R} \quad (6.5)$$

where γ_{DMT} is the adhesion energy for a particular interaction between two surfaces and R is the reduced radius, which is given by:

$$R = \left(\frac{1}{R_{rms}} + \frac{1}{R_{tip}} \right)^{-1} \quad (6.6)$$

where R_{tip} is the radius of the coated AFM tip and R_{rms} is the root-mean-squared roughness of the substrate (R_{rms}) obtained from tapping mode AFM scans. Defining the radius in this way takes into account the finite sizes of the tip and the effective contact radius of the substrate surface.

The adhesion values obtained from these experiments corresponds to the Mode I (opening mode) interfacial fracture toughness between cured PDMS and aluminum. In addition to direct measurement (for example, CCBD test), the calculation of G over the range of Mode I-II mixities can also be estimated based on the pure Mode I fracture toughness value, G_o , using [23]:

$$G = G_o \left(1 + \tan^2 \varphi \right) \quad (6.7)$$

Hence, the results from this force microscopy experiment can be extrapolated using equation (6.7) to obtain estimated fracture toughness values for varying loading conditions. A comparison between the values obtained from the CCBD experiments (uncured PDMS) and the force microscopy experiments (cured PDMS) will also shed light as to whether possible interactions during the curing process lead to increased adhesion between the two layers.

6.4 Finite Element Modeling

In the finite element simulations, we use COMSOL Multiphysics ver. 4.3 and MATLAB interfaces. The performance of an OLED can be categorized by several standard parameters, which are calculated from the luminous intensity, power consumption and geometry of the OLED. The current flowing through a defined area is given by the current density, J , defined by equation (6.8):

$$J = \frac{\text{Current, I}}{\text{Area, A}} (A/m^2) \quad (6.8)$$

Traditional drift-diffusion equations explain charge transport mechanisms in OLEDs in low electric field regime. An important model[25-26] to describe charge injection and transport in OLEDs is the one dimensional Poisson's equation given by equation (6.9):

$$\frac{\partial E(x)}{\partial x} = \frac{q}{\epsilon_r \epsilon_0} [p(x) - n(x)] \quad (6.9)$$

where , $E(x)$ is the electric field in the x-direction, $p(x)$ and $n(x)$ are the hole and electron number densities respectively, q is the magnitude of electronic charge, ϵ_r and ϵ_0 are the relative permittivity and permittivity of free space respectively.

The carrier density in Poisson's equation contains both trapped charge at the interface of the layers and flowing charge through the entire device. The current density has both a drift current component caused by the electric field and a diffusion current component which can occur because of a change in carrier density.

The drift-diffusion equations in one dimension are given by equations (6.10) and (6.11):

$$J_n(x) = q\mu_n n(x)E(x) + D_n \frac{\partial n(x)}{\partial x} \quad (6.10)$$

$$J_p(x) = q\mu_p p(x)E(x) + D_p \frac{\partial p(x)}{\partial x} \quad (6.11)$$

where μ_n and μ_p are respectively the electron and hole mobilities , D_n and D_p are the electron and hole diffusion coefficients.

The continuity equation defines the diffusion current component of the current density as follows:

$$\frac{\partial n}{\partial t} = \frac{1}{q} \nabla \cdot \vec{J}_n - R(n, p) - \frac{\partial n_t}{\partial t} \quad (6.12)$$

$$\frac{\partial p}{\partial t} = -\frac{1}{q} \nabla \cdot \vec{J}_p - R(n, p) - \frac{\partial p_t}{\partial t} \quad (6.13)$$

where \vec{J}_n = electron current density ; \vec{J}_p = hole current density; n_t and p_t are the number densities of trapped carriers; and $R(n, p)$ is the recombination rate per unit volume for electrons and holes.

The continuity equation for the trapped carriers is given by:

$$\frac{\partial n_t}{\partial t} = r_c(N_t - n_t) - r_e n_t \quad (6.14)$$

$$\frac{\partial p_t}{\partial t} = r_c(N_t - p_t) - r_e p_t \quad (6.15)$$

where r_c , N_t and r_e are the capture rate, trap density and emission rate respectively.

The efficiency, η_{OLED} , of the OLED gives a measure of the brightness and the source per current. This is defined by:

$$\eta_{OLED} = \frac{lu \text{ min } ance(cdm^{-2})}{J(Am^{-2})} (cdA^{-1}) \quad (6.16)$$

The power efficiency, η_{OLED}^P , of the OLED is the light flux per electric power given by:

$$\eta_{OLED}^P = \frac{2\pi \cdot lu \text{ min } ance(cdm^{-2}) \cdot area(m^2)}{Current(A) \cdot Voltage(V)} (lmW^{-1}) \quad (6.17)$$

The simulations with COMSOL multiphysics are carried out using the electromagnetic mode for in-plane transverse electric (TE) waves. This application mode is useful in analyzing electronic devices, in which Poisson's equation is being solved for the system considered. The goal here is to model the diffusion of light produced by an OLED made of Glass/ITO/MEH-PPV/Al configuration and that due to a Glass/ITO/MEH-PPV/Al/PDMS configuration.

In the latter configuration, PDMS acts as an encapsulant, to protect the underlying layers from degradation in oxygen and moisture-rich environments. The multilayer structure of the OLED studied here is in two dimensions with a width of 200 μm . The thickness of the entire structure is determined by that of the individual layers in the system. The refractive indices and the thicknesses of the different layers used in the simulation are displayed in Table 6.1. Covering air layers are also considered with a thickness of 1 μm .

The field excitation was set to 1 Vm⁻¹ at one side and all the boundaries to the outside of the structure were simulated as matched boundaries. Figure 6.5 represents the readily drawn structure in the COMSOL user interface. Two cases were considered: the OLED alone, without

PDMS and the OLED with PDMS as the encapsulant. The wave excitation was applied from bottom to top of the structure.

Table 6.1: Simulation Parameters for the Field Distribution at a Wavelength of 600 nm.

Layer	Thickness	Refractive Index
PDMS	1 mm	1.4
Aluminum	150 nm	0.6
MEH-PPV	100 nm	1.7
ITO	150 nm	1.9
Glass	1 mm	1.5

The drawn structure was exported to a MATLAB file and modified to a MATLAB function , that computes the transmission, with respect to the refractive index and thickness of the layers. With this function, it is possible to simulate a set of refractive index and thickness parameters , without having to return to the structure and using MATLAB interface for subsequent computation and storage.

The “parametric linear” problem solver in COMSOL multiphysics was used to simulate the S parameter matrix of the assembled structure in the wavelength range from 300 nm to 900 nm

with a step of 1 nm. The real part of the S_{21} parameter, which is given in decibels (dB) , was taken and the transmittance and reflectance calculated using the following equations:

$$\text{Transmittance} = 10^{\frac{S_{21}}{10}} \times 100(\%) \quad (6.18)$$

$$\text{Reflectance} = 100 - \text{Transmittance}(\%) \quad (6.19)$$

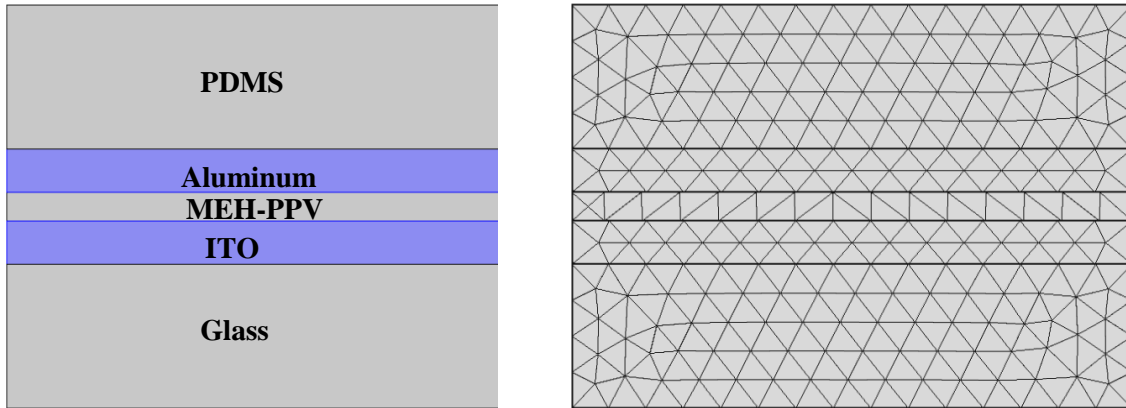


Figure 6.5: Schematic of optical model setup in COMSOL multiphysics

6.5 Results and Discussion

6.5.1 Electrical and Optical Characteristics

The effects of stamping pressure on the dimensions of the transferred encapsulation pattern were minimal, rendering faithful transfer of the stamp pattern onto the surface of the device. The thickness of the transferred pattern did not vary considerably and ranged between 100 and 150 μm , as measured with an optical microscope. There was no negative effect of the

bonding process on the device performance, as indicated by the current-voltage characteristics presented in Figure 6.6.

The annealing/curing step did increase the current output of the encapsulated device as shown (Figure 6.6a). This phenomenon was expected due to the increased adhesion between the Al cathode and the MEH-PPV active layer [27] in addition to the re-ordering of polymer chains due to increased mobility at T_g . The glass transition temperature, T_g , for MEH-PPV is typically 65 °C [27].

Figure 6.6b compares the current-voltage relationship of a device that was encapsulated by stamping at 5 MPa and allowed to cure at room temperature to the corresponding electrical characteristics of the same device before any encapsulation. This shows that there is also no marked change in the electrical behavior of the device and thus, the current increase in 5a can be attributed to the annealing step that is carried out during the encapsulation procedure. It is also noteworthy, that the range of investigated stamping pressures did not significantly affect the electrical performance of the devices (Fig 6.6c). Thus, devices encapsulated by typical hand pressures (220 kPa) performed at par with devices encapsulated at 5 MPa.

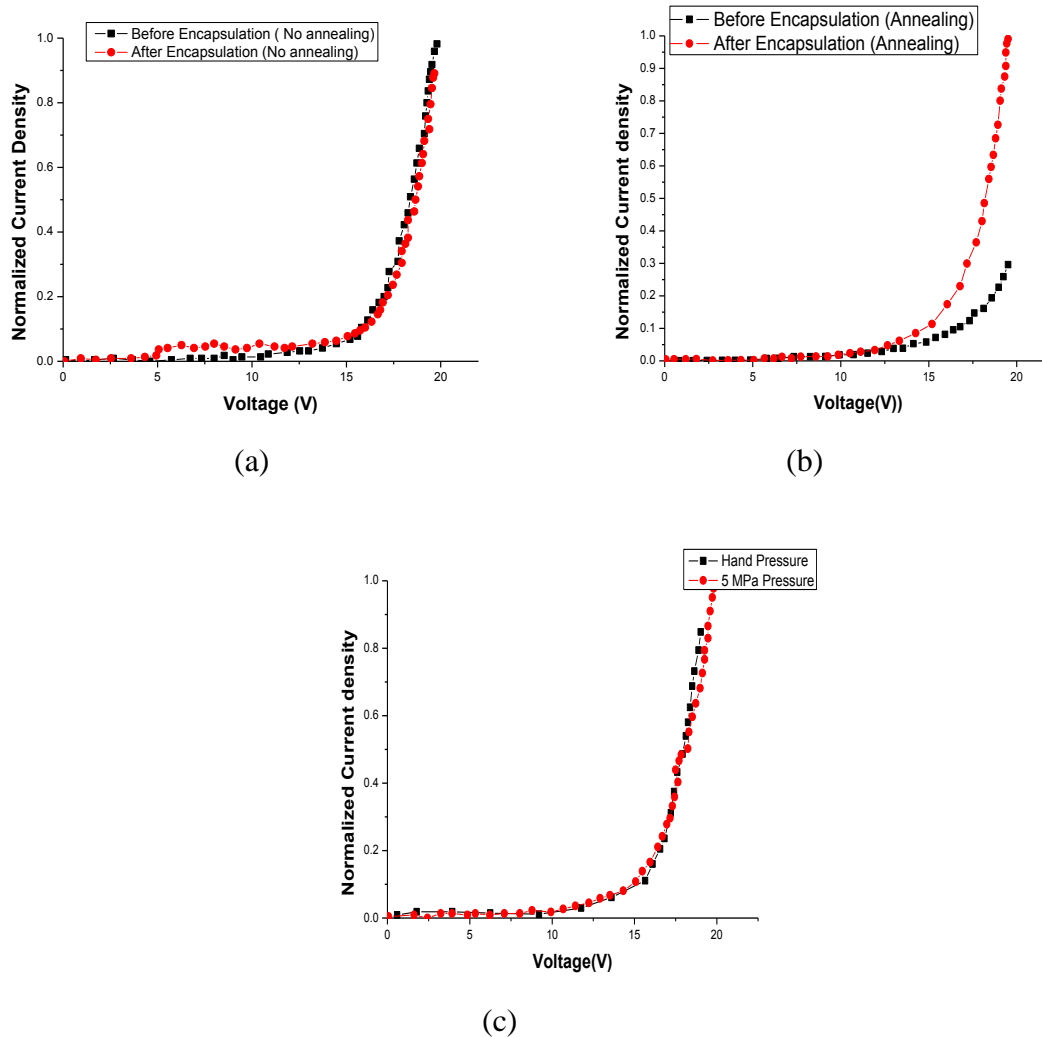
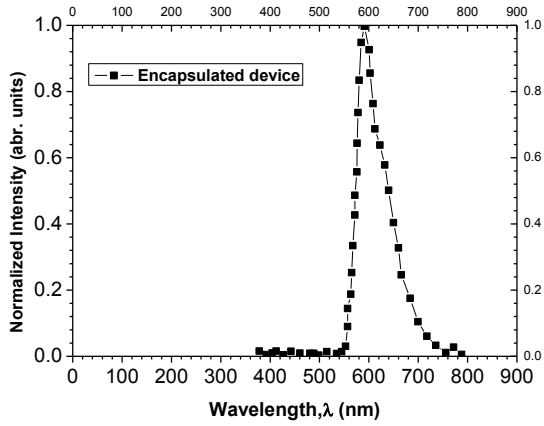


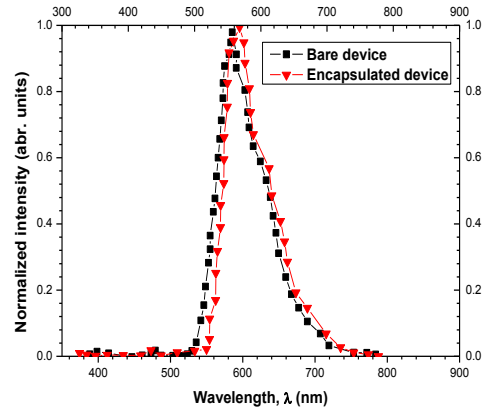
Figure 6.6: Current-Voltage relationships of encapsulated devices: (a) I-V curves of devices before and after encapsulation, showing the effects of annealing. (b) I-V curves of the devices before and after encapsulation at room temperature and 5MPa stamping pressure. (c) I-V curves of encapsulated devices showing the effects of stamping pressure.

The encapsulated devices produced fluorescent electroluminescence with a normalized spectral distribution, as presented in Figure 6.7a. Figure 6.7b presents a comparison between

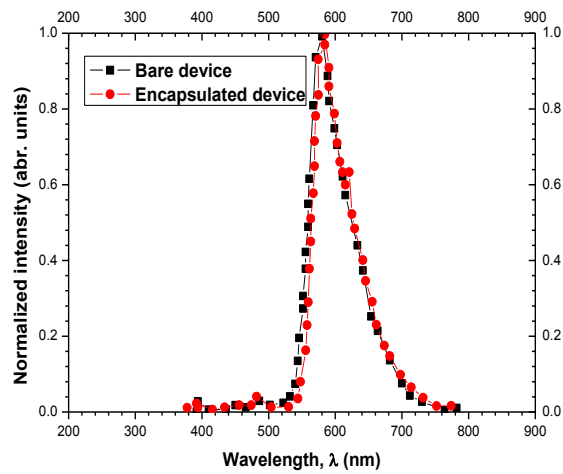
the optical characteristics of encapsulated and bare devices. As shown, there is a slight red shift of the spectrum obtained for the encapsulated device. This can be attributed to the annealing/curing step in the encapsulation process. This is confirmed by Figure 6.7c which compares the spectrum of a device encapsulated by curing at room temperature and a bare device that had no prior annealing. It can be seen that the peak wavelengths (~580 nm) for both spectra coincide. The relative noise in the spectra results is due to the difference in the spectrometer integration times.



(a)



(b)



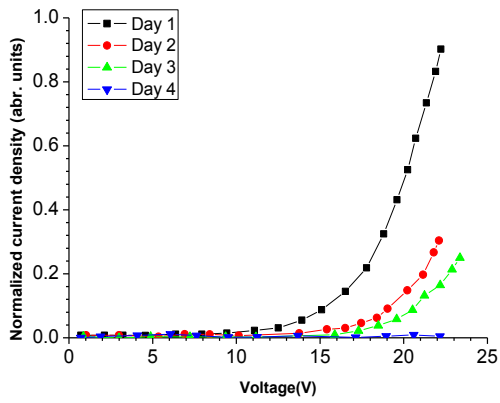
(c)

Figure 6.7: Electroluminescent spectrum of encapsulated devices: (a) EL spectrum of devices encapsulated by curing at 80°C for 2hrs. (b) Comparison of EL spectra of devices encapsulated by curing at 80°C for 2hrs with bare devices. (c) Comparison of EL spectra of devices encapsulated by curing at room temperatures with bare devices.

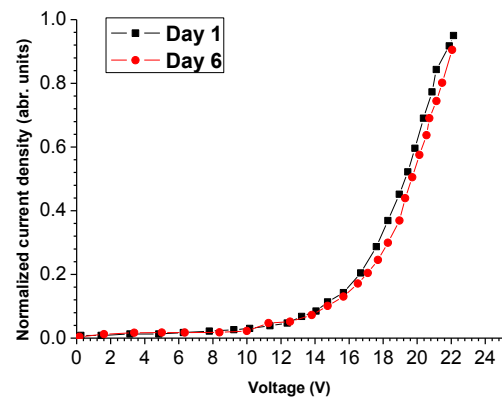
6.5.2 Sensitivity Tests

Figure 6.8a presents normalized I-V curves for bare devices, while Figure 6.8b presents the same measurements for encapsulated devices. The device characteristics were recorded over a period of 6 days. The encapsulated devices showed no change in the recorded I-V characteristics within the 6 day period while the exposed devices exhibited a much sharper decline in the current output within this same period. By the fourth day, the bare device does not produce any meaningful current and as such, there is no visible electroluminescence. By the sixth day, the bare device produces no current.

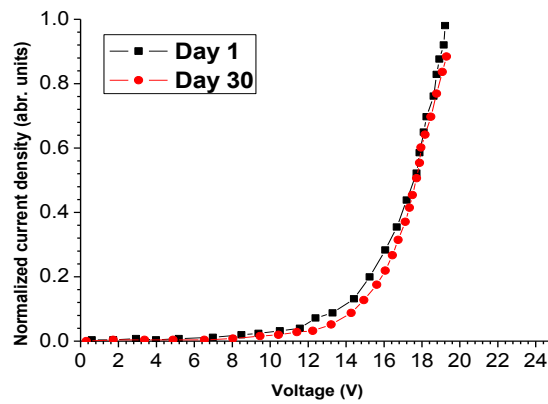
The normalized device characteristic for the encapsulated is also shown after 30 days of ambient storage (Figure 6.8c). It can be seen that there is still no substantial decline in the electrical performance of the encapsulated devices.



(a)



(b)



(c)

Figure 6.8: Current-Voltage relationships of encapsulated devices: (a) I-V curves of bare devices recorded daily; showing the effects of degradation. (b) I-V curves of encapsulated devices after 6 days. (c) I-V curves of encapsulated devices after 30 days

6.5.3 Storage Tests

To investigate the effectiveness of the encapsulation procedure, the devices were exposed to 55% humidity and 80°C for one hour. This test differs from the curing step of the encapsulation procedure because the annealing process was conducted in vacuum. Figure 6.9 reveals that there was no change in the electrical device characteristics for these particular testing conditions.

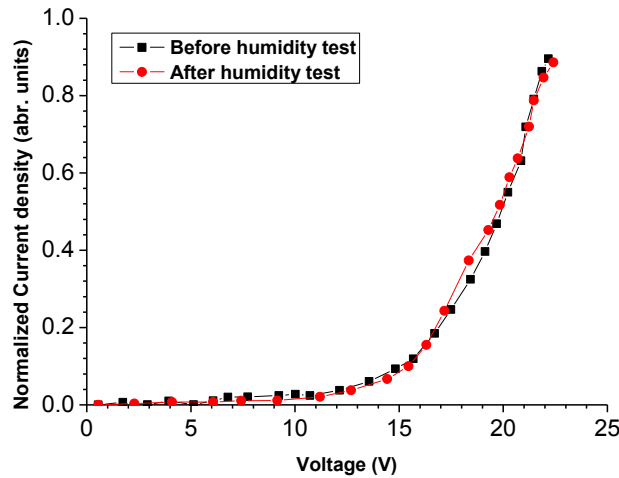


Figure 6.9: Current-Voltage relationships of encapsulated devices before and after elevated temperature and humidity tests.

Encapsulated devices were fully submerged underwater in a beaker of 500 ml of water at room temperature. These submersion tests were conducted for specific periods of time, ranging from 5 minutes to 16 hours. Figures 6.10a and 6.10b show the I-V curves for the encapsulated devices before submersion for 5 minutes and similar devices after full immersion for 16 hours respectively.

The results show that submersion for 5 minutes does not affect the current voltage characteristics of the encapsulated devices. The devices submerged for 16 hours were still

able to produce light visible to the naked eye even though there was a decrease in the current output of the device and a shift in the diode characteristic, indicating some device degradation.

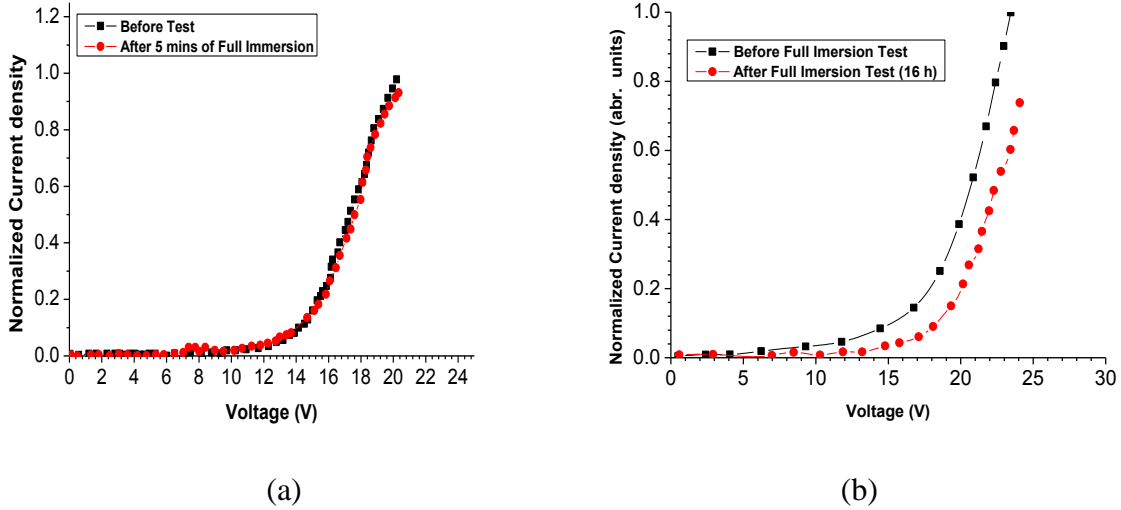


Figure 6.10: Current-Voltage relationships of encapsulated devices: (a) Before and after 5 minutes of full immersion in water. (b) Before and after 16hrs of full immersion in water.

6.5.4 Mechanical Robustness

The mechanical robustness of the PDMS-device interface was investigated using the CCBD test discussed above. The energy release rate/adhesion energy, G , is shown as a function of the mode mixity for the Al-PDMS interface in Figure 6.11. From the figure, it is revealed that the adhesion energy decreases for increasing ψ . This is in contrast with most interfaces that exhibit fracture toughness values that increase with mode mixity between pure mode I and pure mode II. It also suggests that the strength of the investigated interface decreases as the failure mode changes from mode I to mode II.

Thus, the interface has greater resistance to failure (due to the action of opening stresses) than to failure by in-plane shear stresses

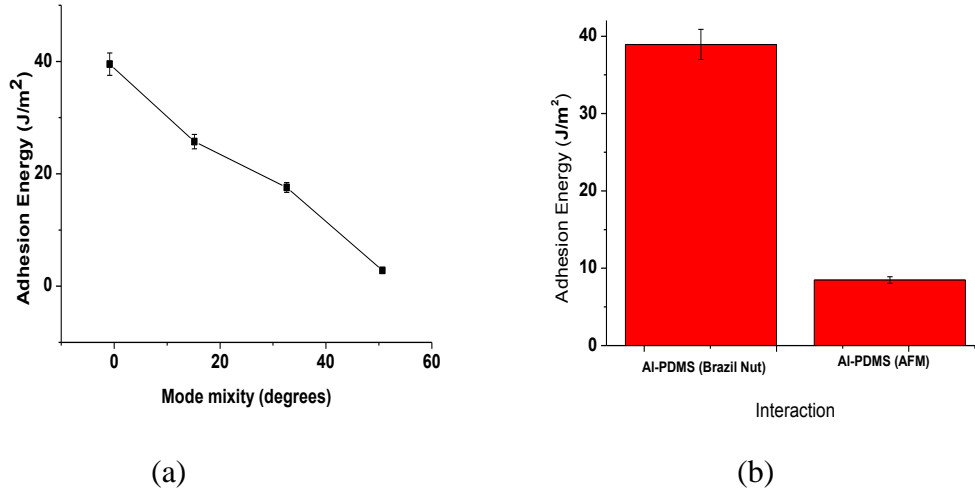


Figure 6.11: Mechanical robustness of the encapsulated device. (a) Result of the Brazil nut tests. (b) Adhesion energies

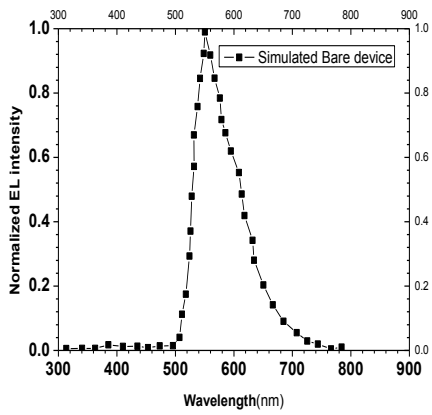
6.5.5 AFM Measurements

The force microscopy measurements revealed a lower adhesion measurement for the aluminum cured PDMS interface. The measured mode I interfacial toughness of 8.60 ± 1.98 J/m² is lower than the 39.37 ± 5.60 J/m² value measured using the Brazil nut specimen. This suggests that the adhesion is enhanced by the curing step of the encapsulation procedure. Extrapolation of the mode I adhesion value leads to a relationship as shown in Figure 6.10. The trend reveals increasing adhesion energy for increasing ψ as expected from equation (7).

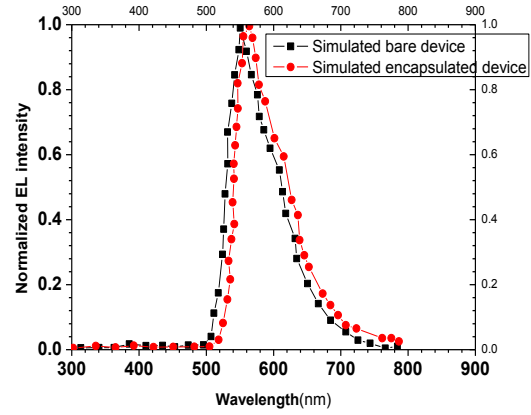
6.5.6 Optical Model

The EL spectrum of the simulated device without PDMS layer, which acts as the encapsulation layer is shown in figure 6.12 a. When PDMS was included in the structure, a

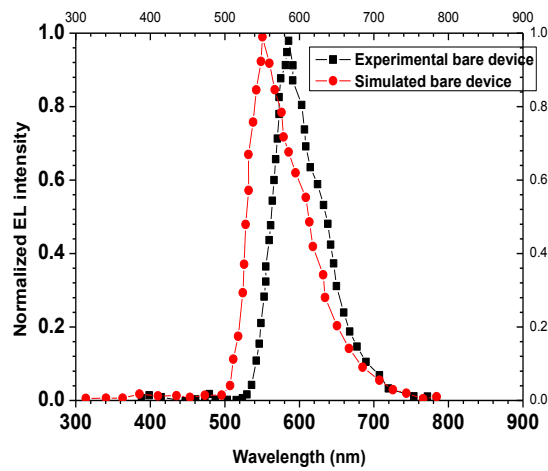
slight increase in the peak wavelength (red-shift) is noticed (figure 6.12b). Comparing the spectrum of the simulated bare device with the experimental results, we notice that the peak wavelength for the former (~540 nm) is less than for the latter (~580 nm) (figure 6.11c). This discrepancy is not clearly understood. It might be due to uncertainties in either the experiments or simulations.



(a)



(b)



(c)

Figure 6.12: Electroluminescence spectra of OLED obtained through optical modeling with COMSOL Multiphysics; (a) EL spectrum of simulated bare device; (b) EL spectrum of simulated bare device compared with its encapsulated counterpart; (c) EL spectrum of simulated bare device compared with the experimental bare device.

6.5.7 Implications

As discussed, the stamping process used for encapsulation was reproducible and yielded uniform films along the device surface. Furthermore, the range of stamping pressures had no noticeable effects on the performance of the encapsulation procedure in terms of storage and environmental barrier ability. Thus, the procedure requires a rather small amount of energy and is consequently “environment friendly”. Additionally, Figure 6.6 indicate that there is no degrading material transport between the encapsulating layer and the device layers. This suggests physical and electrical compatibility between both layers.

The particularly good film forming ability of the PDMS films can be attributed to the flexibility of the polymer chain, which arises from the large valence angle ($\sim 140^\circ$) in the Si-O-Si bonds within the polymer [19]. The results presented also indicate the effectiveness of the stamped polymer barrier as an encapsulation layer against environmental agents, such as moisture and humidity that typically plague organic electronic devices.

The effectiveness of the polymer barrier under the full immersion test can be linked to the nonpolar nature of the methyl groups in the polymer chain [19, 20]. This particular property renders the polymer surface hydrophobic in nature [20]. Similar hydrophobic properties of the perflourinated polymer, Cytop, have been used to encapsulate devices by spin coating to obtain a single layer barrier configuration [13]. These devices also showed some resistance to full submersion conditions in a manner much like the testing configuration described in this work.

The mechanical tests reveal a particularly strong interface with good adhesion levels between the encapsulating layer and the cathode material (aluminum) of our device for both the CCBD technique and the force microscopy technique. The difference in the experimentally measured mode I energies can be attributed to the annealing/curing step during the encapsulation process.

Annealing steps have been shown to increase the adhesion levels between metal and polymer interfaces [27-28]. In particular, annealing of Al and blended PPV derivatives (e.g. MEH-PPV) has been shown to create interfaces that withstand scotch-tape tests in comparison to preannealed Al-MEH-PPV interfaces that could not withstand such tests. Though this is a qualitative measure of adhesion, it suffices to show increased adhesion levels relative to the pre-annealed interface.

The mechanism of increased adhesion has been explained by the formation of an interfacial layer that is produced by complex chemical reactions between Al atoms and polymer side groups. These reactions lead to C-Al or C-O-Al strong covalent bonds between the metal and polymer [28]. Similar conclusions have been put forward to explain the increased current capacity of polymer light emitting diodes that contain Al-polythiophene interfaces [29].

A comparison of the mode I adhesion energies for different interfaces are presented in Table 1. By comparing the relative adhesion levels between the device layers, an adhesion-related mechanism can be used to explain the red-shifted spectrum noted in Figure 6. It has been reported that post-deposition annealing of polymer light emitting diodes, with similar structure to Figure 6.1, results in a blue-shifted electroluminescence spectrum [30].

The blue shifted spectrum can be attributed to the formation of an interfacial layer between the active polymer layer (MEH-PPV) and the metallic (Al) cathode [28]. This layer results from the covalent bonds described above. Due to the high strength of these bonds, there is a shortened conjugation length between bonds formed at the MEH-PPV/Al interface. This consequently leads to an observed blue shifted EL spectrum due to the fact that charge recombination and emission take place near the interface [31].

Table 6.2: Adhesion energies between different device layers in fabricated polymer light emitting diodes.

Interaction	Adhesion Energy (J/m ²)
PDMS-Al (CBB)	39
PDMS-Al(AFM)	8.6
Al-MEH:PPV	3
PEDOT:PSS-MEH:PPV	32
ITO-PEDOT:PSS	40
Glass-ITO	0.3

From Table 6.2, it can be seen that the adhesion between Al and PDMS is approximately 3 times greater than the corresponding adhesion between Al and MEH-PPV. This suggests that the covalent bonds formed between Al atoms and PDMS are greater (in strength or number) than the bonds formed between Al atoms and MEH-PPV. This prevents the formation of the high energy band-gap complexes that lead to blue shifted spectra in annealed, post-deposition OLEDs. (i.e. OLEDs that are annealed after cathode deposition).

Instead, there is a red-shifted spectrum which is similar to the electroluminescence spectrum observed in OLED structures that have been annealed before cathode (in this case, Aluminum) deposition. The red shifted spectrum is brought about by increased mobility of the polymer chains at temperatures higher than T_g which in turn leads to increased packing of the polymer films [29]. Thus, we observe a red-shifted spectrum in our packaged OLEDs similar to pre-

deposition annealed OLEDs due to the substantially larger adhesion levels between the PDMS over layer and the underlying Al electrode. It should also be mentioned that pre-deposition annealing of the polymer film increases the thermal stability of the resulting OLED and its ability to endure Joule heating during operation.

The measured adhesion levels are particularly high for applications that require substantial normal loading (such as simple bending [26, 32]) on the device and encapsulation layers. The tests reveal lower interfacial strength for applications requiring the presence of shear stresses (such as twisting). The lower levels of adhesion under mode II loading conditions could be attributed to possible shear softening phenomena that have been noted in commercially available branched polymers [33]. Hence, this polymer encapsulation scheme suffices rather well for flexible bending applications under conditions of low shear. For the given mode II adhesion energy, twisting applications employing this interface are still feasible provided that the applied torques result in mode II driving conditions that are below the measured interfacial fracture toughness values.

The operating lifetimes of the bare device and the encapsulated device were compared using an initial current density of 410 mA/cm^2 in air. Our measurement conditions are similar to an accelerated lifetime test, because the driving current is two orders of magnitude greater than that of a practical measurement, and is carried out at room temperature [10]. At these biasing conditions, the encapsulated device provided an average 90 minutes of illumination (till no light could be visible to the naked eye) compared to the approximately 3 minutes of illumination provided by the bare device.

We prefer to report the lifetime of these devices as a comparison between the two conditions because the device structure used has not been optimized for stability with respect to intrinsic degradation mechanisms due to, for example, the migration of Indium ions from the ITO anode [34] which has reportedly been reduced by the insertion of buffer layers such as PEDOT: PSS between the anode and the electroluminescent organic layer. Thus, the barrier properties of the presented encapsulation technique are better discussed and understood in terms of accelerated environmental tests in comparison with bare devices. With this consideration, the encapsulated devices withstood laboratory environmental and testing conditions for a period, 30 times longer than their bare, non-encapsulated counterparts.

Hence, the results from the encapsulation procedure indicate effectiveness against degrading environmental conditions. This reproducible stamping technique fulfills the encapsulation requirements of low temperature processing, inherent flexibility, device compatibility and mechanical robustness at low costs.

The use of a polymer barrier layer with nitrogen spacers [14] has been shown to be one of the clear advantages of simple encapsulation techniques similar to those presented here. These techniques bear the potential for engineering barrier properties by utilizing the permeability of polymers in a positive way. Guest nano-particle fillers with less oxygen and moisture permeability than the host polymer barriers can also be used to form hybrid materials with optimized volume fractions to obtain improved encapsulation properties [7]. Furthermore, because of the shift towards flexible structures, these encapsulated devices need to undergo a rigorous series of mechanical testing in order to determine their mechanical robustness under loading conditions that simulate the multi-dimensional stresses that can occur in practical

applications.. With this in mind, the CCBD technique used in this work provides useful information for tailoring devices towards different flexible applications.

In addition to good structural integrity and environmental protection, further functionality from the present encapsulation scheme can be derived from the fact that PDMS possesses excellent biocompatibility [35]. Recent work on the feasibility of biologically safe organic devices is illustrated by the fabrication of organic transistors on resorbable biomaterial substrates [36].

Thus, this encapsulation procedure has been able to utilize a polymer barrier that could be potentially integrated into bioengineering applications. Although this subset of applications has been investigated in several laboratories, further research needs to be conducted before fully integrated organic bio-compatible devices are commercially feasible.

6.6 Summary and Concluding Remarks

This work presents an effective solution for protecting organic light emitting devices from harsh environmental conditions. By evaluating the mechanical robustness of the PDMS-device interface, the scheme presented has been shown to produce encapsulated devices that maintain structural integrity, and therefore device functionality, for use in future commercial applications. The simplicity of the encapsulation procedure and the flexibility in choice of the encapsulation material hold promise for industrial scale implementation of the presented technique without the need for expensive deposition equipment or proprietary barrier materials.

References

- [1] C.W. Tang and S. A. VanSlyke, “Organic electroluminescent diodes”, *Applied Physics Letters*, 5(12), 913-915 (1987).
- [2] J. H. Burroughes, D.C. Bradley, A.R. Brown, R.N. Marks , K. Mackay, R.H. Friend, P.L. Burns, and A.B. Holmes, “Light-emitting-diodes based on conjugated polymers”,

- Nature 347, 539 (1990).
- [3] M.R. Krames, O.B. Shchekin, R. Mueller-Mach ,G.O. Mueller, L.Zhou , G.Harbers, and G.M. Crawford, “Status and Future of High-Power Light-Emitting Diodes for SolidState Lighting”, Journal of Display Technology 3, 160 (2007).
- [4] W. A. McDonald,Engineered Films for Display Technologies, J. Mater. Chem., 14 (2004).
- [5] P.E. Burrows, S.R. Forrest, S.P. Sibley, and M.E. Thompson, Color-tunable organic light-emitting device, Appl. Phys. Lett. 69, 2959 (1996).
- [6] P.E. Burrows, V. Bulović, S.R. Forrest, L.S. Sapochak, D.M. McCarty, and M.E. Thompson, “Reliability and Degradation of Organic Light Emitting Devices,” Appl. Phys. Lett. 65, 2922 (1994).
- [7] Y. Zhang ,M. Andreasson , H. Zhou, J. Liu ,T. Andersson, J-Y. Fan, “Encapsulation of OLED device by Using Anisotropic Conductive Adhesive”, International Symposium on High Density packaging and Microsystem Integration, Shanghai, China, June 26-28, p.1-4 (2007).
- [8] P.A. Ghosh, L.J. Gerenser, C.M. Jarman, and J.E. Fornalik, “Encapsulation of Pentacene/C60 organic solar cells with Al₂O₃ deposited by atomic layer deposition” Appl. Phys. Lett. 86, 503 (2005).
- [9] S.H. Kwon, S.Y. Paik, O.J. Kwon, and J.S. Yoo, “Triple-layer passivation for longevity of polymer light-emitting diode”, Appl. Phys. Lett. 79, 4450 (2001).
- [10] G.H. Kim, J.Oh, Y.S. Yang, L.M. Do, and K.S. Suh, “Lamination process encapsulation for longevity of plastic-based organic light-emitting devices”,Thin Solid Films 467, 1(2004) .
- [11] P. Mandlik, J. Gartside, L. Han, I-C. Cheng , S.Wagner, A.J. Silvernail, R. Ma, M.Hack and J.J. Brown, “A single-layer permeation barrier for organic light-

- emitting displays”, *Appl. Phys. Lett.* 92, 103309 (2008).
- [12] J. McElvain, H. Antoniadis, M. Hueschen, J. Miller, D. Roitman, J. Sheats, and R. Moon, Formation and growth of black spots in organic light-emitting diodes, *J. Appl. Phys.* 80, 6003 (1996).
- [13] J. Granstrom, J. S. Swensen, J. S. Moon, G. Rowell, J. Yuen, and A. J. Heeger, “Encapsulation of organic light-emitting devices using a perfluorinated polymer” *Appl. Phys. Lett.* 93, 193304 (2008).
- [14] Jimmy Granstrom, Michael Villet, Tirtha Chatterjee, Jeffrey A. Gerbec, Evan Jerkunica, and Anshuman Roy, “Multilayer barrier films comprising nitrogen spacers between freestanding barrier layers,” *Appl. Phys. Lett.* 95, 093306 (2009).
- [15] S.P. Subbarao, M.E. Bahlke, I. Kymissis, “A Laboratory Process for Encapsulation of Air Sensitive Organic Devices,” *IEEE Transactions on Electron Devices* 57, 153 (2010).
- [16] M. Scharnberg, V. Zaporozhchenko, R. Adelung, F. Faupel, C. Pannemann, T. Diekmann, and U. Hilleringmann, Tuning the threshold voltage of organic field-effect transistors by an electret encapsulating layer, *Appl. Phys. Lett.* 90, 013501, (2007).
- [17] Y-H. Kim, K-S. Shin, J-Y. Kang, E-G. Yang, K-K. Paek, D-S. Seo, and B-K. Ju, J. Y. Kang, and B. K. Ju, “Characterization of an integrated fluorescence detection hybrid device with photodiode and organic light-emitting diode,” *IEEE Electron Journal of microelectromechanical systems*, 15, 1152 (2006).
- [18] J-M. Han, J-W. Han, J-Y. Chun, C. H. Ok, and D-S. Seo, “Novel encapsulation method for flexible organic Light-Emitting diodes using poly (dimethylsiloxane),” *Jpn. J. Appl. Phys.* 47, 8986 (2008).
- [19] J.C. Lötters, W. Olthuis, P.H. Veltink and P. Bergveld, The mechanical properties of

- the rubber elastic polymer polydimethylsiloxane for sensor applications, J. Micromech. Microeng. 7, 145(1997).
- [20] M. Jin, X. Feng , J. Xi, J. Zhai , K. Cho, L. Feng, L. Jiang, “Super-Hydrophobic PDMS Surface with Ultra-Low Adhesive Force,” Macromol. Rapid Commun. 26, 1805 (2005).
- [21] J.S. Lewis and M.S. Weaver, Thin-film permeation barrier technology for flexible organic light-emitting devices, IEEE J. Sel. Top. Quantum Electron.10,45(2004).
- [22] Z. Suo and J.W. Hutchinson, “Sandwich test specimens for measuring interface crack toughness,” Mater. Sci. Eng., A 107,135 (1989).
- [23] N. Rahbar, Ph.D. Thesis, Princeton University, U.S.A (2008).
- [24] W. Soboyejo, Mechanical Properties of Engineered Materials, Marcel Dekker Inc., New York, NY, 2003.
- [25] H. Lee, Y. Hwang and T. Won, “ Finite Element Study on the Micro-Cavity Effect in OLED Devices”, Journal of Semiconductor Technology and Science, 14, 023(2014).
- [26] B. Ruhstaller, T. Beierlein, H. Riel, S. Karg, J. Campbell, and W. Riess, “ Simulating Electronic and Optical Processes in Multilayer Organic Light-Emitting Devices”, IEEE Journal of Selected Topics in Quantum Electronics, 9, 723 (2003).
- [27] J. H. Ahn, C. Wang, N. E. Widdowson, C. Pearson, M. R. Bryce, and M. C. Petty, “Thermal annealing of blended-layer organic light-emitting diodes,” J. Appl. Phys. 98 054508 (2005).
- [28] T-W. Lee and O.O. Park, Adv. Mater., “The effect of different heat treatments on the luminescence efficiency of polymer light emitting diodes,”12, 801 (2000).
- [29] J. Liu, T-F. Guo, and Y. Yang, “Effect of Thermal Annealing on the Performance of Polymer Light Emitting Diodes,” J. Appl. Phys. 91,1595 (2002).
- [30] J. Kim, J. Lee, C. W. Han, N. Y. Lee, and I-J. Chung, Effect of Thermal Annealing on the Lifetime of Polymer Light-Emitting Diodes," Appl. Phys. Lett. 82, 4238

- (2003).
- [31] I. D. Parker, "Carrier Tunneling and Device Characteristics in Polymer Light-Emitting Diodes," *J. Appl. Phys.* 75, 1656 (1994).
- [32] E. J. Hearn, *Mechanics of Materials 2, Third Edition: The Mechanics of Elastic and Plastic Deformation of Solids and Structural Materials*, Butterworth-Heinemann, Woburn, MA, 1997.
- [33] T. C. B. McLeish and R. G. Larson, "Molecular constitutive equations for a class of branched polymers: The pom-pom polymer." *J. Rheol.* 42, 81 (1998).
- [34] M. P. de Jong, D. P. L. Simons, M. A. Reijme, L. J. van IJzendoorn, A. W. Denier van der Gon, M. J. A. de Voigt, H. H. Brongersma, R. W. Gymer, Indium diffusion in model polymer light-emitting diodes, *Synth. Met.* 110, 1 (2000).
- [35] A. L. Thangawng, R. S. Ruoff, M.A. Swartz, M.R. Glucksberg, An ultra-thin PDMS membrane as a bio/micro-nano interface: fabrication and characterization *Biomedical Microdevices*, 9, 587 (2007).
- [36] C. J. Bettinger and Z. Bao, Organic Thin-Film Transistors Fabricated on Resorbable Biomaterial Substrates *Adv. Mater.* 22, 651 (2009).

Chapter 7

Concluding Remarks and Suggestions for Future Work

7.1 Concluding Remarks

The influence of pressure on the performance of organic light emitting devices has been investigated in this dissertation. The replacement of the conventional poly-(3,4-ethylenedioxythiophene): poly-(p-styrenesulfonate) (PEDOT:PSS) with molybdenum trioxide (MoO_3) for improving the performance of OLEDs was also examined. Interfacial adhesion was studied in the various bi-material interfaces that are relevant to OLEDs. The effects of interfacial defects (on transfer printing or lamination of OLED layers) was studied as well as encapsulation of OLEDs using a cost effective technique that uses polymers. The results and some salient conclusions are summarized below:

We have presented the results of a combined experimental, theoretical and computational study on the pressure effects on the pressure facilitated fabrication of OLEDs. The OLEDs were fabricated using novel HIL material, MoO_3 , and the more conventional material, PEDOT:PSS, respectively. The current-voltage characteristics of the devices were measured before and after the pressure treatment. The results showed a dramatic decrease of the threshold voltage after the application of pressure. This was true for both the MoO_3 -based and PEDOT:PSS-based devices. In order to study the mechanism of the pressure effects,

nanoindentation method and AFM techniques were used, respectively, to measure the key mechanical properties (Young's moduli and hardness values) and adhesion energies of the layers and interfaces.

The measured properties were incorporated into analytical models for the calculation of the contact profiles around dust particles interposed between the HIL and EML. A finite element model was used to simulate the evolution of contact profile under pressure. The results suggest that the application of pressure, to the evaporated or spin-coated device layers, reduces the blister area surrounding the interposed dust-particle. This increases the contact area between the HIL and EML. Since such significant increase in the contact area would facilitate charge transport across interfaces in the OLED structures, we attribute the reduction of the threshold voltages of the pressure-assisted devices to the improvement of the charge transport across interfaces with increased contacts. However, it is important to note that excessive lamination pressure may also induce device damage due to the sink-in of dust particles. This suggests the need to optimize the pressure for improved surface contact without significant damage.

An atomic force microscopy technique was used for the quantification of nano-scale adhesion between thin film interfaces in organic and hybrid organic/inorganic electronic devices is presented. The AFM technique was used for the characterization of the adhesion of a wide range of interfaces that are relevant to organic electronic structures. The study also considered the effects of TiO₂ nanoparticles on the adhesion within/ between the active layers. The results show that TiO₂ nanoparticles enhance the adhesion between the active layers and hole injection layers of the different structures. The dependence of energy release rate on crack size is also studied for different

bimaterial configurations. Such measurements can be used to improve existing device designs, while motivating large-scale processing methods, such as soft-contact lamination.

In this dissertation, we have presented experimental results to show the complete transfer of thin-films of the active layer material, MEH-PPV of OLEDs using soft-contact lamination. Spin-coated layers were used as controls. The lower roughness values obtained for laminated layers, both MEH-PPV and MEH-PPV infused with TiO₂ nanoparticles is an indication that such a procedure can be employed in large area display and lighting systems fabrication with the device performance not compromised.

Finite element simulations was used to provide a quantitative guidance with regards to the role interfacial defects play in understanding the mechanisms that govern transfer printing process.

A PDMS encapsulation method was presented as an effective solution for protecting organic light emitting devices from harsh environmental conditions. By evaluating the mechanical robustness of the PDMS-device interface, the scheme presented has been shown to produce encapsulated devices that maintain structural integrity, and therefore device functionality, for use in future commercial applications. The simplicity of the encapsulation procedure and the flexibility in choice of the encapsulation material hold promise for industrial scale implementation of the presented technique without the need for expensive deposition equipment or proprietary barrier materials. A red-shift of the EL spectrum noticed from the experiments was also confirmed by the optical simulations.

7.2 Suggestions for Future Work

Some suggestions for future work are presented below:

- (a) Further efforts should be made to fully understand the device physics and modeling of charge transport across the device interfaces of the compressed and uncompressed devices.
- (b) The deposition of MoO₃ by a solution-processed technique should be explored as a cost effective technique. This is because generally, thermal evaporation can be detrimental to underlying organic layers in the OLED system. Such devices can also be compressed and the performance studied. Focused Ion Beam Microscopy should also be used to check the interfaces of the compressed devices.
- (c) The effects of mixed mode loading on the integrity and reliability of the interfaces of the layers in the OLED structures needs further studies both experimentally and numerically. Cohesive Interface Modeling (CIM) is required, to study the initiation and evolution of cracks at the different device interfaces. We therefore need to conduct more experiments to determine the cohesive interface modeling parameters such as the fracture energy and cohesive strength of the interfaces of the different systems considered in this dissertation.
- (d) In the transfer printing experiments, although the results of the surface layer roughness achieved so far are quite reasonable compared to earlier results from spin-coating, further enhancement of this technique is necessary to optimize the layer properties. This optimization could be achieved by possibly tuning the 3-stage program parameters to have better detachment from the PDMS stamp. Also, a better surface treatment or modification of the PDMS stamp is required.
- (e) Further work is needed to develop a basic understanding of the spectral tuning that is observed in the encapsulated devices.